UNIVERSITY OF CALIFORNIA, SAN DIEGO

Soil Structure Interaction in Energy Piles

A Thesis submitted in partial satisfaction of the requirements
for the degree Master of Science

in

Structural Engineering

by

Diming Chen

Committee in charge:

Professor John S. McCartney, Chair
Professor Ahmed-Waeil M. Elgamal
Professor J. Enrique Luco

2016

The Thesis of Diming Chen is approved and it is acceptable in quality and form for publication on microfilm and electronically:

_____

_____

_____

Chair

University of California, San Diego

2016

TABLE OF CONTENTS

LIST OF SYMBOLS

L	Length of energy pile
D	Diameter of pile cross section
A or A_b	Cross section area of pile
A_s	Lateral surface area of pile
γ_p	Unit weight of pile
E	Young's modulus
K or K_f	Axial stiffness of pile
K_s	Stiffness of the side shear spring
K_{base}	Stiffness of the base spring
K_h	Pile head-structure stiffness
P	Load from the upper structure applied on the head of pile
n or N	The number of discretized pile elements
n_1	The number of elements above the null point
n_2	The number of elements below the null point
NP	The depth of null point
Q_t	Force at the head surface
Q_s	Force at lateral side surface
Q_b	Force at the base surface
Q_{ave}	Average force of elements
σ	Axial stress of pile element
ρ_t	Relative displacement between soil and pile at the head surface
ρ_s	Relative displacement between soil and pile at the middle surface
ρ_b	Relative displacement between soil and pile at the base surface
Δ	Elongation of pile element
m	Coefficient for updating the increment in the value of elongation
γ'	Effective unit weight of soil

z	Depth
ϕ'	Effective friction angle
c_u	Undrained shear strength
K_0	Coefficient of lateral earth pressure at rest
K_p	Coefficient of passive earth pressure
K_T	Reduction factor for coefficient of passive earth pressure
κ	Empirical coefficient of radial expansion
σ_v'	Effective overburden pressure
α_T	Coefficient of thermal expansion
ΔT	Change of temperature
s_c	Shape factor
d_c	Depth factor
N_c	Undrained bearing capacity factor for deep foundations
a_s	Parameter of side resistance-displacement curve
a_b	Parameter of base resistance-displacement curve
b_s	Parameter of side resistance-displacement curve
b_b	Parameter of base resistance-displacement curve
β	Empirical reduction factor for ultimate capacity
k_{sec}	Secant slope in Newton's method for finding the toe displacement
F_{unb}	Unbalanced force
i (superscript)	The element *i*
max (subscript)	Maximum or ultimate capacity of a given variable
b (subscript)	Value of a variable for the base of an element
M (subscript)	Value of a variable under mechanical load only
T (subscript)	Value of a variable under thermal load only
MT (subscript)	*Value of a variable under combined thermal and mechanical load*

LIST OF FIGURES

LIST OF TABLES

ACKNOWLEDGEMENTS

Financial support from NSF grant CMMI-0928159 is gratefully acknowledged. The contents of this paper reflect the views of the authors and do not necessarily reflect the views of the sponsor.

ABSTRACT OF THE THESIS

Soil Structure Interaction in Energy Piles

by

Diming Chen

Master of Science

University of California, San Diego, 2016

Professor John S. McCartney, Chair

This study focuses on developing an improved thermo-mechanical soil-structure interaction (i.e., load transfer) analysis to assess the axial strains, stresses, and displacements during thermo-mechanical loading of energy piles in different soils having different end restraint boundary conditions. This study builds on established analyses by (i) incorporating an algorithm to identify the location of the point of zero displacement (i.e., the null point) during changes in temperature, (ii) adding models for the ultimate side shear resistance representative of drained and undrained soils, and (iii) incorporating an unloading path for the side shear resistance curve. A parametric evaluation was performed

to understand the roles of the soil shear strength parameters, toe stiffness, head stiffness, side shear stress-displacement curve, and radial expansion, as well as the foundation type, mechanical load magnitude, and temperature change magnitude. This investigation showed that the end restraint boundary conditions played the most important role in controlling the magnitude and location of the maximum thermal axial stress. The soil type also caused changes in the nonlinearity of the axial stress distribution throughout the energy pile. The radial expansion did not affect the thermo-mechanical soil-structure interaction for the conditions investigated in this study. The thermo-mechanical load-transfer analysis was then calibrated to identify the parameters that match the observed soil-structure interaction responses from four case studies involving non-plastic soils, including one field study and three centrifuge studies. The ranges of calibrated parameters provide insight into the behavior of energy piles in non-plastic soils, and can be used for preliminary design guidance.

CHAPTER 1: INTRODUCTION

1.1 Motivation

Energy piles are a dual-purpose structural element built underground to exchange heat between a building and the subsurface while also transferring loads from the structure to the ground. Different from classical deep foundations, energy piles incorporate closed-loop, flexible, high density polyethylene (HDPE) tubing within the reinforcing cage, through which a heat exchange fluid (i.e., typically water mixed with propylene glycol) is circulated to transfer heat to or from the subsurface. The temperature of the fluid is controlled using a heat pump within the building. The relatively steady temperature of subsurface soil and rock, approximately equal to the mean annual air temperature (Burger et al. 1985), makes it possible to provide sufficient heat exchange to cover the base heating and cooling thermal loads for a built structure. The advantage of energy piles is that they provide a unique approach to reduce costs of ground-source heat exchangers, the consumption of fossil energy sources, and the energy bill.

Geotechnical design of energy piles requires consideration of the impact of temperature on the induced stresses and strains in the foundation, which may affect building performance. Specifically, heating and cooling of the foundation during heat exchange will lead to expansion and contraction of the foundation and soil. This may lead to deformations and changes in the stress state (Brandl 2006; Laloui and Nuth 2006; Bourne-Webb et al. 2009). Therefore, it is important for designers to understand what the behavior of energy piles. There are many means to simulate the energy piles. The mechanisms of thermos-mechanical soil-structure interaction have been documented in several full-scale case histories in the field (Laloui et al. 2003; Brandl 2006; Laloui et al.

2006; Bourne-Webb et al. 2009; Amatya et al. 2012; McCartney and Murphy 2012; Akrouch et al. 2014; Sutman et al. 2014; Murphy et al. 2015; Murphy and McCartney 2015; Olgun et al. 2014a; Wang et al. 2014). Thermoelastic finite-element (FE) analyses have been used to predict the changes in axial displacement, strain and stress in energy piles during heating and cooling (Laloui et al. 2006; Ouyang et al. 2011; Wang et al. 2012, 2015). However, FE analyses are complicated to perform for energy pile design due to the large number of parameters potentially needed that may require advanced testing to obtain, especially when nonlinear soil behavior is considered. Alternatively comparably simpler method called thermo-mechanical load transfer analyses can be used to predict the behavior of energy pile under temperature changes (Knellwolf et al. 2011; Plaseied 2012; Suryatriyastuti et al. 2013). This method combines a known shape of the mobilized side shear resistance and end bearing resistance curves together with knowledge of the ultimate side shear and end bearing capacities to estimate the distribution in axial stress, strain and displacement. Although this approach is simpler and requires fewer parameters, there is limited information on the range of parameters that describe the shapes of the mobilized side shear resistance and end bearing resistance curves needed to perform thermo-mechanical load transfer analyses.

1.2 Objectives

The main objective of this study is to understand the effects of model parameters on the output of the load transfer analyses to understand the relative importance of the different variables. Another equally important objective is to understand typical ranges of model parameters calibrated using experimental data on the thermo-mechanical behavior

of energy piles having different end-restraint boundary conditions in non-plastic soils where soil thermal volume changes are not expected.

1.3 Approach

To reach this objective, the thermo-mechanical load transfer analysis of Plaseied (2012) was updated to better capture the null point location, to incorporate different models for the side shear resistance of soils under drained and undrained conditions, and to consider different soil-pile interface shear resistance models with both loading and unloading considered. Next, a parametric evaluation is performed to understand the effects of different parameters on the stress-strain response. Then, the model is fitted to the experimental results from four different studies to calibrate the different model parameters. Finally, ranges and trends in the calibrated model parameters are synthesized to provide design guidance.

1.4 Scope

Chapter 2 includes a review of the current knowledge regarding the thermo-mechanical soil-structure interaction in energy piles. Chapter 3 provides a detailed description of the algorithms for mechanical and thermo-mechanical axial load transfer (T-z) analysis. Chapter 4 describes a parametric evaluation of energy pile type (floating, end-bearing, semi-floating), mechanical load applied to the pile head, soil shear strength, change of temperature, toe stiffness, head stiffness, side shear stress-displacement curve and radial expansion coefficient to study the impact of each parameter on strain-stress distribution along the energy pile. Chapter 5 involves calibration of the model parameters by fitting the model to the experimental results from different studies on energy piles in different settings. Chapter 6 provides design guidance on the choice of model parameters

by concluding the parametric evaluation and evaluation of field data. The complete load transfer analysis implemented in MATLAB is presented in Appendix A.

CHAPTER 2: BACKGROUND

Subsurface geothermal resources represent a great potential of directly usable energy, especially in connection with deep foundations and heat pumps. It is already common to utilize the geothermal energy in providing thermal needs of building. To utilize subsurface geothermal energy, heat exchanger is commonly incorporated in to drilled shaft foundations for circulating heat exchange fluid between the subsurface ground and structure. However, it also presents new challenges for the broader geotechnical engineering profession, in terms of technical issues associated with soil-structure interaction (Laloui et al. 2006; Bourne-Webb et al. 2009; Amatya et al. 2012; Murphy et al. 2015).

Observations from several case histories involving full-scale energy piles indicate that heating and cooling will lead to movements associated with thermal expansion and contraction of the foundation element and surrounding soil (Laloui et al. 2003; Brandl 2006; Laloui et al. 2006; Bourne-Webb et al. 2009; Amatya et al. 2012; McCartney and Murphy 2012; Akrouch et al. 2014; Sutman et al. 2014; Olgun et al. 2014a; Wang et al. 2014; Murphy et al. 2015; Murphy and McCartney 2015). These thermally-induced movements may lead to the generation of axial stresses due to the restraint of the foundation provided by soil-structure interaction and end-restraint boundary conditions (i.e., the stiffness of the overlying structure and the underlying bearing layer). Lateral movements of energy piles during heating and cooling has been proposed as a mechanism of changing soil structure interaction (McCartney and Rosenberg 2011; Mimouni and Laloui 2014), although cavity expansion analyses indicate that the amount of lateral expansion may not be sufficient to change the lateral stress state in all soils profiles (Olgun et al. 2014a). The end-restraint

boundary conditions play an important role in design guidelines being proposed for energy piles (Suryatriyastuti et al. 2013; Mimouni and Laloui 2014). As it is often difficult to vary the end-restraint boundary conditions in full-scale energy pile systems, an alternate modeling approach involves the use of centrifuge-scale energy piles to investigate soil-structure interaction mechanisms (McCartney and Rosenberg 2011; Stewart and McCartney 2014; Goode et al. 2014; Goode and McCartney 2014; Goode and McCartney 2015; Ng et al. 2014, 2015). Although centrifuge tests represent a comparatively simple situation compared to field tests, they have been shown to be useful for calibration of numerical simulations using thermo-elasto-plastic finite element models (Rotta Loria et al. 2015a, 2015b). Empirical data from centrifuge tests and field tests can also be useful for calibration of parameters or verification of load transfer analyses (Knellwolf et al. 2011; Plaseied 2012; McCartney 2015).

One of the first studies to modify the conventional load transfer analysis for mechanical loading to consider thermo-mechanical load transfer analysis was performed by Knellwolf et al. (2011), where the energy pile is assumed to be several elastic foundation elements connected to the soil by elastic perfectly-plastic springs. Plaseied (2012) developed a load transfer analysis by considering nonlinear springs, where the mobilized side shear and end bearing resistance springs were represented by hyperbolic curves. Plaseied (2012) also considered the role of radial expansion of the foundation elements, but did not perform a through parametric evaluation of this parameter. The algorithm in the model of Plaseied (2012) also fails to capture the exact location of the null point, and requires the user to choose the null-point, which leads to potentially inaccurate results.

Thermo-mechanical load transfer analysis has been validated on the basis of in-situ measurements of the loads and deformations experienced by heat exchanger test piles (Knellwolf et al. 2011; Plaseied 2012), but the choice of parameters for this method need to be studied in order to put this method to practical use. Energy pile design guidelines to account for thermal soil-structure interaction effects are available in different countries (Burlon et al. 2013; Bourne-Webb et al. 2014), but there is still a need for consistent soil-structure guidance to ensure implementation in practice worldwide (Olgun et al. 2014b).

CHAPTER 3: LOAD TRANSFER MODEL DESCRIPTION

3.0 Overview

An axial load transfer analysis is developed in this study to predict the behavior of energy piles subject to combined mechanical and thermal loading. Specifically, the traditional load transfer analysis developed by Coyle and Reese (1966), used to predict the settlement and stress distribution in deep foundations subject to mechanical loading, was extended by Knellwolf et al. (2011) and Plaseied (2012) to consider thermo-elastic deformation of the foundation and possible thermo-elasto-plastic deformation of the surrounding soil. The thermo-mechanical load transfer analysis is based on the following assumptions:

1. The properties of the foundation such as the Young's modulus (E) and coefficient of thermal expansion (α_T) remain constant along the foundation.
2. Downward and upward movements are taken as positive and negative respectively. Compressional stresses are also taken to be positive.
3. Foundation expands and contracts about a point referred to as the null point when it is heated or cooled (Bourne-Webb et al. 2009). The location of the null point depends on the upper and lower axial boundary conditions and side shear distribution, and will be defined later. Expansion strains are assumed to be negative.
4. Depending on the particular details of the soil profile, the ultimate side shear resistance can be assumed to be constant with depth in a soil layer (i.e., the α method) (Tomlinson 1957) or it can be assumed to increase linearly with depth in a soil profile (i.e., the β method) (Rollins et al. 1997). Both approaches are used in the parametric study of the analysis.

The following notations are used in the thermo-mechanical load transfer analysis:

- Q is used to represent axial forces within the foundation, at the foundation base and the internal loading between the elements.
- The letter ρ stands for the relative displacement between the foundation and soil.
- K_f, K_s and K_{base} are the stiffness values of the reinforced concrete foundation spring, the side shear spring, and the base spring, respectively.
- The indices "*b*", "*t*" and "*s*" represent the bottom, top and side of an element.
- The indices *M, T, MT* stand for mechanical, thermal loading and thermos-mechanical loading, respectively.
- The superscript "*i*" represents the element number within the foundation.
- The variable "L^i" represents the length of each element along the foundation.

3.1 Mechanical Load-Transfer (T-z) Analysis

3.1.1 Overview

The traditional load transfer analysis, as proposed by Coyle and Reese (1966) is used to calculate the deformation distribution within a pile under application of a mechanical load to the foundation head. The approach involves discretizing the foundation into a series of elements. The typical geometric variables and a schematic of the discretized energy pile and a typical element i is shown in Figures 3.1 and 3.2. The behavior of each foundation element can be represented by a spring with stiffness of K^i. The spring stiffness K^i is defined by the following equation:

$$K^i = E^i A^i / L^i \qquad \text{Eq. 3.1}$$

where A^i is the cross section area of element *i*, E^i is the Young's modulus of the reinforced concrete in element *i*, and L^i is the length of the element *i*.

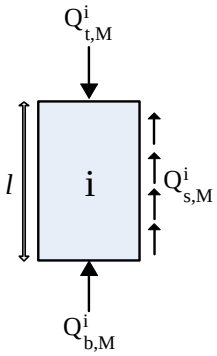

Figure 3.1: Typical element *i* with load variables

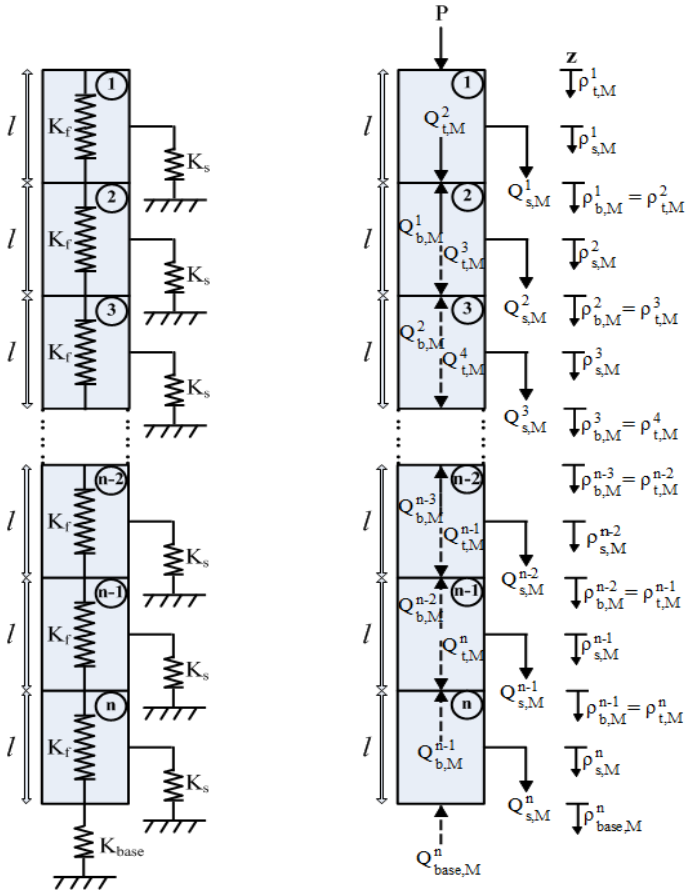

Figure 3.2: Discretized energy pile used in the load transfer analysis

3.1.2 Mobilized Side Shear and End Bearing Resistance Curves

The upward soil reaction force at the pile tip (or base) is also modeled using a non-linear spring. The spring response is specified as dimensionless tip stress (ratio of tip stress to tip bearing capacity) versus tip settlement, referred to as the Q-z curve. Similarly, the mobilization of side shear resistance with displacement is typically defined using a curve of dimensionless side shear versus relative movement between the element and the soil. The dimensionless side shearing stress is typically expressed as the ratio of the actual shearing stress to the shearing stress at failure, and dimensionless movement is the ratio of actual movement to the movement at failure. The dimensionless shearing stress versus displacement is usually referred to as the T-z curve. Examples of the Q-z and T-z curves for a drilled shaft foundation defined by O'Neill and Reese (1998) are shown in Figure 3.3.

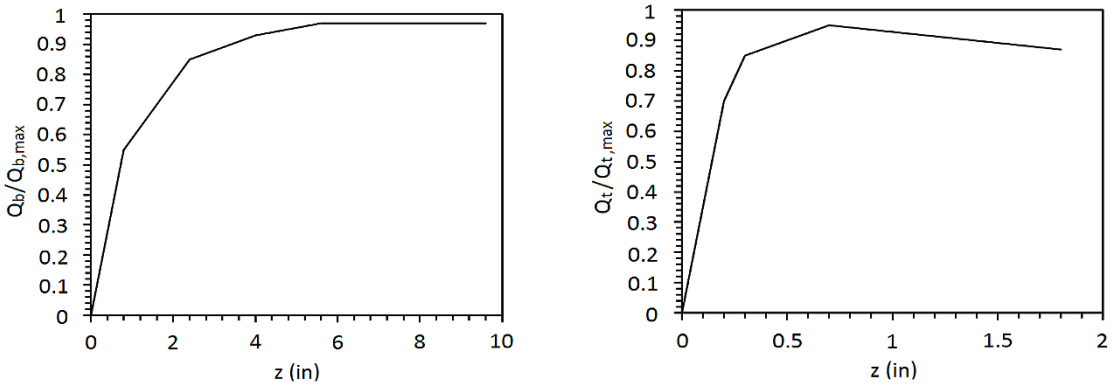

(a) (b)

Figure 3.3: Typical nonlinear spring inputs for the load transfer analysis: (a) Q-z curve; (b) T-z curve (Reese and O'Neill 1988)

The Q-z and T-z curves shown in Figure 3.3 are nonlinear, and have a shape that is approximately hyperbolic. Accordingly, they are represented in this study using a hyperbolic model for simplicity. The normalized side shear resistance (f_{T-z}) and the normalized base reaction (f_{Q-z}) at any relative displacement can be obtained using following equations:

$$f_{Q-z}(\rho_b^n) = \frac{\rho_b^n}{a_b + b_b \rho_b^n} \quad \text{Eq. 3.2}$$

$$f_{T-z}(\rho_s^i) = \begin{cases} \dfrac{\rho_s^i}{a_s + b_s \rho_s^i} & for\ loading \\ \dfrac{\rho_s^i}{a_s} + \dfrac{Q_{s,M}^i}{Q_{s,M,max}^i} - \left(\dfrac{1}{\dfrac{Q_{s,M,max}^i}{Q_{s,M}^i} - b_s} \right) & for\ unloading \end{cases} \quad \text{Eq. 3.3}$$

where a_b and b_b are the parameters that determine the shape of the Q-z curve, a_s and b_s are parameters that determine the shape of the T-z curve, and $Q_{s,M}^i$ represents the initial side shear resistance after the mechanical loading is applied. Because Murphy and McCartney (2014) found that the T-z curves are not sensitive to temperature, the T-z curves evaluated in this study are assumed to be independent of temperature. The mobilized values of base reaction (Q_b^n) and the side shear resistance (Q_s^i) can be obtained from Equations 3.2 and 3.3 by multiplying them by the ultimate end bearing force at the tip or the ultimate side shear force at a given depth of the pile, respectively. Examples of the hyperbolic Q-z and T-z curves used in this study are shown in Figures 3.4(a) and 3.4(b), respectively. Although

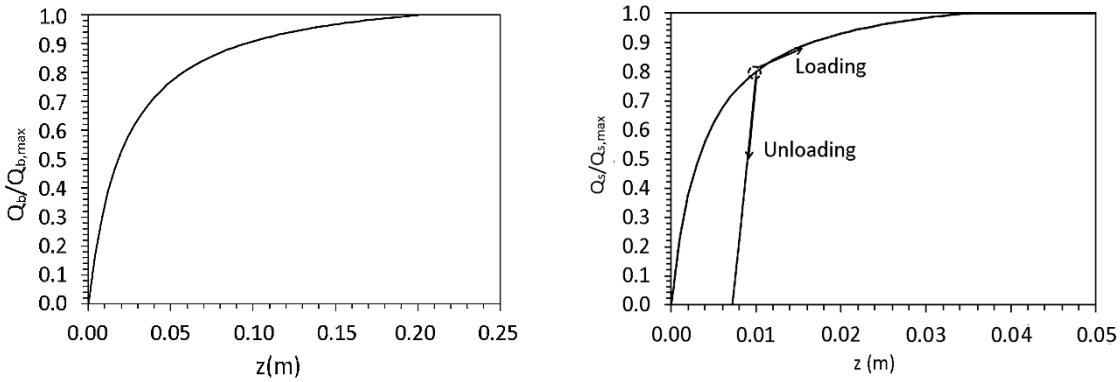

(a) (b)

Figure 3.4: Hyperbolic nonlinear spring inputs for the load transfer analysis used in this study: (a) Q-z curve; (b) T-z curve with unloading

this study is focused on monotonic heating, if heating and cooling were considered, an unloading path for the Q-z curve should also be included.

3.1.3 Ultimate Foundation Resistance

The ultimate side shear force at ambient temperature conditions at a given depth of i^{th} element can be calculated based on empirical methods. Typically, the ultimate side shear force for undrained soils in this studies is estimated using α-method (Tomlinson 1957) as shown in the following equation:

$$Q_{s,max}^{i} = \alpha A_s^i c_u \qquad \text{Eq. 3.4}$$

where c_u represents the undrained shear strength, α is an empirical reduction factor based on local soil condition, and A_s^i is the surface area of the foundation sides at i^{th} element. And the ultimate side shear force for drained soils is calculated using β-method as shown in the following equation:

$$Q_{s,max}^{i} = \beta A_s^i \sigma_v'(z) K_0 tan\phi' \qquad \text{Eq. 3.5}$$

where, β is an empirical reduction factor representing soil-interface behavior associated with installation effects, A_s^i is the surface area of the foundation sides at i^{th} element, $\sigma_v^{i\prime}$ is the effective overburden pressure at a given depth z, K_0 is the coefficient of lateral earth pressure at rest defined using Jaky's equation:

$$K_0 = 1 - sin\phi' \qquad \text{Eq. 3.6}$$

The β method was selected for this analysis because it is an effective stress-based approach to define the side shear resistance, and heating is assumed to occur slowly leading to drained conditions in the soil. Specifically, as the foundation expands into the soil during heating, the soil will consolidate and lead to an increase in ultimate side shear resistance of

the foundation. The impact of temperature on $Q_{s,max}^{i}$ due to the thermally induced radial expansion of the foundation for drained condition can be determined as follows (McCartney and Rosenberg 2011):

$$Q_{s,T,max}^{i} = \beta A_s^i \sigma_v'(z)\left[K_0 + \left(K_p - K_0\right)K_T\right]tan\phi' \quad \text{Eq. 3.7}$$

where K_p is the coefficient of passive earth pressure and can be defined as follows:

$$K_p = \frac{1 + sin\emptyset'}{1 - sin\emptyset'} \quad \text{Eq. 3.8}$$

K_T is a reduction factor representing the mobilization of passive earth pressure with thermal-induced strain, equal to:

$$K_T = \kappa\alpha_T\Delta T\left(\frac{D/2}{0.02L}\right) \quad \text{Eq. 3.9}$$

where κ is an empirical coefficient representing the soil resistance to expansion of the foundation and maybe a stress-dependent variables, but it was assumed to be constant and equal to 65 for this parametric analysis. α_T is the coefficient of thermal expansion of reinforced concrete (7.5×10^{-6} /°C). The geometric normalizing factor [(D/2)/(0.02L)] was proposed by Reese et al. (2006).

In this study, it is assumed that the ultimate end bearing resistance is expressed using an undrained analysis for all soils. This is a simplifying assumption, but is reasonable as it uses the shear strength at a point to evaluate the ultimate end bearing resistance. The ultimate end bearing $Q_{b,max}$ for the foundation can be defined as follows:

$$Q_{b,max} = c_{u,b}A_b s_c d_c N_c \quad \text{Eq. 3.10}$$

where $c_{u,b}$ is the undrained shear strength of the soil or rock at the foundation tip, A_b is the cross sectional area of the shaft toe, s_c is the shape factor (i.e., equal to 1.2 for a pile with

a circular or square cross-section), d_c is the depth factor (i.e., equal to 1.5 for a pile with depth over diameter larger than 2.5), and N_c is the undrained bearing capacity factor for deep foundations (i.e., equal to 9 for a pile with a circular or square cross-section and a tip depth greater than 2 foundation diameters).

3.1.4 Pile Discretization

Before the T-z analysis, the pile is firstly discretized into *n* elements. The value of the displacement at the bottom of the foundation $\rho_{b,M}^n$ is assumed for initiating the T-z analysis. The reaction force Q_b^n can be calculated using an imposed value of ρ_b^n, as follows:

$$Q_{b,M}^n = Q_{b,max} \cdot f_{Q-z}(\rho_{b,M}^n) \quad \text{Eq. 3.11}$$

The average axial force in the element can be calculated by averaging the axial force at the top $Q_{t,M}^n$ (initially zero) and bottom $Q_{b,M}^n$ for element n, as follows:

$$Q_{ave,M}^n = (Q_{b,M}^n + Q_{t,M}^n)/2 \quad \text{Eq. 3.12}$$

Next, the elastic compression of element *n* (Δ_M^n) can be calculated by dividing the average force Q_{ave}^n by the stiffness of the K^n, as follows:

$$\Delta_M^n = Q_{ave,M}^n / K^n \quad \text{Eq. 3.13}$$

Next, the displacement at the side of the element $\rho_{s,M}^n$ is defined by adding the settlement at the bottom of the element plus one half the elastic compression $\Delta_M^n/2$ of the element, as follows:

$$\rho_{s,M}^n = \rho_b^n + \frac{1}{2}\Delta_M^n \quad \text{Eq. 3.14}$$

Next, the mobilized side shear force on this element $Q_{s,M}^n$ is then defined using the T-z curve and the displacement at the side $\rho_{s,M}^n$, as follows:

$$Q_{s,M}^{n} = Q_{s,max}^{n} \cdot f_{T-z}\left(\rho_{s,M}^{n}\right) \quad \text{Eq. 3.15}$$

Finally, a new force at the top of the element $Q_{t,M,new}^{n}$ is defined by adding the force at the base of the element and the force on the side of the element to establish equilibrium, as follows:

$$Q_{t,M,new}^{n} = Q_{b,M}^{n} + Q_{s,M}^{n} \quad \text{Eq. 3.16}$$

If the difference between the new and old forces on the top of current element is not less than a user-defined tolerance (a value of 10^{-10} was used in this study) then the new axial force at the top of current element is used to calculate a new average axial force (using Equation 3.12) and a new $Q_{t,M,new}^{n}$ will be obtained after using Equation 3.13 to 3.16. The difference between $Q_{t,M,new}^{n}$ and $Q_{t,M}^{n}$ is calculated again to check whether the values have converged or not. The process is repeated iteratively until reaching a user-specified criterion (a value of 10^{-10} is used in this study).

When the axial stress values for a current element have converged, equilibrium of the upper adjacent element then calculated. To calculate for this new element, the force and displacement at the base of this new element are calculated using Equations 3.17 and 3.18, respectively:

$$Q_{b,M}^{i-1} = Q_{t,M}^{i} \quad \text{Eq. 3.17}$$

$$\rho_{b,M}^{i-1} = \rho_{b,M}^{i} + \Delta_{M}^{i} \quad \text{Eq. 3.18}$$

Then, the process involving Equations 3.12 to 3.16 is used, with superscript *n* being replaced with *i* for all these equations and these steps will be repeated until current element is converged. In this way, pile elements will become converged from the bottom to the top, successively.

When the stresses within the whole pile have converged, the equilibrium, compatibility and the constitutive laws of materials are satisfied in all the pile elements. However the load applied to the head of the pile *P* is not necessarily equal to the force at the top of the head element ($Q_{t,M}^{1}$). Thus, Newton's method can be used for quickly finding the toe displacement ($\rho_{b,M}^{n}$) that makes the calculated force at the heat of pile turns out to be the actual load from the upper structure ($Q_{t,M}^{1} = P$). To perform Newton's method, $\rho_{b,M}^{n}$ is assumed and a new value of $Q_{t,M}^{1}$ is calculated. Then, the secant stiffness that passes through origin is calculated using Eq. 3.19, as follows:

$$k_{sec} = Q_{b,M}^{1}/\rho_{b,M}^{n} \qquad \text{Eq. 3.19}$$

Then, the new displacement at the base of pile $\rho_{b,M,(new)}^{n}$ is calculated using Eq. 3.20, as follows:

$$\rho_{b,M,(new)}^{n} = \rho_{b,M}^{n} + k_{sec}(P - Q_{t,M}^{1}) \qquad \text{Eq. 3.20}$$

where *P* is the applied mechanical axial load from the structure. The new axial displacement at the base ($\rho_{b,M,(new)}^{n}$) should replace the old one and the process should be repeated until the difference between the new and old forces at the head of pile becomes less than user-defined tolerance (a value of 10^{-10} was used in this study).

3.2 Thermal Load Transfer (T-z) Analysis

The load transfer (T-z) analysis can also be used to predict the settlement and stress distribution in energy piles subject to thermal loading (i.e., without mechanical loading). In this regard, a spring should be added to the top of the foundation, which represents the foundation head-structure stiffness (Knellwolf et al. 2011). The "null point" location is a

very important variable to determine the thermal response of the energy pile during heating/cooling in this process.

3.2.1 Null Point Criterion

Once an energy pile is heated or cooled, it begins to expand or contract about its null point (Bourne-Webb et al. 2009). The null point is the location in the foundation where there is no thermal expansion or contraction, assuming that the temperature change occurs uniformly throughout the foundation. A schematic of a typical foundation divided into *n* equal elements, along with the location of the null point, is shown in Figure 3.5.

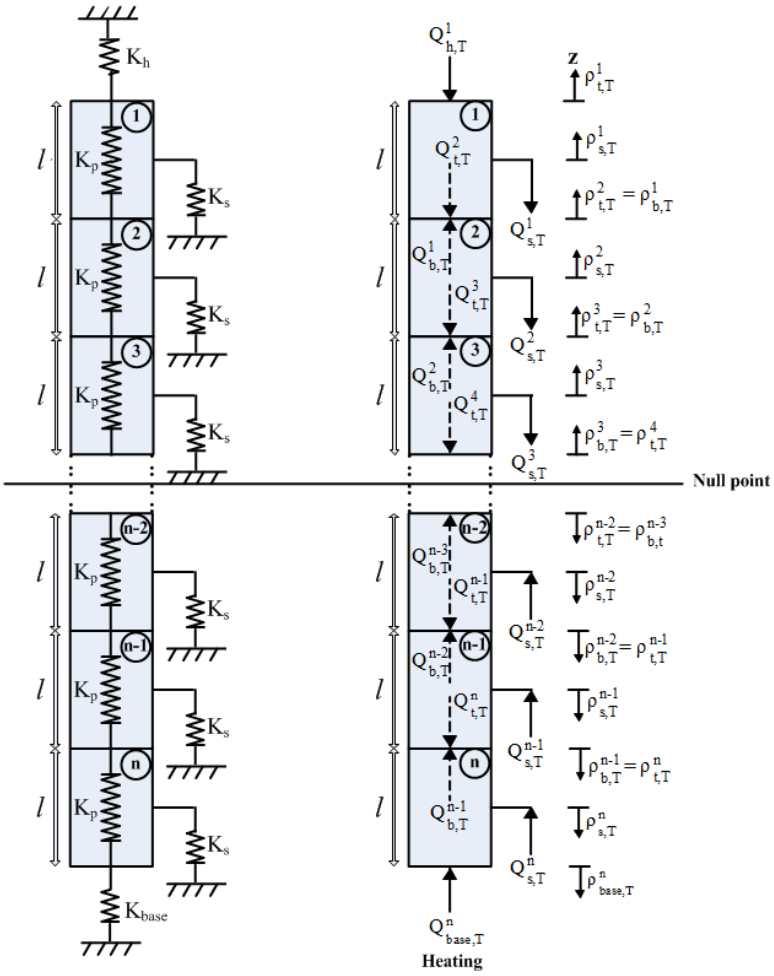

Figure 3.5: Typical foundation schematic of n elements highlighting the location of the null point (after Knellwolf et al. 2011)

In order for the displacement at the null point (denoted as NP) to be zero, the sum of the mobilized shear resistance and the structure reaction for the upper section of the null point should be equal to the sum of the mobilized shear resistance and the base reaction in the lower one (Knellwolf et al. 2011). Eq. 3.21 through 3.24 can be used to define the null point location along the foundation.

$$\sum_{i=1}^{NP} Q_{s,T}^{i} + Q_{t,T}^{1} = \sum_{i=NP+1}^{n} Q_{s,T}^{i} + Q_{b,T}^{n} \quad \text{Eq. 3.21}$$

$$Q_{t,T}^{1} = K_h \cdot \rho_{t,T}^{1} \quad \text{Eq. 3.22}$$

$$Q_{b,T}^{n} = Q_{b,max} \cdot f_{Q-z}\left(\rho_{b,T}^{n}\right) \quad \text{Eq. 3.23}$$

$$Q_{s,T}^{i} = Q_{s,T,max}^{i} \cdot f_{T-z}\left(\rho_{s,T}^{i}\right) \quad \text{Eq. 3.24}$$

In these equations, $Q_{b,T}^{n}$ represents the base response to the thermal expansion and contraction is defined using Q-z curve. $Q_{t,T}^{1}$ signifies that the structure response is linearly proportional to the relative displacement of the head of the foundation. $Q_{s,T}^{i}$ is the shear resistance of the foundation and can be determined by T-z curve. K_h represents the foundation head-structure stiffness, which depends on several factors including the rigidity of the supported structure, the type of contact between the foundation and the mat or raft, and the position and the number of energy piles (Knellwolf et al. 2011). The values of $\rho_{t,T}^{1}$ and $\rho_{b,T}^{n}$ represent the relative displacements at the head and the base of the foundation, respectively. $\rho_{s,T}^{i}$ is the relative thermal displacement at the side of the element i. It should be noted that Equations 3.23 and 3.24 are validated only if no mechanical load is applied at the head of the pile.

3.2.2 Algorithm

To compute the settlement and the stress distribution of the energy pile (under heating load for example), the first thing is to assume the null point location, NP. Then, appropriately divide the pile above the NP into n_1 elements and the pile below the NP into n_2 elements. The pile is assumed to be totally free to move (Knellwolf et al. 2011). Therefore, the first set of displacements can be derived using the following expression:

$$\Delta_T^i = L^i \alpha \Delta T \qquad \text{Eq. 3.25}$$

where L^i is the length of the element and the superscript *i* represents the element number along the energy pile.

For the part of pile below the null point, these elements move downward. Thus, the displacement of each element below the null point can be calculated using Equations 3.26 through 3.28, as follows:

$$\rho_{t,T}^i = \begin{cases} 0 & for\ i = n_1 + 1 \\ \rho_{b,T}^{i-1} & for\ i \neq NP \end{cases} \qquad \text{Eq. 3.26}$$

$$\rho_{s,T}^i = \rho_{t,T}^i + \frac{\Delta_T^{NP+1}}{2} \qquad \text{Eq. 3.27}$$

$$\rho_{b,T}^i = \rho_{t,T}^i + \Delta_T^{NP+1} \qquad \text{Eq. 3.28}$$

When the base element of the pile is reached, the base resistance can be computed by using Equation 3.29, as follows:

$$Q_{b,T}^n = Q_{b,max} \cdot f_{Q-z}(\rho_{b,T}^n) \qquad \text{Eq. 3.29}$$

where $f_{Q-z}(\cdot)$ represents the normalized function of Q-z curve. Then, from the base element to the element below and adjacent to the null point, the mobilized side shear force can be calculated using Equation 3.30, the force at the top of each element can be calculated

by equilibrium using Equation 3.31, and the thermal axial stress in each element can be calculated using Eq.3.32, as follows:

$$Q_{s,T}^{i} = Q_{s,T,\max}^{i} \cdot f_{T-z}^{loading}(\rho_{s,T}^{i}) \quad \text{Eq. 3.30}$$

$$Q_{t,T}^{i} = Q_{b,T}^{i} + Q_{s,T}^{i} \quad \text{Eq. 3.31}$$

$$\sigma_{T}^{i} = \frac{Q_{t,T}^{i} + Q_{b,T}^{i}}{2A_b} \quad \text{Eq. 3.32}$$

where $f_{T-z}(\cdot)$ represents the function of T-z curve and the superscript "loading" represents the loading path. After the forces acting on each element are defined, the next step is to define the actual elongation of each element using the following equation:

$$\Delta_{Tactual}^{i} = \Delta_{T}^{i} - \frac{\sigma_{T}^{i}.L_i}{E} \quad \text{Eq. 3.33}$$

The actual thermal elongation in each element will be lower than that present when the energy pile is free to move from the bottom. This actual thermal elongation should be replaced with the initial thermal elongation (free boundary) and the process from Equations 3.26 to 3.32 should be repeated in order to get a new actual thermal elongation from Equation 3.33 and this process should be repeated until the values of actual thermal elongation reasonably converge (the sum of difference between the new and old actual elongation ($\Delta_{Tactual}^{i}$) is less than 10^{-10}).

For the part of pile above the null point, heating leads to these elements move upward. Thus, from the element above and adjacent the null point to the top element, the displacement can be calculated using Equations 3.34 through 3.36, as follows:

$$\rho_{b,T}^{i} = \begin{cases} 0 & for\ i = n_1 \\ \rho_{t,T}^{i+1} & for\ i \neq NP - 1 \end{cases} \quad \text{Eq. 3.34}$$

$$\rho_{s,T}^{i} = \rho_{t,T}^{i} - \frac{\Delta_T^i}{2} \quad \text{Eq. 3.35}$$

$$\rho_{t,T}^{i} = \rho_{t,T}^{i} - \Delta_T^i \quad \text{Eq. 3.36}$$

When the top element is reached, the force at the top of each element from 1 to n_1 can be computed by using Equation 3.37, as follows:

$$Q_{t,T}^{i} = \begin{cases} K_h \cdot \rho_{t,T}^{i} & for\ i = 1 \\ Q_{b,T}^{i-1} & for\ i \neq 1 \end{cases} \quad \text{Eq. 3.37}$$

where K_h represents the head structure stiffness. The mobilized side shear force can be calculated using Equation 3.38, as follows:

$$Q_{s,T}^{i} = Q_{s,T,\max}^{i} \cdot f_{T-z}^{unloading}\left(\rho_{s,T}^{i}\right) \quad \text{Eq. 3.38}$$

The force at the base of these elements can be calculated by equilibrium, as follows:

$$Q_{b,T}^{i} = Q_{t,T}^{i} - Q_{s,T}^{i} \quad \text{Eq. 3.39}$$

and thermal axial stress in each element can be calculated using Equation 3.32.

Again, after the forces acting on each element are defined, the actual thermal elongation of each element can be defined using Equation 3.32. This actual thermal elongation should be replaced with the initial thermal elongation (free boundary) and the process for elements above the null point should be repeated until the values of actual thermal elongation reasonably converge (the sum of difference between the new and old actual thermal elongation is less than 10^{-10}).

Once the two parts of pile reach convergence, the unbalanced forced can be calculated by Equation 3.40, as follows:

$$F_{unb} = \left|Q_{t,T}^{n_1+1} - Q_{b,T}^{n_1}\right| \quad \text{Eq. 3.40}$$

It is necessary to adjust the location of the null point and appropriately mesh the pile to make the unbalanced force lower than user-defined tolerance. If the unbalanced force F_{unb} is not less than user-defined tolerance, it means that the assumed null point is not the actual one. If F_{unb} is positive, it means the actual null point locates deeper than the currently assumed null point, therefore a new null point need to be assumed a bit deeper than the current one. If F_{unb} is negative, it means the actual null point locates above the currently assumed one, therefore, the new null point need to be assumed a bit shallower than current one. After the new null point is assumed, the process above need to be performed. Finally, the unbalanced force F_{unb} will become less than the user-defined tolerance. The similar process can be used for pile under cooling load, though the sign and the function of T-z curve need to be paid attention.

3.3 Thermo-Mechanical T-z Analysis

The most accurate representation of energy piles can be obtained using a thermo-mechanical T-z analysis, in which the thermal loading is applied to an energy pile under an initial mechanical load. To calculate the thermo-mechanical response of the energy pile, the first step is to calculate the distribution in axial and interface displacements and forces along the pile for a given initial mechanical loading. Then the energy pile response due to thermal loading (heating for example) will be applied subsequently to define the overall response of an energy pile subject to thermo-mechanical loading. The thermo-mechanical process should be started from the "null point" which represents the zero thermal displacement point (not necessarily the point of zero thermo-mechanical displacement). The location of the null point is first assumed to start the analysis, and the part of pile above and below the null point is equally and appropriately meshed into n_1 and n_2 elements,

respectively (totally N elements). Then, similar to the thermal algorithm, the initial displacements are considered to be the same as the free boundary condition ($\Delta_T^i = l_i \alpha \Delta_T$). After the mechanical T-z analysis, a similar thermal T-z analysis is performed to calculate the response of energy pile under the combined thermo-mechanical load.

For the elements below the null point, the thermal displacement of each element is calculated using Equations 3.26 through 3.28 from the element $n_1 + 1$ to the element N, as presented above. The thermo-mechanical displacement of these element can be calculated using Equations 3.41 through 3.43, as follows:

$$\rho_{t,MT}^i = \rho_{t,M}^i + \rho_{t,T}^i \quad \text{Eq. 3.41}$$

$$\rho_{s,MT}^i = \rho_{s,M}^i + \rho_{s,T}^i \quad \text{Eq. 3.42}$$

$$\rho_{b,MT}^i = \rho_{b,M}^i + \rho_{b,T}^i \quad \text{Eq. 3.43}$$

where the subscript "MT" represents the combined thermal and mechanical loading. While the base of the energy pile is reached, the thermo-mechanical force in each element can be calculated using Equations 3.44 through 3.47 from the element N down to the element $n_1 + 1$, as follows:

$$Q_{b,MT}^i = \begin{cases} Q_{b,max} \cdot f_{Q-z}^{loading}\left(\rho_{b,MT}^i\right) & for\ i = N \\ Q_{t,MT}^{i+1} & for\ i \neq N \end{cases} \quad \text{Eq. 3.44}$$

$$Q_{s,MT}^i = Q_{s,T,max}^i \cdot f_{T-z}^{loading}\left(\rho_{s,MT}^i\right) \quad \text{Eq. 3.45}$$

$$Q_{t,MT}^i = Q_{s,MT}^i + Q_{b,MT}^i \quad \text{Eq. 3.46}$$

$$\sigma_T^i = \frac{Q_{t,MT}^i + Q_{b,MT}^i}{2A_b} - \sigma_M^i \quad \text{Eq. 3.47}$$

where σ_M^i is calculated using the Eq. 3.48, as follows:

$$\sigma_M^i = \frac{Q_{ave,M}^i}{A_b} \quad \text{Eq. 3.48}$$

After the forces acting on these elements are defined, the actual thermal elongation of each element is calculated using Equation 3.33 as mentioned before. Again, the actual thermal elongation in each element will be lower than that present when the energy pile is free to move from the bottom. This actual thermal elongation should be replaced with the initial thermal elongation (free boundary) and the process for computing the response for the part of pile elements below the null point should be repeated until the values of actual elongation reasonably converge (the difference between the new and old actual elongation is less than 10^{-10}).

Similar process is used for the part above the null point. The thermal displacement of each element is calculated using Equations 3.34 through 3.36 from the $n_1{}^{th}$ element to the top element, as presented above. The thermo-mechanical displacement of these element can be calculated using Equations 3.41 through 3.43, as presented above. When the head of the energy pile is reached, the thermo-mechanical force in each element can be calculated using Equations 3.49 through 3.52 from the top element to the $n_1{}^{th}$ element, as follows:

$$Q_{t,MT}^i = \begin{cases} P - K_h \cdot \rho_{t,T}^i & for\ i = 1 \\ Q_{b,MT}^{i-1} & for\ i \neq 1 \end{cases} \quad \text{Eq. 3.49}$$

$$Q_{s,MT}^i = Q_{s,T,max}^i \cdot f_{T-z}^{unloading}\left(\rho_{s,MT}^i\right) \quad \text{Eq. 3.50}$$

$$Q_{b,MT}^i = Q_{t,MT}^i - Q_{s,MT}^i \quad \text{Eq. 3.51}$$

$$\sigma_T^i = \frac{Q_{t,MT}^i + Q_{b,MT}^i}{2A_b} - \sigma_M^i \quad \text{Eq. 3.52}$$

where σ_M^i is calculated using Equation 3.48. Again, after the forces acting on these elements are defined, the actual thermal elongation of each element is calculated using Equation 3.33 as mentioned above. This actual thermal elongation should be replaced with the initial thermal elongation (free boundary) and the process for computing the response for the part of pile elements below the null point should be repeated until the values of actual thermal elongation reasonably converge (the difference between the new and old actual thermal elongation is less than 10^{-10}).

It is worth noting that these iterations no matter for the part above or below the null point might not be converged when the head stiffness and the base stiffness is large. Therefore, when this happens, Equation 3.33 should be replaced with Equation 3.53, as follows:

$$\Delta_{Tactual}^i = \Delta_T^i - m \cdot \frac{\sigma_T^i . L_i}{E} \qquad \text{Eq. 3.53}$$

where m is a coefficient that can make Δ_T^i change less intensely to keep Δ_T^i in the range that permits it to converge. When both parts of the pile reach convergence, the unbalanced force can be defined as follows:

$$F_{unb} = \left|Q_{t,MT}^{NP+1}\right| - \left|Q_{b,MT}^{NP}\right| \qquad \text{Eq. 3.54}$$

If the unbalanced force F_{unb} is not less than user-defined tolerance, it means that the assumed null point is not the actual one. If F_{unb} is positive, it means the actual null point locates deeper than the currently assumed null point, therefore a new null point need to be assumed a bit deeper than the current one. If F_{unb} is negative, it means the actual null point locates above the currently assumed one, therefore, the new null point need to be assumed a bit shallower than current one. After the new null point is assumed, the process above

need to be performed. Finally, the unbalanced force F_{unb} will become less than the user-defined tolerance, which means that the assumed null point is reasonably close to the actual null point and the behavior of pile obtained from the current value of the assumed null point can be accepted.

CHAPTER 4: LOAD TRANSFER MODEL PARAMETRIC EVALUATION

4.1 Effect of Foundation Type

In practice, pile foundations can be classified based on their primary mode of resistance to axial loads. The primary pile types are semi-floating piles, in which case the pile resists axial loads by a combination of end bearing and side shear resistance, floating piles, in which case the pile resists axial loads by primarily side shear resistance, and end-bearing piles, in which case the pile resists axial loads by primarily end-bearing resistance. Each of these different pile types will also provide different restraints to thermo-mechanical movement if the pile is converted into an energy pile. Of these pile types, the semi-floating energy pile is the most commonly encountered, but there are instances where the other types are also encountered.

In order to assess the impact of pile types, it was first important to come up with a baseline set of soil and pile properties that can be used to make the comparisons as fair as possible. The pile was assumed to consist of the typical concrete mixture used in drilled shaft foundations in the field. The energy pile parameters are given as follows:

- Length L = 13.1 m
- Diameter D = 1.2 m
- Unit weight of pile γ_p = 24 kN/m^3
- Young's modulus of reinforced pile E = 30 GPa
- Coefficient of thermal expansion $\alpha_T = 10\times10^{-6}$ m/m°C

Drained soil properties were assumed for the ultimate side shear resistance along the pile, while an undrained shear strength was assumed for the soil at the toe of the pile.

The soil parameters for this parametric analysis are given as follows, which are similar to those used in the analysis of McCartney and Rosenberg (2011):

- Drained friction angle of soil $\phi = 30°$
- Effective unit weight of soil $\gamma' = 18$ kN/m^3
- Undrained shear strength of soil at the base of the energy pile $c_{u,b} = 54$ kPa

There are also different soil-structure interaction parameters that need to be selected, including the shapes of the side shear mobilization curve (the T-z curve) and the end bearing mobilization curve (the Q-z curve). These model parameters are used in Equations 3.2 and 3.3, which are used to represent the smooth Q-z and T-z curves, respectively. In all of the comparisons, it is assumed that the pile temperature is constant with depth, an assumption that is approximately valid based on field data (Murphy et al. 2015; Murphy and McCartney 2015).

Table 4.1: Properties of the T-z and Q-z curves for the different types of energy piles evaluated in this analysis

	Floating	End bearing	Semi-Floating
a_s	0.0035	-	0.0035
b_s	0.9	-	0.9
a_b	∞	0.002	0.002
b_b	∞	0.9	0.9
α	0.27	0.27	0.27
β	0.55	0	0.55

4.1.1 Floating Energy Pile

The behavior of a floating energy pile with no end bearing restraint was investigated in this section, using the baseline parameters and the soil-structure interaction curve parameters given in Table 4.1. A load of 500 kN was first applied to the pile head, then a change in temperature of 20 °C was applied uniformly to the length of the energy pile. The

mechanical, thermal, and thermo-mechanical axial stresses for this pile are shown in Figure 4.1(a). In all of the following figures, when the term “thermal” is used, it is defined as the value obtained when subtracting the mechanical value from the thermo-mechanical value, which is useful to highlight the effect of temperature only.

It is clear from evaluation of the curves in Figure 4.1(a) that the axial stress is zero at the toe of the floating pile, because there is no end restraint at the toe. Heating was observed to lead to an increase in axial stress with depth, with the lowest increase near the toe. The axial stress at the head of the pile was observed to increase by 33% with the change in temperature. The mechanical, thermal, and thermo-mechanical axial strains for this pile are shown in Figure 4.1(b). It is clear from this figure that the mechanical axial strain is zero at the toe of the floating pile because there is no end restraint at the toe. Heating was observed to lead to expansive axial strains. The highest expansion is at the toe because there is less side shear resistance at shallow depths (near the surface) in the drained soil to restrain the axial expansion.

The mobilized side shear stresses are shown in Figure 4.1(c). It is clear that heating leads to a mobilization of friction in the energy pile. A positive mobilized side shear stress means a downward shear stress at the soil-pile interface. The mobilization with temperature is nonlinear because the T-z curve is nonlinear and is highly sensitive to displacement for small values of displacement. The greatest mobilized side shear stress is at the toe because the highest downward displacement accumulated from mechanical load and from thermal-induced expansion is at the toe.

The mechanical, thermal, and thermo-mechanical displacements are shown in Figure 4.1(d). It is clear that the pile was moving consistently downward (positive

displacement) with depth due to application of the mechanical load. The mechanical displacements decrease slightly with depth, because the axial mechanical stress decreases with depth, leaving less force for the pile to move down. The curve of thermal displacement indicates that the part of pile above 1.7 m moves upward and the part below moves downward when temperature is applied, which explain why the different between thermo-mechanical displacement and mechanical displacement.

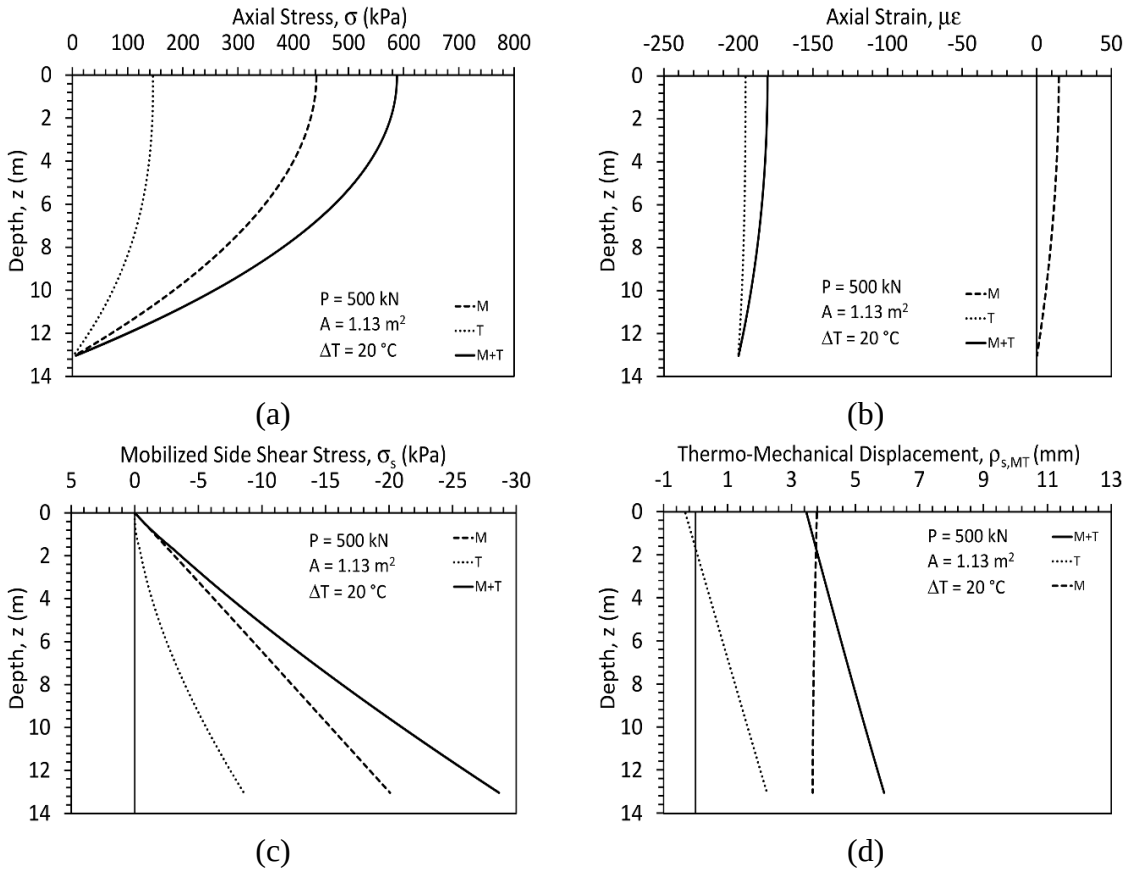

Figure 4.1: Soil-structure interaction behavior of a floating energy pile: (a) Axial stresses; (b) Axial strains; (c) Mobilized side shear stress; (d) Thermo-mechanical displacement

4.1.2 Pure End Bearing Pile

The behavior of an end-bearing energy pile was investigated in this section. In this case, the energy pile is assumed to have no side shear resistance with depth, and gains all

of its axial capacity from the toe of the energy pile. This pile has the same baseline parameters as those listed in Section 4.1. A load of 500 kN was first applied to the pile head, then a change in temperature of 20 °C was applied uniformly to the length of the energy pile.

The mechanical, thermal, and thermo-mechanical axial stresses for this pile are shown in Figure 4.2(a). Although there is no soil-structure interaction along the side of the end-bearing energy pile, there is still a head stiffness representing the stiffness of the overlying structure. Accordingly, the thermal stresses in the energy pile are not zero. In all of the following figures, when the term “thermal” is used, it is defined as the value when subtracting the mechanical value from the thermo-mechanical variable, which is useful to isolate the effects of temperature. It is clear from this figure that the axial stress does not change along the pile and is zero at the toe of the floating pile, because there is end restraint at the toe but no mobilized side shear stress along the side of the pile. Heating was observed to lead to an increase in axial compression stress, because the thermal expansion induced much restraint forced at the head and the toe of the pile. The axial stress at the head of the pile was observed to increase by 3.8% after the application of the change in temperature.

The mechanical, thermal, and thermo-mechanical axial strains for this pile are shown in Figure 4.2(b). All of these three curves is observed to keep constant along the pile. The axial thermal strain is slightly less than the strain of free expansion (which is -200 με at 20°C), because without friction at the side of the pile, the axial stress increased less during heating, and, thus generates less extra compressive strain to reduce the thermal expansion.

The mobilized side shear stresses are shown in Figure 4.2(c). The mobilized side shear stress is zero for all, because pure end-bearing pile does not have friction at side. The mechanical, thermal, and thermo-mechanical displacements are shown in Figure 4.2(d). It is clear that the pile was moving consistently downward (positive displacement) with depth under mechanical load. The thermal displacement curves show that the null point locates close to the top of pile, which also implies that the head stiffness is low comparatively to toe stiffness. The highest displacement is at the toe, and is increased by 26% after heating to 20°C.

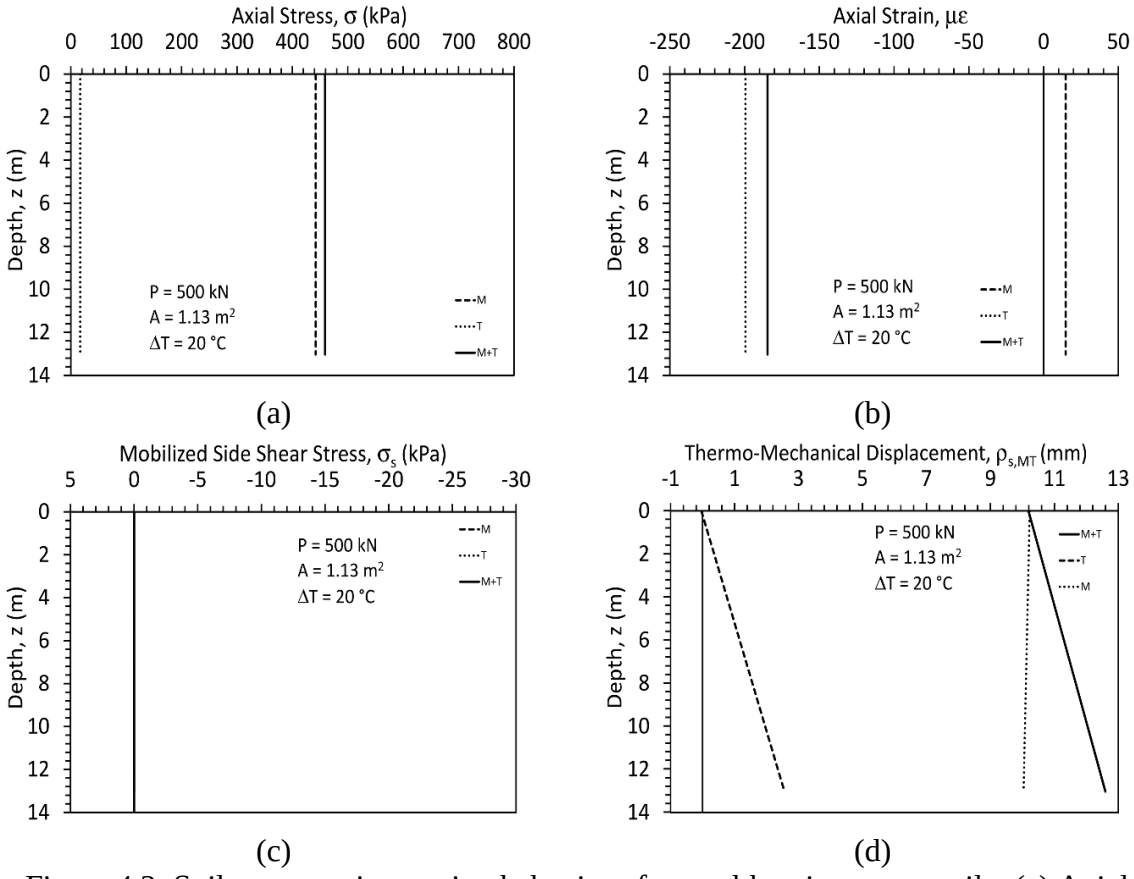

Figure 4.2: Soil-structure interaction behavior of an end-bearing energy pile: (a) Axial stresses; (b) Axial strains; (c) Mobilized side shear stress; (d) Thermo-mechanical displacement

4.1.3 Semi-Floating Energy Piles

The behavior of a semi-floating energy pile was investigated in this section. In this case, the energy pile is assumed to have both side shear resistance and end-bearing restraint. This pile has the same baseline parameters as those listed in Section 4.1. A load of 500 kN was first applied to the pile head, then a change in temperature of 20 °C was applied uniformly to the length of the energy pile. The mechanical, thermal, and thermo-mechanical axial stresses for this pile are shown in Figure 4.3(a). Accordingly, the thermal stresses in the energy pile are not zero. In all of the following figures, when the term "thermal" is used, it is defined as the value when subtracting the mechanical value from the thermo-mechanical variable, which is useful to isolate the effects of temperature. It is clear from this figure that the axial stress is not zero at the toe of the floating pile and the stress, strain, or displacement vary along the pile, because there are both mobilized side shear stress and end restraint at the toe involved. Heating was observed to lead to an increase in axial stress with depth, with the lowest increase near the toe. The axial stress was observed to increase by 62% at the head of the pile and by 58% at the toe of the pile.

The mechanical, thermal, and thermo-mechanical axial strains for this pile are shown in Figure 4.3(b). The difference between thermal axial strain and free expansion strain is much larger than it in end-bearing cases, because mobilized side shear stress leads to much larger compressive strain combined with the restrains from the head and toe of the pile to lower the thermal expansion. The thermal axial strain of the pile is closer to the free expansion strain as the depth increases, because the Thermo-Mechanical compression stress decreases as the depth increases, leading to less strain to diminish the expansion caused by heating.

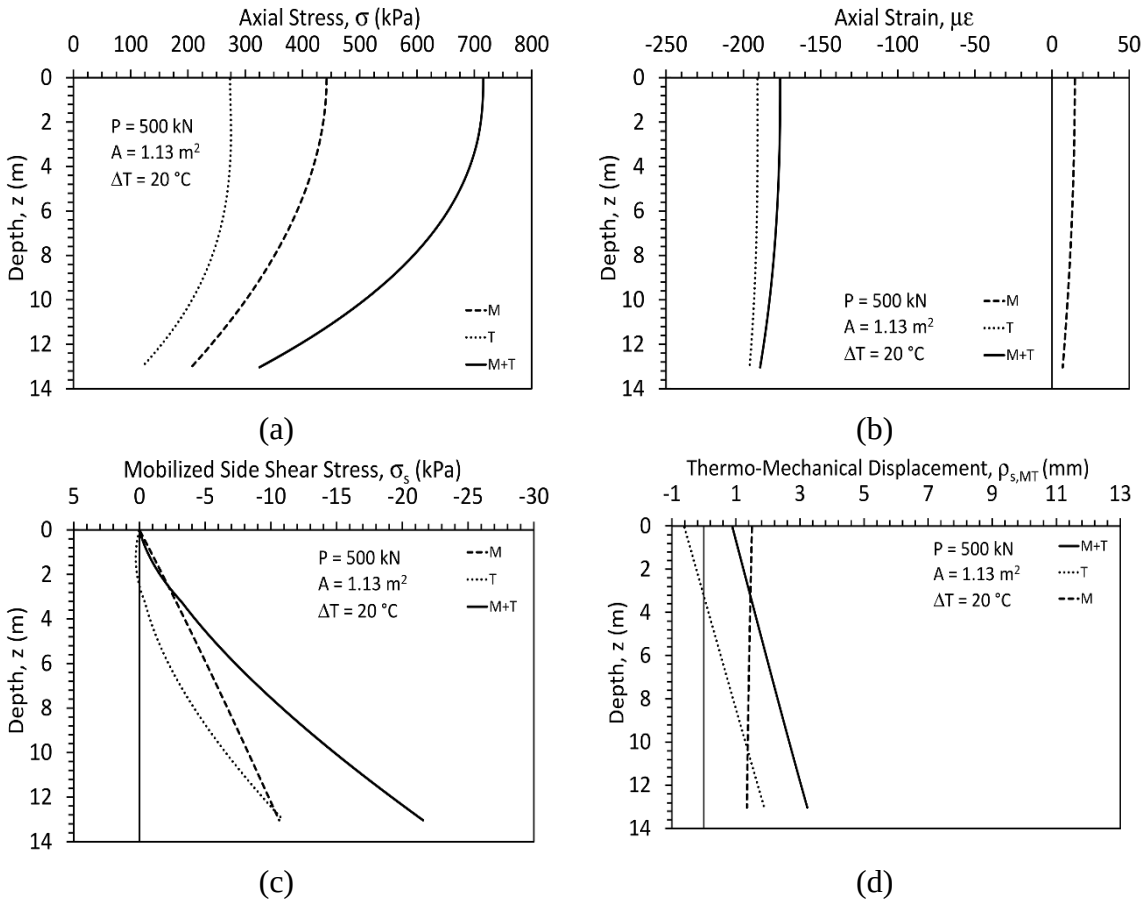

Figure 4.3: Soil-structure interaction behavior of a semi-floating energy pile: (a) Axial stresses; (b) Axial strains; (c) Mobilized side shear stress; (d) Thermo-mechanical displacement

The mobilized side shear stresses are shown in Figure 4.3(c). It is clear that heating leads to a mobilization of friction in the energy pile. Longer part of the pile is expansion upward after heating in this case than it in the pure floating case, because the null point in this case is at 2.8 m, deeper than the null point in pure floating case. The greatest mobilized side shear stress is at the toe, because the highest downward displacement accumulated from mechanical load and from thermal-induced expansion is at the toe.

The mechanical, thermal, and thermo-mechanical displacements are shown in Figure 4.3(d). It is clear that the pile was moving consistently downward (positive

displacement) with depth after mechanical loading. Although increased by 1.4 times after heating to 20 °C, the highest displacement after heating is the lowest in all of the cases.

4.1.4 Discussion

Although it is difficult to fairly compare the magnitudes of the thermal axial stresses, strains, and displacements between the three types of energy piles, the results presented in this section highlight the role of the end boundary conditions and side shear stresses on the soil-structure interaction behavior of energy piles. Comparing the results from the pure floating pile and end-bearing pile with the semi-floating pile, the semi-floating pile is observed to have the lowest settlement at the toe and the lowest head upward displacement induced by uniformly heating the pile. As semi-floating energy piles are the most common type of deep foundations encountered in practice, it is used as the baseline all future comparisons in this chapter.

4.2 Effect of Mechanical Load

A semi-floating energy pile with the same parameters used in Section 4.1 is considered in this section to evaluate the effect of mechanical load on thermo-mechanical response of an energy pile. In each type of soil, axial loads of 0, 100, 500, or 1000 kN was first applied to the pile head, then a change in temperature of 20 °C was applied uniformly to the length of the energy pile. The responses of this pile are shown in Figures 4.4 through 4.9 in the following sections.

4.2.1 Drained Soils

The thermo-mechanical and thermal axial stresses and strains for energy pile in drained soils are shown in Figures 4.4. From Figures 4.4(a) and 4.4(b), it can be observed that higher mechanical loads at the top lead to higher thermo-mechanical axial stresses and

lower thermo-mechanical axial strains drained soils, especially at the head of the pile. Figures 4.4(c) and 4.4(d) show that the larger the value of the applied mechanical load, the lower the thermal axial stress and the more thermal axial expansion the energy pile gains. This is because a pile under larger mechanical load and larger downward displacement trends to gain less mobilized side shear stress that can alleviate the thermal expansion as the stiffness softens with displacement.

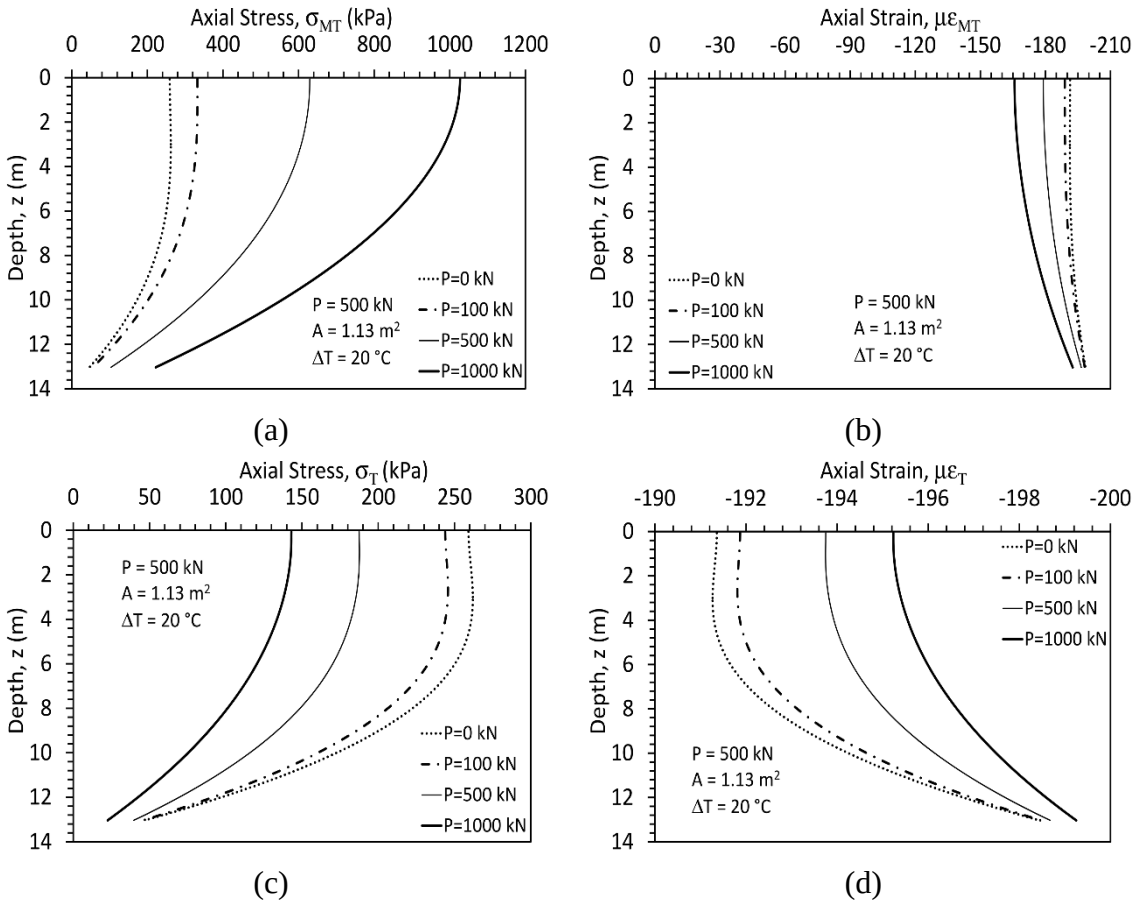

Figure 4.4: Soil-structure interaction behavior of a semi-floating energy pile in drained soils: (a) Thermo-mechanical axial stresses; (b) Thermo-mechanical axial strains; (c) Thermal axial stresses; (d) Thermal axial strains

The mechanical axial stresses and strains, mobilized side shear stress distributions, and thermo-mechanical displacement distributions for energy pile in drained soils are

shown in Figure 4.5. Figures 4.5(a) and 4.5(b) show that the increases of mechanical loads significantly increase the mechanical axial stress and mechanical axial compression stress along the pile in drained soil, especially at the head of pile. Both Figure 4.5(c) and 4.5(d) show that the increases of mechanical load lead to an upward shift of the NP. This is because the base stiffness decreases as the base settlement increases while the head stiffness remains constant. Further, the mobilized side shear stress with depth becomes more linear, because the part of T-z curve becomes more linear and flatten as displacement increases.

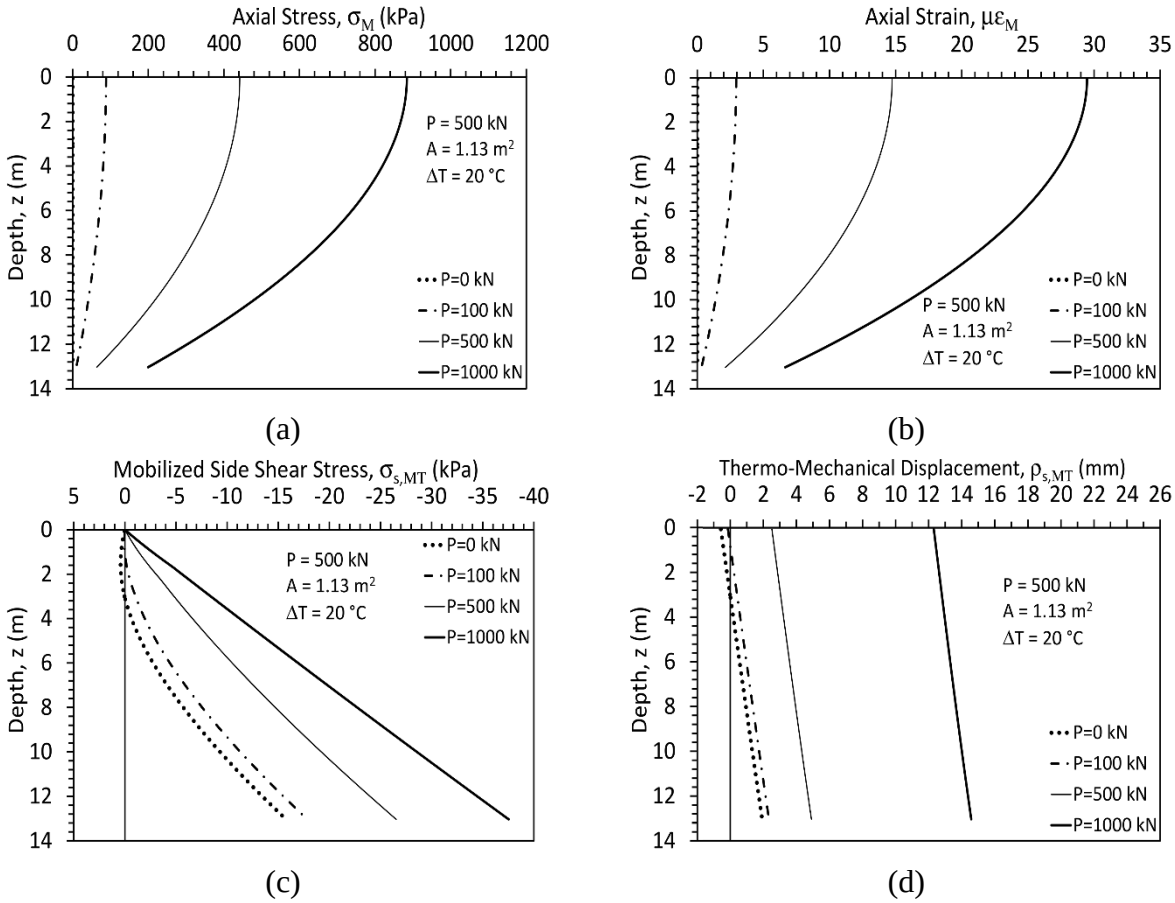

Figure 4.5 Soil-structure interaction behavior of a semi-floating energy pile in drained soils: (a) Mechanical axial stresses; (b) Mechanical axial strains; (c) Mobilized side shear stresses; (d) Thermo-mechanical displacements

4.2.2 Undrained Soils

The thermo-mechanical and thermal axial stresses and strains for an energy pile in undrained soils are shown in Figures 4.6(a) and 4.6(b). It also can be observed from Figure 4.6(a) that the increases of mechanical load under undrained condition lead to an increasing of thermo-mechanical axial stress along the energy pile, especially at the head of energy pile, and Figure 4.6(b) shows that thermo-mechanical axial expansion decreases with an increase of mechanical load. The profile of thermo-mechanical axial strain is more linear for undrained condition than for drained condition, because in undrained soil, the ultimate side skin resistance does not vary with depth.

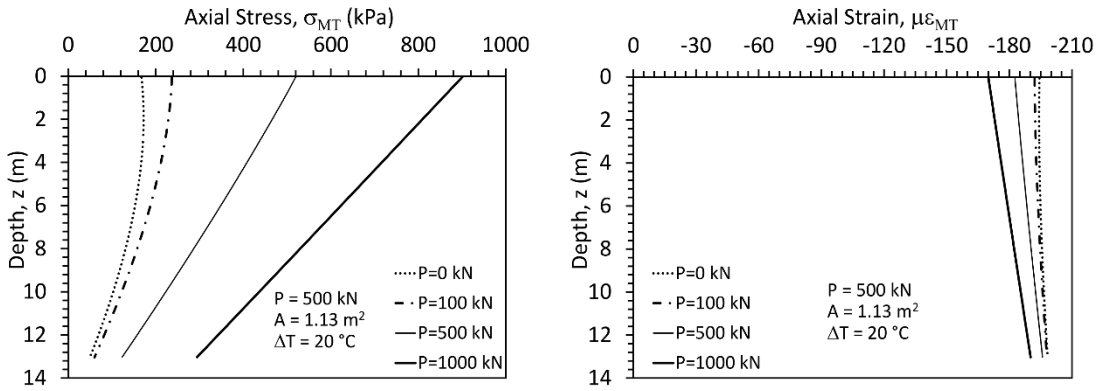

(a) (b)

Figure 4.6 Soil-structure interaction behavior of a semi-floating energy pile in undrained soils: (a) Thermo-mechanical axial stresses; (b) Thermo-mechanical axial strains;

The thermal axial stresses and strains and mechanical axial stresses and strains are shown in Figure 4.7. Figures 4.7(a) and 4.7(b) show that the increases of mechanical load reduce thermally-induced axial stresses and thermally-induced axial strains along the energy pile. Figures 4.7(c) and 4.7(d) shows the profiles of mechanical axial stresses and strains are quite linear and the mechanical stresses and strains decrease with depth as side skin friction reduces the load from upper part of pile.

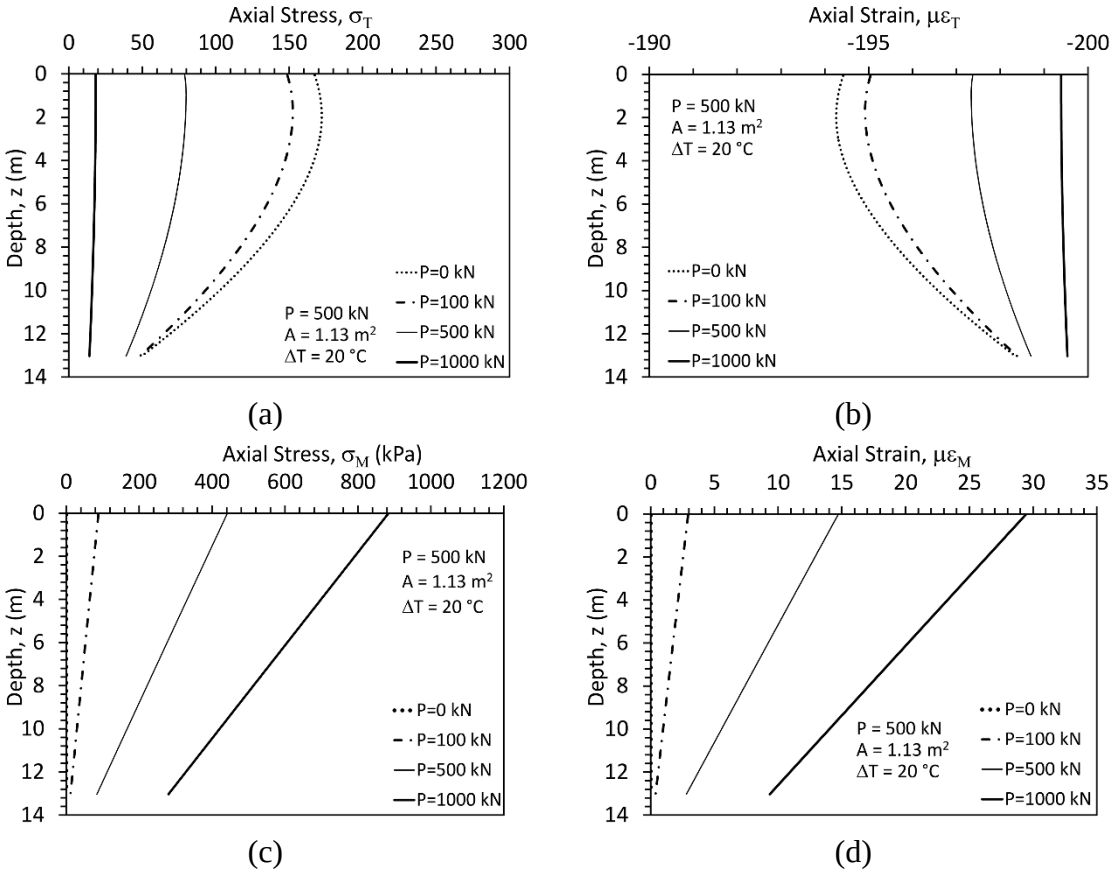

Figure 4.7 Soil-structure interaction behavior of a semi-floating energy pile in undrained soils: (a) Thermal axial stresses; (b) Thermal axial strains; (c) Mechanical axial stresses; (d) Mechanical axial strains

The thermo-mechanical mobilized side shear stresses and displacement along the energy pile are shown in Figure 4.8. It can be clearly observed from Figure 4.8(a) that the depth of null point moves upward with an increase of mechanical load. In Figure 4.8(a), discontinuities in the curves are observed, especially in the large mechanical-load case. This discontinuity is at the turning point, which reflects the change of mobilized side shear stress when pile is moving downward from when the pile is moving upward after heating. The Figure 4.8(b) shows that the increases of mechanical load lead to significant thermo-mechanical axial displacement, especially when mechanical is large. This is because larger

mechanical load leads to the stiffness at tip and at side-skin becomes lower, as shown in Q-z curve and T-z curve in Figure 3.4 in Chapter 3.

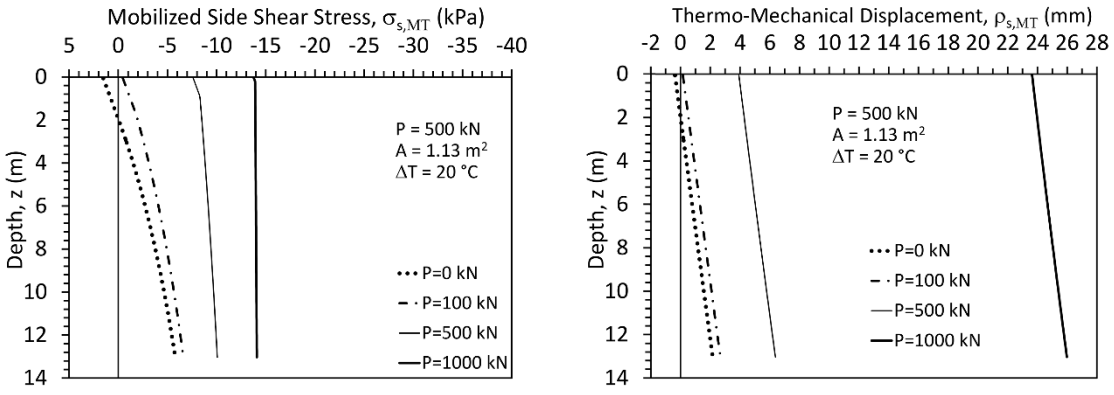

(a) (b)

Figure 4.8 Soil-structure interaction behavior of a semi-floating energy pile in undrained soils: (a) Mobilized side shear stresses; (b) Thermo-mechanical displacements

4.2.3 Synthesis of the Impact of Mechanical Load

Some key aspects of energy pile performance in terms of mechanical, thermal, and thermo-mechanical axial stress and displacement are selected and are shown in Figures 4.9(a) and 4.9(b). It is clear from Figure 4.9(a) that the maximum axial stress brought in by thermal expansion decreases as the mechanical load increases. From Figure 4.9(b), the mechanical load leads to an increase in the thermo-mechanical displacement, and the rate of increase becomes larger when larger loads are applied. The nonlinearity observed in Figure 4.9(b) is due to the fact that when mechanical loads are large, the resistant forces at the sides and toe are supposed to be large, which required large displacements. Since the slopes of the Q-z and T-z curves reflect nonlinear softening with increasing displacement, much more displacement is necessary.

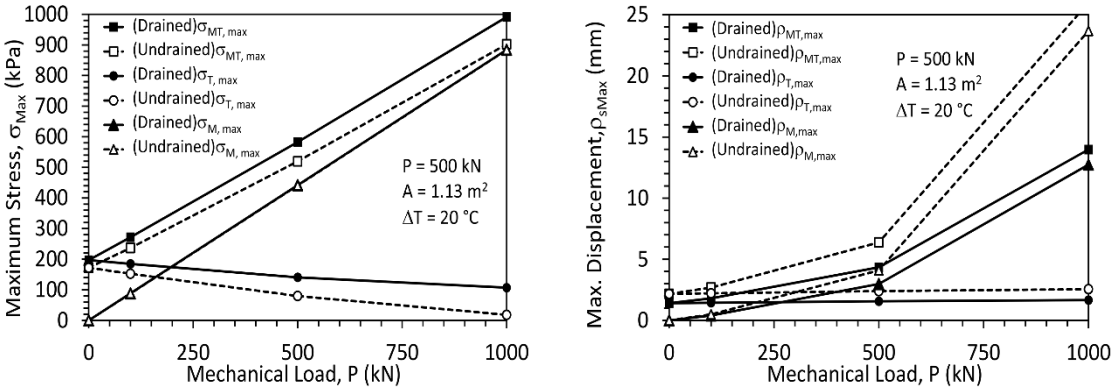

(a) (b)

Figure 4.9: Comparison of the impact of mechanical load on soil-structure interaction behavior: (a) Max. axial stresses vs. mechanical loads; (b) Max. displacements vs. mechanical loads

4.3 Effect of Soil Shear Strength Parameters

A semi-floating energy pile with the same parameters used in Section 4.1 is considered in this section to evaluate the effect of mechanical load on thermo-mechanical response of an energy pile in two types of soils. For drained soils having drained friction angles of 20°, 25°, 30° or 35°, a load was first applied to the pile head then a change in temperature of 20 °C was applied uniformly to the length of the energy pile. The response for this pile in drained and undrained soils are shown in Figures 4.10 through 4.15.

4.3.1 Drained Soils – Effect of Friction Angle

The thermo-mechanical, thermal axial stresses and strain for energy pile under varying friction angle for energy pile in drained soils are shown in Figures 4.10(a) through 4.10(d). It is clear from Figure 4.10(a) that the thermo-mechanical axial stresses increases with an increase of friction angle, especially at the head of pile. Figure 4.10(b) shows that the axial thermo-mechanical stresses at the head increase with an increase of drained friction angle. Figure 4.10(c) shows that the thermal axial stresses increases with an increase of friction angle. Figure 4.10(d) shows that thermal induced strains at the head

decrease with an increase of drained friction angle. This is because mobilized side shear force increases with an increase of drained friction angle (see Figure 4.11(c)). The results in Figure 4.10(d) also indicate that heating has an insignificant effect on thermal axial strain.

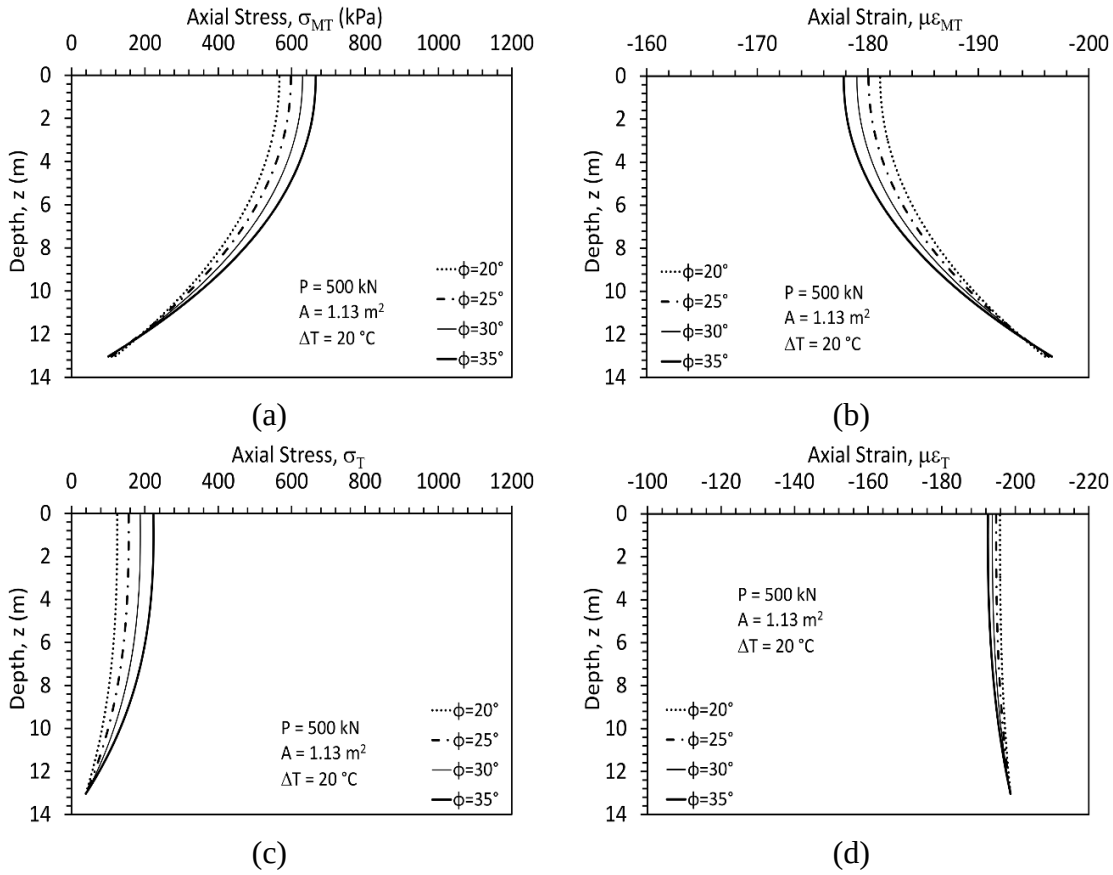

Figure 4.10: Soil-structure interaction behavior of a semi-floating energy pile in drained soils: (a) Thermo-mechanical axial stresses; (b) Thermo-mechanical axial strains; (c) Thermal axial stresses; (d) Thermal axial strains

The mechanical axial stresses and strains, mobilized side shear stress distributions, and thermo-mechanical displacement distributions under varying friction angle for energy pile in drained soils for energy pile in drained soils are shown in Figures 4.11. The results in Figures 4.11(a) and 4.11(b) indicate that drained friction angle has a slight influence on mechanical axial stress. Figure 4.11(c) shows that the fiction angle does not affect the mobilized side shear stresses at the head of pile. As the depth increases the mobilized side

shear stresses increase with an increase of friction angle. The maximum mobilized side shear stresses exist at the base of pile. The results in Figure 4.11(d) indicate that the thermo-mechanical displacement decreases with an increase in drained friction angle, and the influence of drained friction angle on displacement becomes insignificant when the drained friction angle is large.

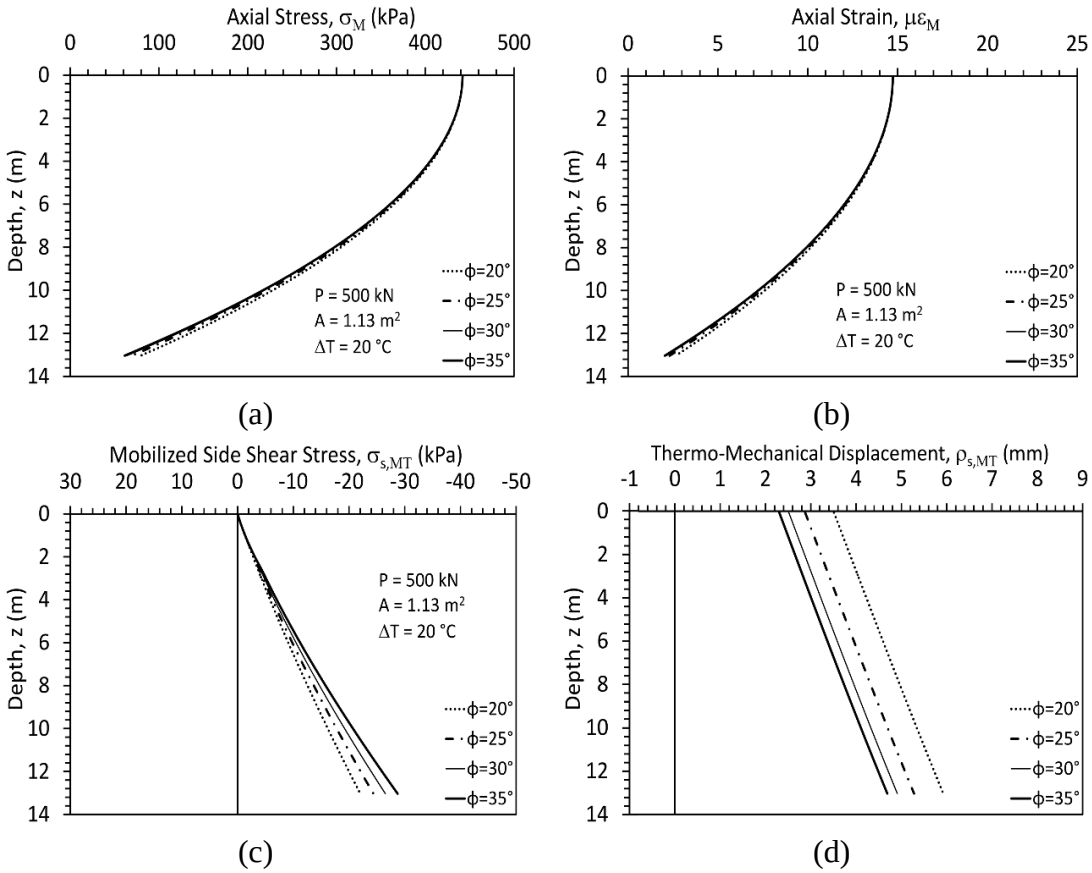

Figure 4.11: Soil-structure interaction behavior of a semi-floating energy pile in undrained soils: (a) Mechanical axial stress; (b) Mechanical axial strains; (c) Mobilized side shear stresses; (d) Thermo-mechanical displacements

The maximum thermo-mechanical, thermal, mechanical stress and maximum displacement under varying friction angle values for energy pile in drained soils are shown in Figures 4.12(a) and 4.12(b). It can be observed from figure 4.12(a) that the thermo-mechanical stresses increase linearly with an increase of drained friction angle ranging

from 25° to 35°, and the largest thermo-mechanical stress is close to the head of pile. Figure 4.12(b) shows that maximum thermo-mechanical displacement decreases with an increases of drained friction angle, and the effect of drained friction angle on the maximum displacement becomes small when the friction angle is large. This is because the ultimate side shear stress increases nonlinearly with increases in the friction angle, which leads to larger axial stresses to resist the axial displacement caused by thermal expansion.

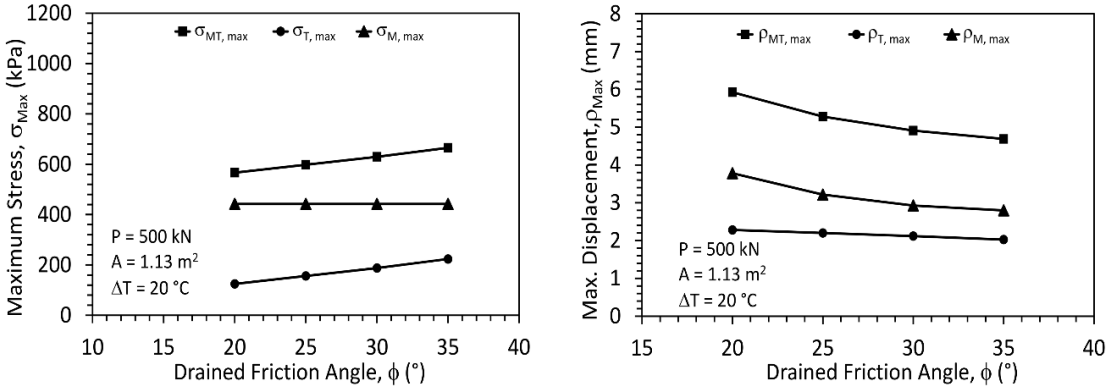

(a) (b)

Figure 4.12: Soil-structure interaction behavior of a semi-floating energy pile in drained soils: (a) Max. stresses vs. ϕ; (b) Max. displacements vs. ϕ

4.3.2 Undrained Soils – Effect of Undrained Shear Strength

The thermo-mechanical and thermal axial stresses and strain under varying undrained shear strength for energy pile in undrained soils are shown in Figures 4.13(a) through 4.13(d). It is clear from Figures 4.13(a), 4.13(c) that the axial thermo-mechanical stresses and thermal stresses increase with an increase in undrained shear strength. Figures 4.13(b) and 4.13(d) shows that the thermo-mechanical stresses and thermal induced expansions decrease with an increases of undrained shear strength. As undrained shear strength increases the profiles of thermo-mechanical and thermal axial stresses and strains become nonlinear. The axial thermo-mechanical strain and thermal strain decrease with an

increase of undrained shear strength, and that increase in temperature leads to the null point moving downward and thermo-mechanical stresses and strains increase.

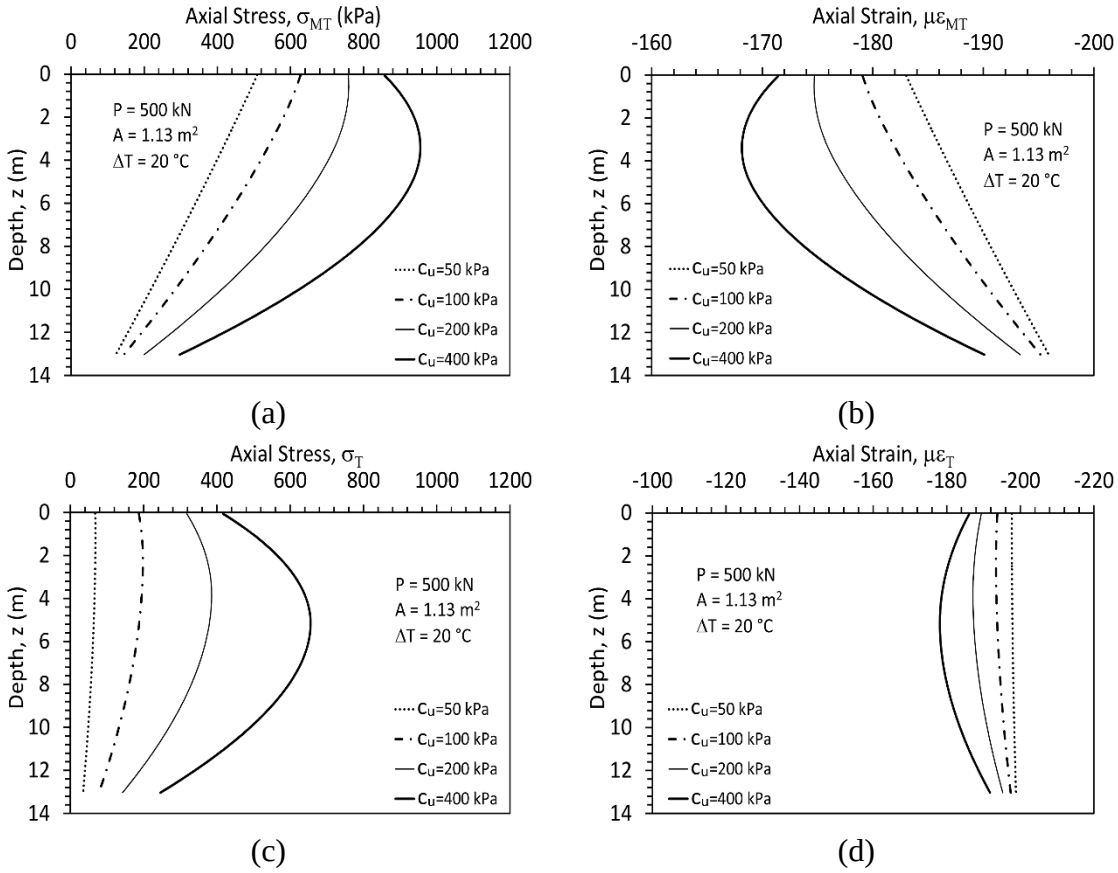

Figure 4.13: Soil-structure interaction behavior of a semi-floating energy pile in undrained soils: (a) Thermo-mechanical axial stresses; (b) Thermo-mechanical axial strains; (c) Thermal axial stresses; (d) Thermal axial strains

The mechanical axial stresses and strain, thermo-mechanical mobilized side shear stresses and displacements under varying undrained shear strength for energy pile in undrained soils are shown in Figures 4.14(a) through 4.14(d). Figures 4.14(a) and 4.14(b) show that the change of undrained shear strength does not have much influence on mechanical stresses and strains. Figure 4.14(c) shows that the increase of undrained shear strength leads to significant increase in mobilized side shear stress for the part below the null point where the part of energy pile moves downward and to significant decrease for

the part above the null point where the part moves upward. Figure 4.14(d) shows that the thermo-mechanical displacement and the ratio of this change decreases with an increase of undrained shear strength.

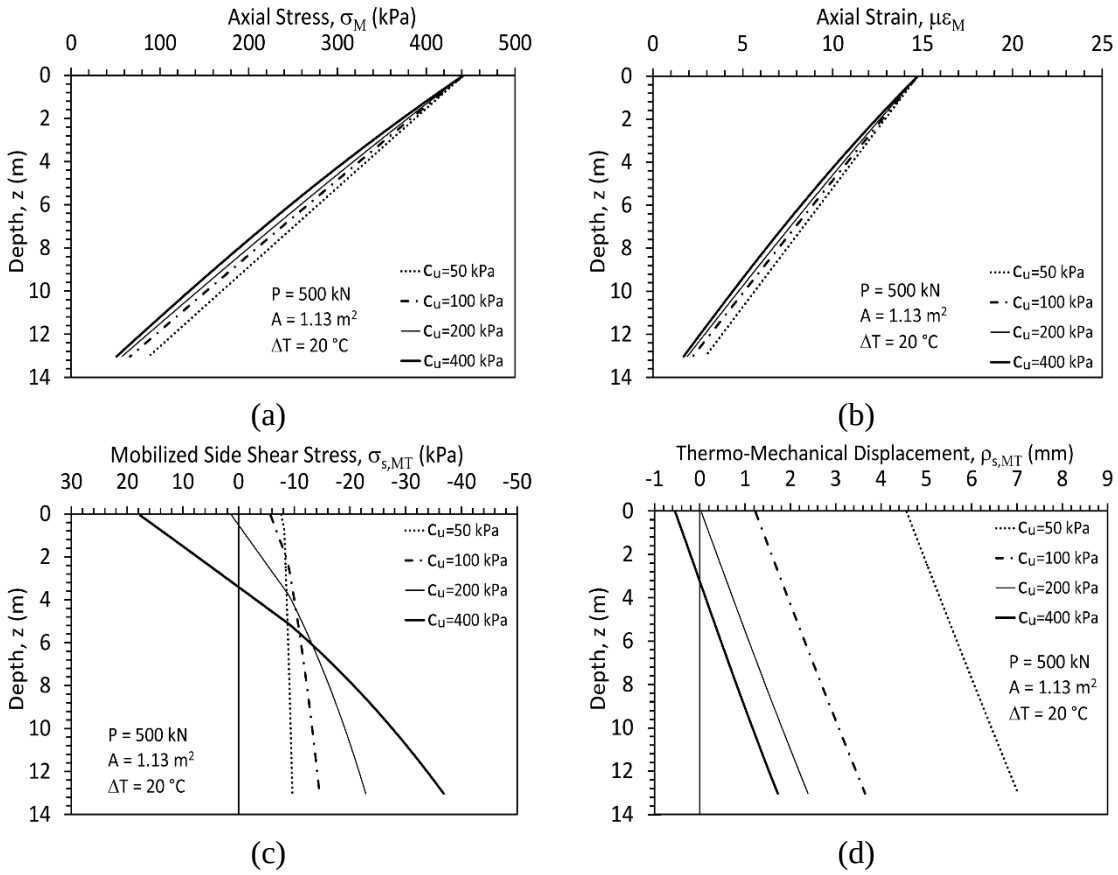

Figure 4.14: Soil-structure interaction behavior of a semi-floating energy pile in undrained soils: (a) Mechanical axial stress; (b) Mechanical axial strains; (c) Mobilized side shear stresses; (d) Thermo-mechanical displacements

The maximum thermo-mechanical, thermal and mechanical stresses and maximum displacement for varying undrained shear strength values in cohesive soils are shown in Figure 4.15. Figure 4.15(a) shows the maximum thermo-mechanical stress in pile increases with an increase of undrained shear strength of soil while maximum mechanical stress is quite insensitive to shear strength of soil. The maximum thermo-mechanical stress when undrained shear strength is at 400 kPa is approximately 2 times larger than it when

undrained shear strength is at 50 kPa. Figure 4.15(b) shows that the thermo-mechanical displacement decreases with an increase of undrained shear strength, because an increase of undrained shear strength leads to an increase of mobilized side shear stress and toe resistant force which compress the pile to lower the displacements. Besides, the influence of the shear strength on maximum displacements becomes insignificant when shear strength is large, because of the nonlinearity of T-z curve. When the ultimate mobilized side shear stress is amplified by increasing c_u, less displacement is required for side shear stresses to holding the pile. Since the T-z curve stiffen with a decrease of displacement, a smaller downward movement of pile is able to achieve the large enough side shear stress to hold the pile. The maximum thermo-mechanical displacement when undrained shear strength is at 50 kPa is approximately 4 times larger than it when undrained shear strength is 400 kPa.

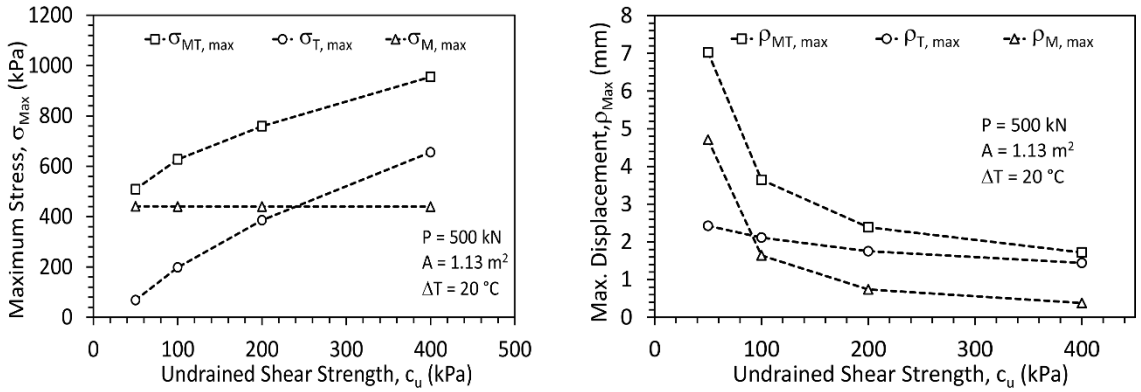

Figure 4.15: Soil-structure interaction behavior of a semi-floating energy pile in undrained soils: (a) Maximum stresses vs. c_u; (b) Maximum displacements vs. c_u

4.4 Effect of Temperature

A semi-floating energy pile with the same parameters is considered in this section. For each type of soil, a load of 500 kN was first applied to the pile head, then a change in

temperature of 5 °C, 10 °C, 20 °C, 30 °C, 40 °C or 50 °C was applied uniformly to the length of the energy pile. The responses for this pile are shown in Figure 4.16 through 4.20.

4.4.1 Drained Soils

The thermo-mechanical, thermal induced axial stresses and strain under varying temperature for energy pile in drained soils are shown in Figures 4.16(a) through 4.16(d).

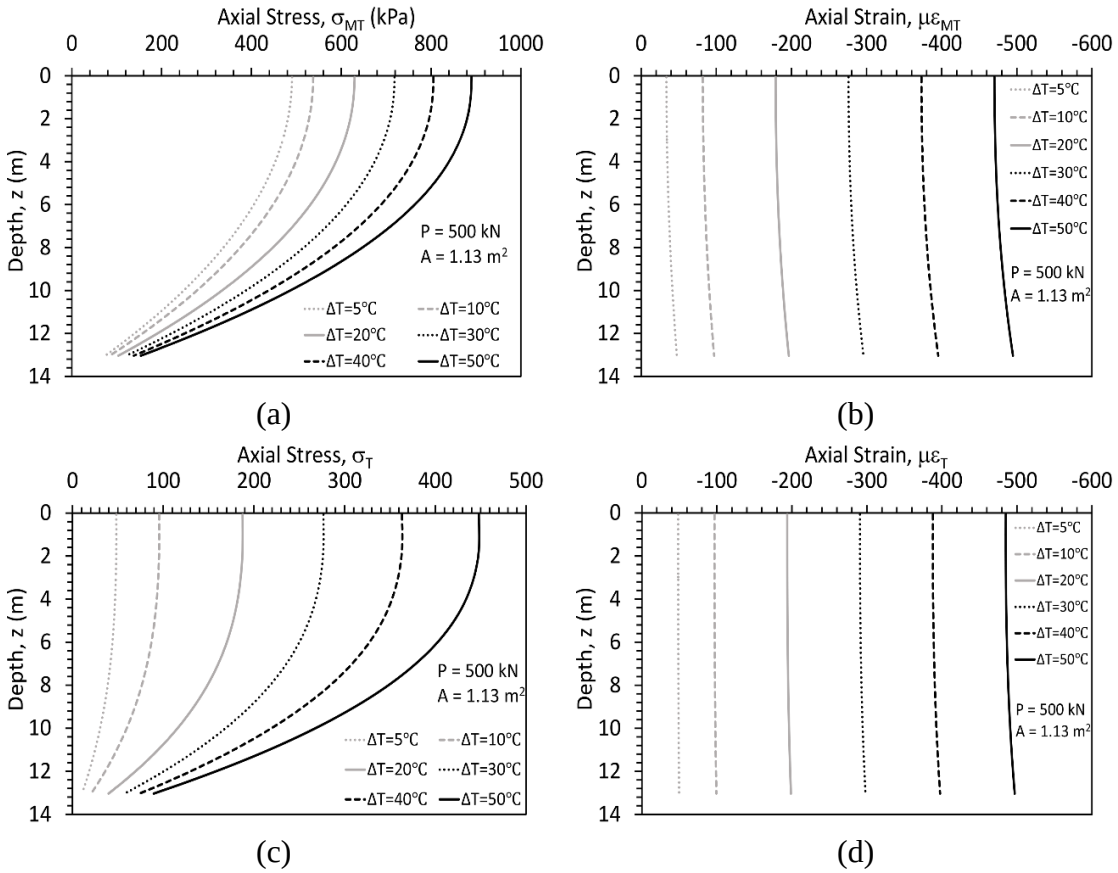

Figure 4.16: Soil-structure interaction behavior of a semi-floating energy pile in drained soils: (a) Thermo-mechanical axial stresses; (b) Thermo-mechanical axial strains; (c) Thermal axial stresses; (d) Thermal axial strains

It is clear from Figures 4.16(a) and 4.16(c) that thermo-mechanical axial stresses and thermal induced axial compressive stresses increase linearly with an increase of temperature. These increases are more substantial at the head of the pile rather than toe of the pile, yet thermo-mechanical stresses are larger in drained soils than in undrained soils.

Figures 4.16(b) and 4.16(d) shows that thermo-mechanical strains and thermal strains increase linearly with increases in temperature.

The mechanical axial stresses and strains, thermo-mechanical mobilized side shear stresses and displacements under varying temperature for energy pile in drained soils are shown in Figures 4.17(a) through 4.17(d). Figures 4.17(a) and 4.17(b) illustrate the behavior of mechanical axial stresses and strains responding to different temperature under different soil condition, respectively. It is observed that all 6 curves of are overlapped in either Figures 4.17(a) or 4.17(b) because temperature does not influence on the mechanical axial stress or strain. Figure 4.17(c) shows the influence of temperature on mobilized side shear stress in drained soil. It can be observed from this figure that the increase of temperature leads to an increase of mobilized side shear stresses, especially in deeper part of energy pile. Figure 4.17(d) shows that the change of temperature does not change the position of null point. With an increases of change of temperature, the thermo-mechanical displacement for part of energy pile below the null point increases and for the part above null point decreases. The transition at approximately 2 m observed in Figure 4.17(d) indicates that the upper part of the energy pile is unloading and the lower part is loading.

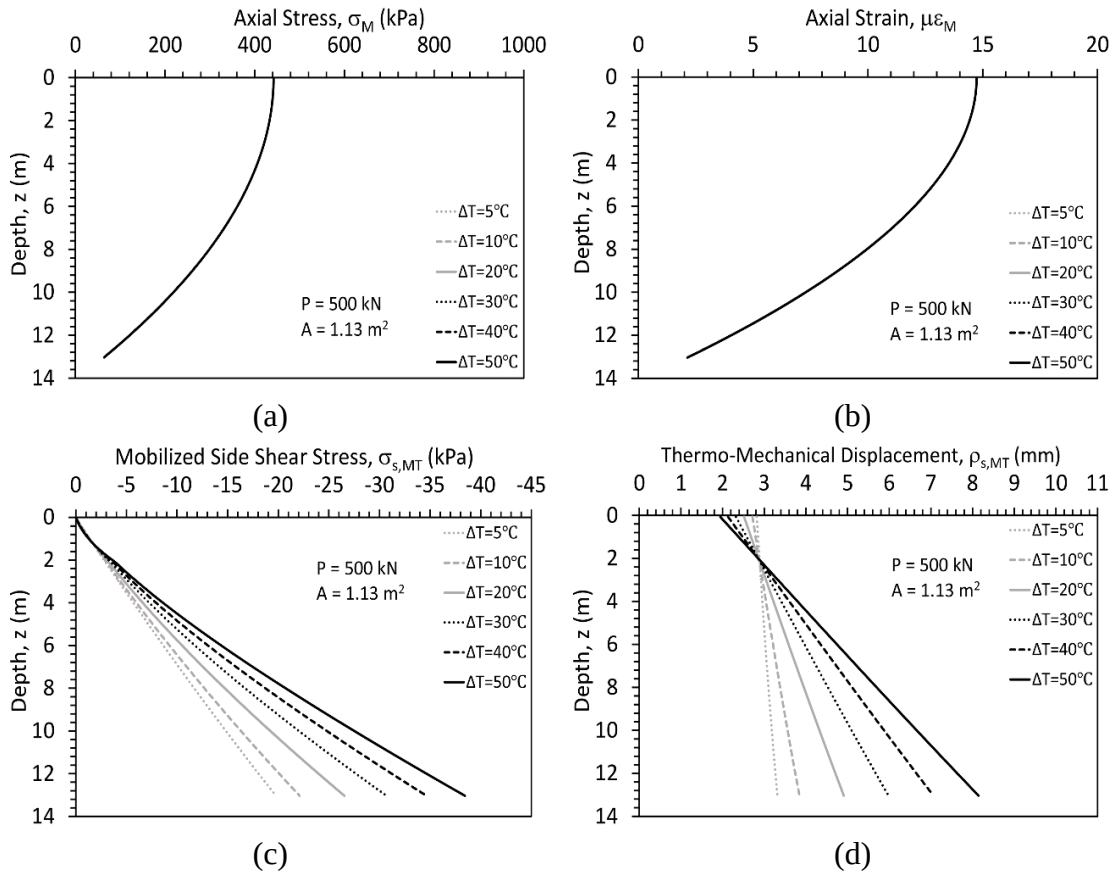

Figure 4.17: Soil-structure interaction behavior of a semi-floating energy pile in drained soils: (a) Mechanical axial stresses; (b) Mechanical axial strains; (c) Mobilized side shear stresses; (d) Thermo-mechanical displacements

4.4.2 Undrained Soils

The thermo-mechanical, thermal induced axial stresses and strain under varying temperature for energy pile in undrained soils are shown in Figures 4.18(a) through 4.18(d). It can be observed from Figures 4.18(a) and 4.18(c) that the thermo-mechanical, thermal induced axial stresses approximately linearly increase with increases of change of temperature. These increases are more substantial at the head of the pile rather than toe of the pile. Figures 4.18(b) and 4.18(b) show that thermo-mechanical strains and thermal strains linearly increase with an increase of temperature.

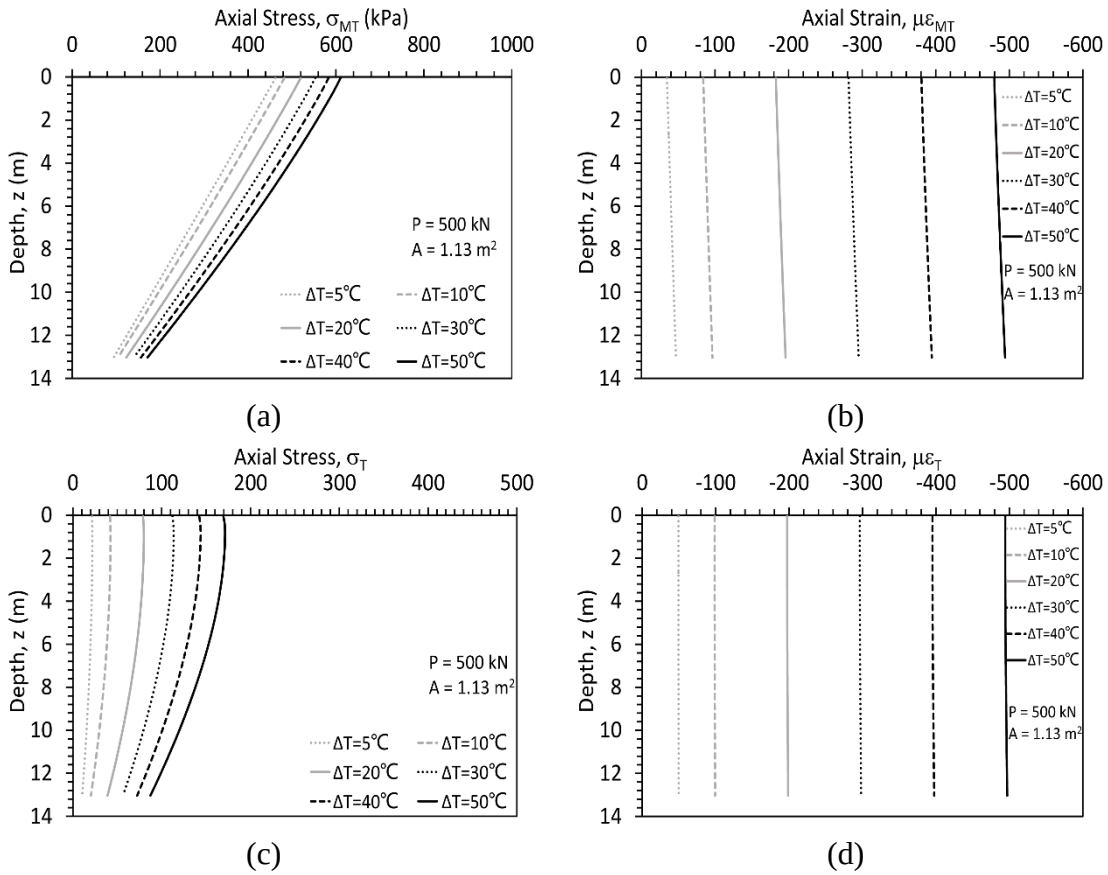

Figure 4.18: Soil-structure interaction behavior of a semi-floating energy pile in undrained soils: (a) Thermo-mechanical axial stresses; (b) Thermo-mechanical axial strains; (c) Thermal axial stresses; (d) Thermal axial strains

The mechanical axial stresses and strain, thermo-mechanical mobilized side shear stresses and displacements under varying temperature for energy pile in undrained soils are shown in Figures 4.19(a) through 4.19(d). Figures 4.19(a) and 4.19(c) show that the change of temperature has no effect on mechanical axial stresses and strains. Figure 4.19(c) shows the influence of temperature on mobilized side shear stress in drained soil. Different from the case in drained soils, the mobilized side shear stresses at head is not zero because ultimate side shear stress in undrained soils is non-zero constant value along the pile, but drained soils is proportional to vertical earth pressure which is zero at the top. The transition at 1.75 m observed in Figure 4.19(c) indicates that the upper part of the energy pile is

unloading and the lower part is loading. Figure 4.19(d) shows that the thermo-mechanical displacement linearly increases with an increase of change of temperature for the part of energy pile below the null point, and decreases for the part above the null point.

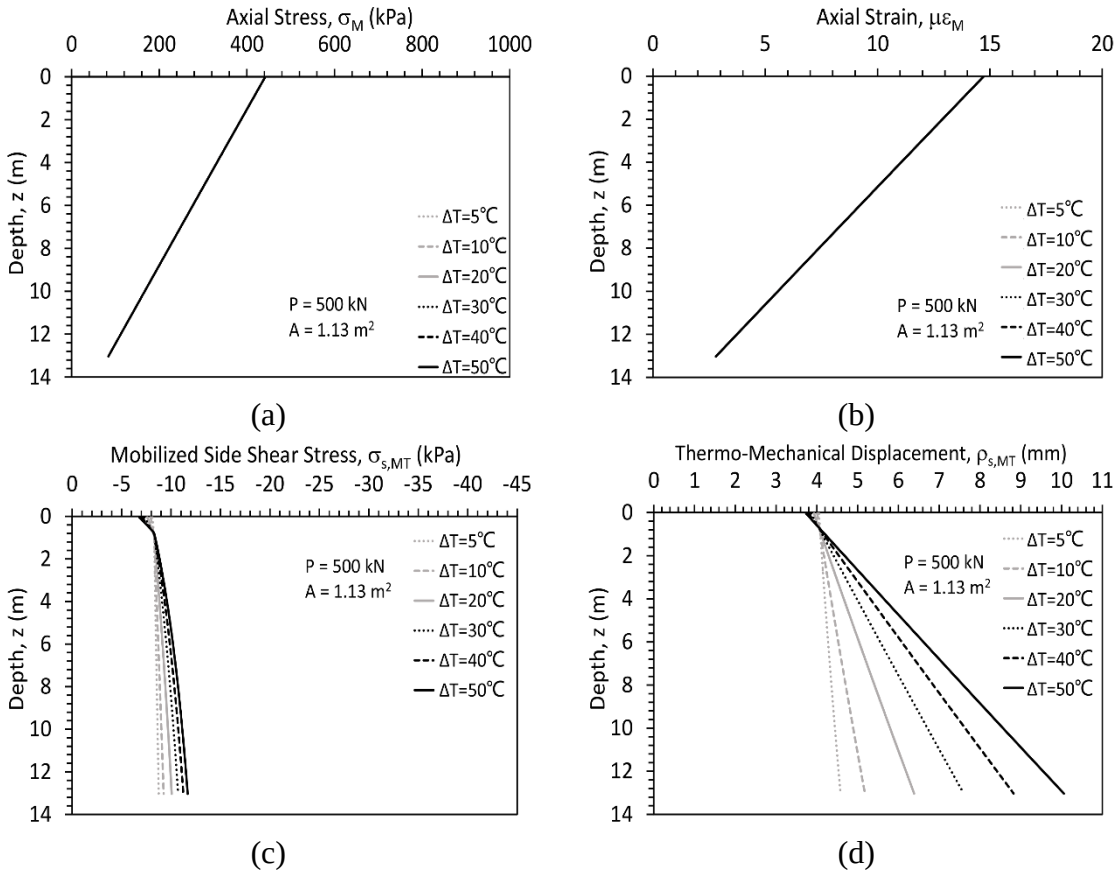

Figure 4.19: Soil-structure interaction behavior of a semi-floating energy pile in undrained soils: (a) Mechanical axial stresses; (b) Mechanical axial strains; (c) Mobilized side shear stresses; (d) Thermo-mechanical displacements

4.4.3 Synthesis of the Impact of Temperature Change

Maximum values of axial stress and displacement in terms of mechanical, thermal, and thermo-mechanical axial are shown in Figures 4.20(a) and 4.20(b), respectively. Figures 4.20(a) and 4.20(b) show that the maximum axial stress increases quite linearly with an increase of temperature, but maximum displacement increases faster with an increases of temperature. This is because the temperature effect in the soil-structure

interaction model is linear. A pile has lower maximum thermo-mechanical axial stress but larger maximum thermo-mechanical displacement in undrained soils than in drained soils.

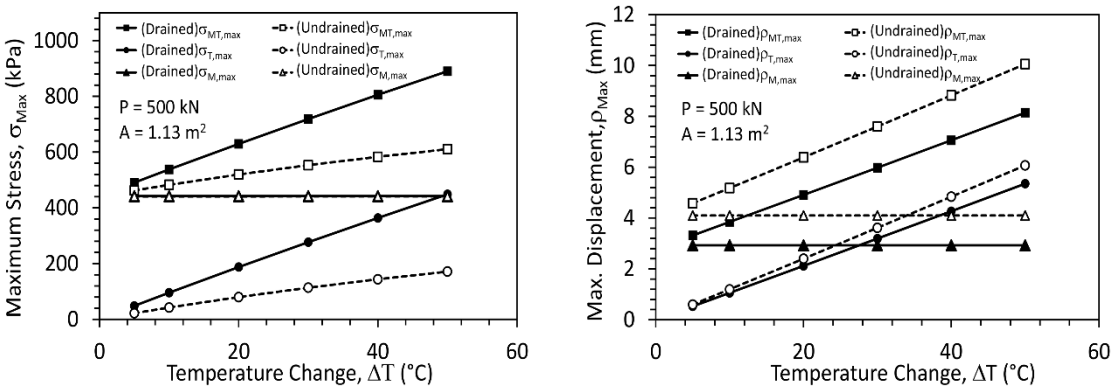

(a) (b)

Figure 4.20: Comparison of the impact of temperature on soil-structure interaction behavior: (a) Max. stresses vs. temperatures; (b) Max. displacement vs. temperatures

4.5 Effect of Toe Stiffness

A semi-floating energy pile with the same parameters is considered in this section. For each type of soil, a load of 500 kN was first applied to the pile head, then a change in temperature of 20 °C was applied uniformly to the length of the energy pile. Parameters a_b of 0.001, 0.005, 0.01, 0.05, 0.1 or 0.25 and b_b of 0.9 are used to determine the toe stiffness. The response for this pile are shown in Figure 4.21 through 4.25.

4.5.1 Drained Soils

The thermo-mechanical, thermal induced axial stresses and strain under different toe stiffness condition for energy pile in drained soils are shown in Figures 4.21(a) through 4.21(d). it is clear from Figures 4.21(a) and 4.21(c) that the thermo-mechanical and thermal induced axial stresses decrease with an increase of toe stiffness parameter a_b. Figures 4.21(b) and 4.21(d) show that the thermo-mechanical and thermal induced axial expansions increase with an increase of a_b. The influence of a_b on thermo-mechanical, thermal induced

axial stresses and strains become insignificant when a_b is large. These are because the initial slope of the Q-z curve decreases with an increase in a_b, which leads to more mobilized side shear stress to alleviate the settlement from lower end bearing reaction.

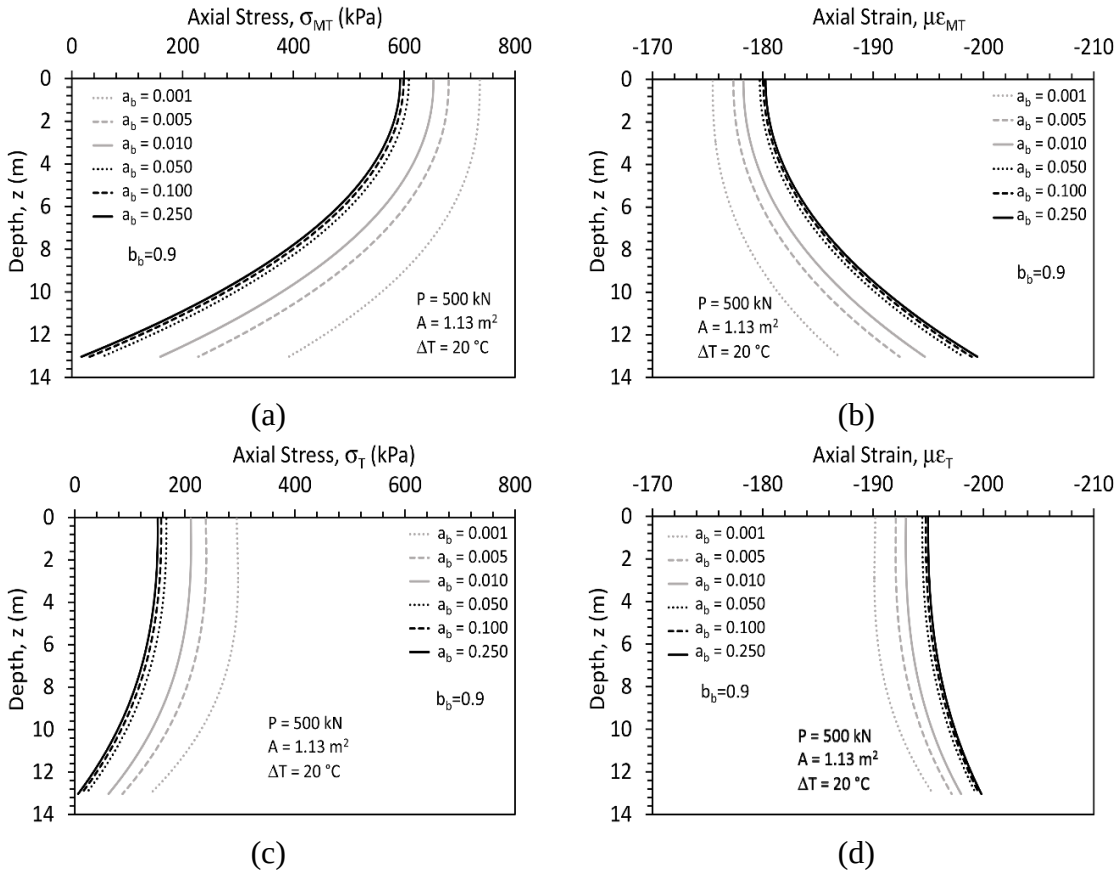

Figure 4.21: Soil-structure interaction behavior of a semi-floating energy pile in drained soils: (a) Thermo-mechanical axial stresses; (b) Thermo-mechanical axial strains; (c) Thermal axial stresses; (d) Thermal axial strains

The mechanical axial stresses and strain, thermo-mechanical mobilized side shear stresses and displacements under different toe stiffness condition for energy pile in drained soils are shown in Figures 4.22(a) through 4.22(d). Figures 4.22(a) and 4.22(b) show that the mechanical axial stresses and strain keep constant at the head of energy pile and decrease with depth as a_b increases. Also, the influence of a_b on mechanical axial stresses and strains become insignificant when a_b is large as explained before. Figures 4.22(c) and

4.22(d) indicate that the mobilized side shear stress and thermo-mechanical displacement increases with an increase of a_b, because decrease of base stiffness lead to larger settlement which induced more side friction at the interface between pile and soil.

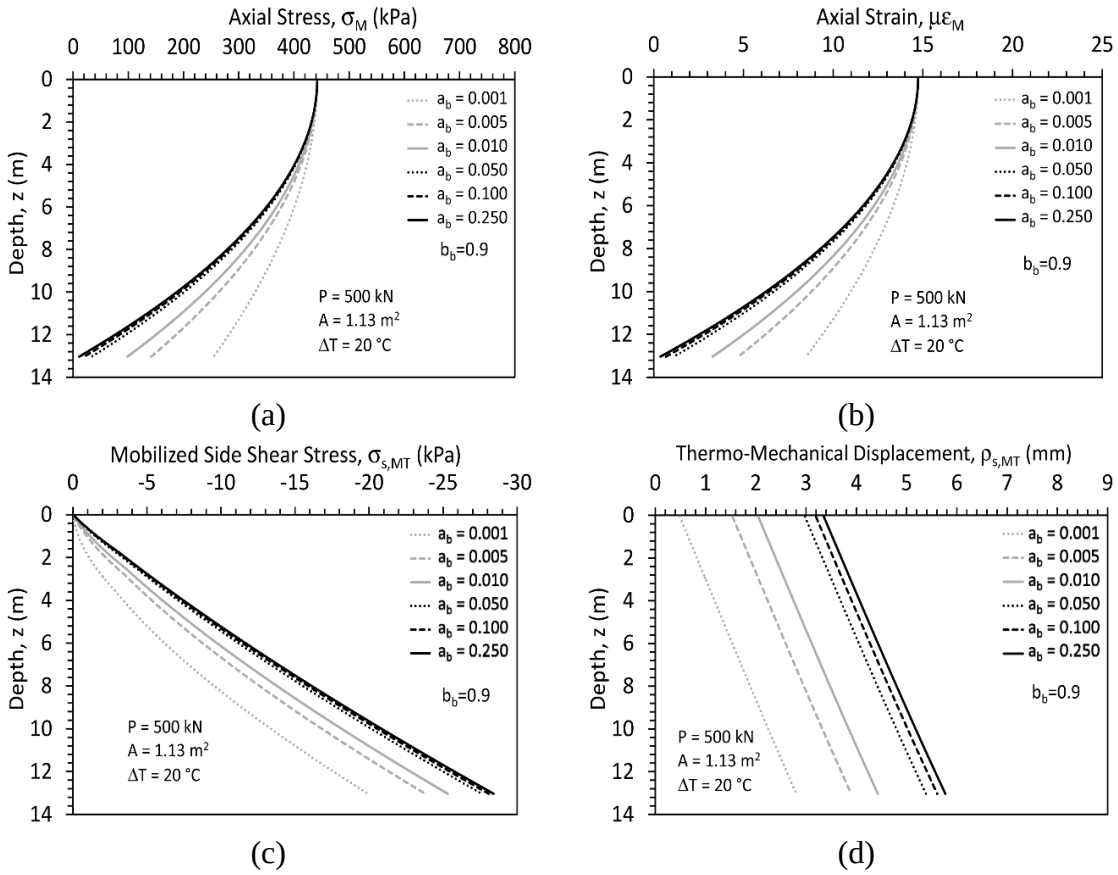

Figure 4.22: Soil-structure interaction behavior of a semi-floating energy pile in drained soils: (a) Mechanical axial stresses; (b) Mechanical axial strains; (c) Mobilized side shear stresses; (d) Thermo-mechanical displacements

4.5.2 Undrained Soils

The thermo-mechanical, thermal induced axial stresses and strain under different toe stiffness condition for energy pile in undrained soils are shown in Figures 4.23(a) through 4.23(d). It can be observed from Figures 4.23(a) and 4.23(c) that the thermo-mechanical and thermal induced axial stresses decreases with an increase of a_b. Figures

4.23(b) and 4.23(d) shows that the thermo-mechanical and thermal induced axial expansions increase with an increase of a_b.

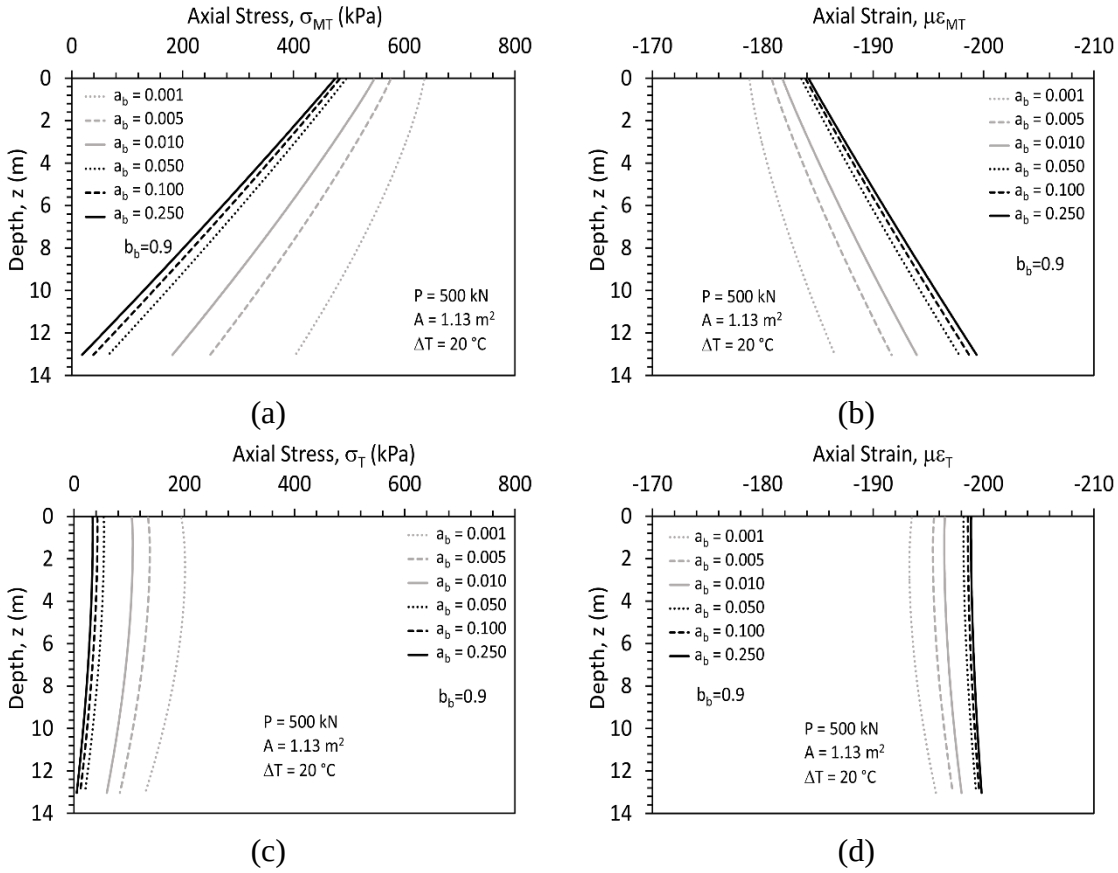

Figure 4.23: Soil-structure interaction behavior of a semi-floating energy pile in undrained soils: (a) Thermo-mechanical axial stresses; (b) Thermo-mechanical axial strains; (c) Thermal axial stresses; (d) Thermal axial strains;

The mechanical axial stresses and strain, thermo-mechanical mobilized side shear stresses and displacements under different toe stiffness condition for energy pile in undrained soils are shown in Figures 4.24(a) through 4.24(d). It can be observed from Figures 4.24(a) and 4.24(b) that the mechanical axial stresses and strain decreases with an increase of a_b, and the influence of ab becomes insignificant when a_b is large. Figure 4.24(c) shows that the decrease of toe stiffness leads to an increase of thermo-mechanical mobilized side shear stresses along the energy pile, and the influence of ab also becomes

insignificant when ab is large. The clear discontinuities in this figure indicate that the null point moves upward with a decrease of toe stiffness. Figure 4.24(d) shows that the thermo-mechanical displacements increase with a decreases of initial toe stiffness.

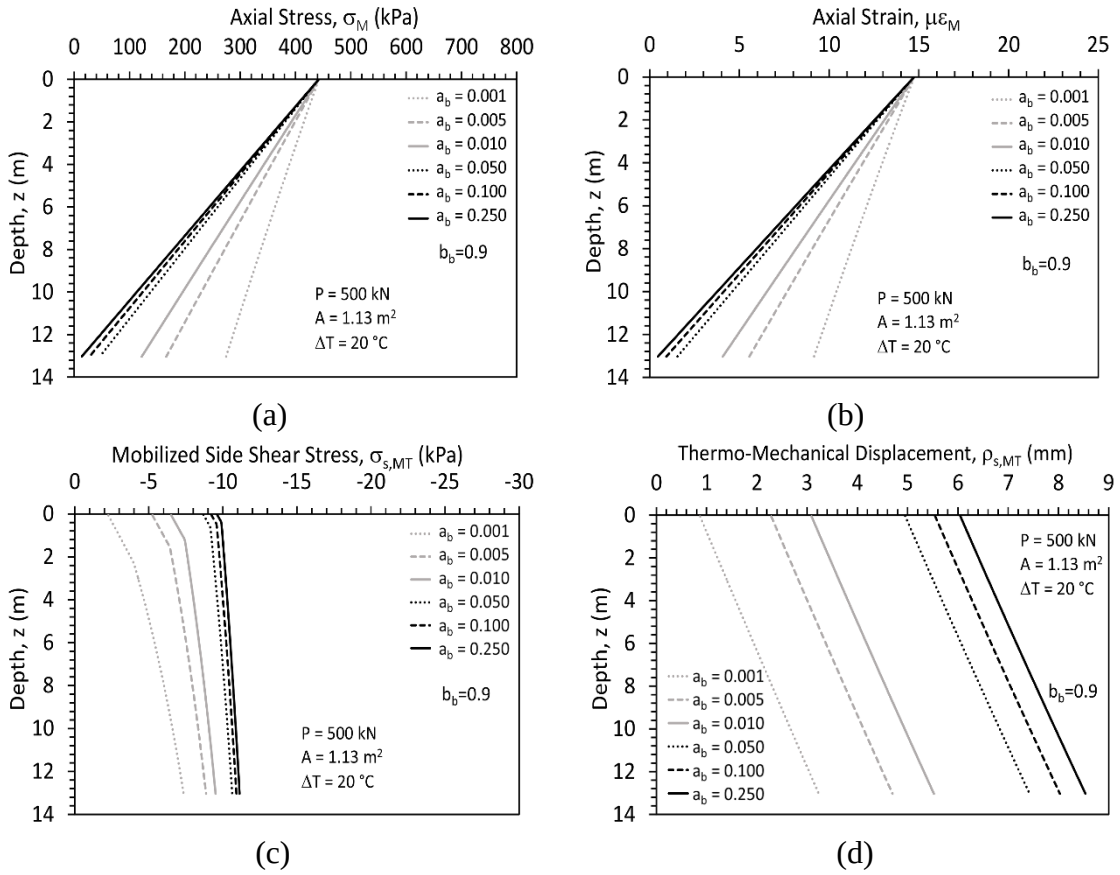

Figure 4.24: Soil-structure interaction behavior of a semi-floating energy pile in undrained soils: (a) Mechanical axial stresses; (b) Mechanical axial strains; (c) Mobilized side shear stresses; (d) Thermo-mechanical displacements

When comparing the results in Figures 4.21 and 4.22 with 4.23 and 4.24, it can be observed that the curves for undrained soil are more linear than those for drained soils, which has been discussed in former sections.

4.5.3 Synthesis of the Impact of the Toe Stiffness

Some maximum value of axial stress and displacement in terms of mechanical, thermal, and thermo-mechanical values are shown in Figures 4.25(a) and 4.25(b),

respectively. Figure 4.25(a) shows that greater values of a_b lead to a decrease in the maximum thermo-mechanical axial stress, but the influence of a_b on the maximum axial stress becomes less significant as a_b increases. This occurs because the initial stiffness of the mobilized base resistance Q-z curve decreases with increasing a_b, which leads to a softer base and allows more downward displacement (as proved in Figure 4.25(b)). When there is less base resistance force generated, the maximum axial stress decreases. Figure 4.25(b) shows that enlarging a_b leads to an increase in maximum displacement, and this effect is smaller when a_b is comparably large. This is because the toe is softer when a_b is larger, allowing longer part of pile expand downward from null. When a_b is very large, the energy pile can be seen as floating energy pile and total resistance is contributed by side-skin friction only, thus, a slight change in displacement will be observed.

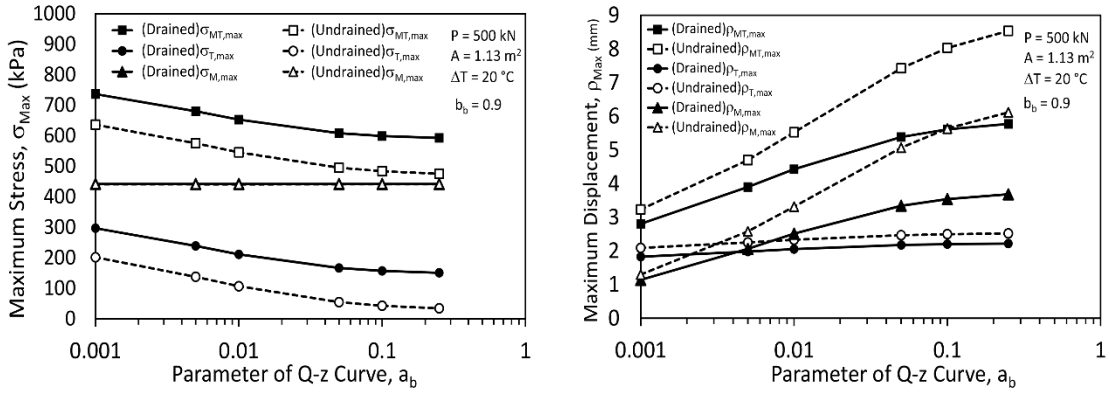

(a) (b)

Figure 4.25: Comparison of the impact of toe stiffness on soil-structure interaction behavior: (a) Max. stresses vs. a_b; (b) Max. displacement vs. a_b

4.6 Effect of Head Stiffness

A semi-floating energy pile with the same parameters is considered in this section. For each type of soil, a load of 500 kN was first applied to the pile head, then a change in temperature of 20 °C was applied uniformly to the length of the energy pile. The head

stiffness K_h of 0.01, 0.5, 1.0 or 10 MN/mm is used to determine the toe stiffness. The responses for this pile are shown in Figures 4.26 through 4.30.

4.6.1 Drained Soils

The thermo-mechanical, thermal induced axial stresses and strain under different head stiffness condition for energy piles in drained soils are shown in Figures 4.26(a) through 4.26(d). Figure 4.26(a) shows that the thermo-mechanical stress increases with an increases of heat stiffness, and this increase becomes less when K_h is larger. More significant change is observed at head rather than at base of the energy pile. When K_h is very low, the null point is comparably low, which leads to the longer part of pile moving upward so that the decrease of side shear stress causes a decrease of thermo-mechanical axial stresses. Figure 4.26(b) show that thermo-mechanical expansive strain decreases with an increases of heat stiffness, and this decrease becomes less when K_h is larger. Also, more significant change is observed at head rather than at base of the energy pile. For the case when K_h is very low, low axial strain was observed at two side of energy pile since the thermal expansion leads to longer part of pile above the null point unloading, which increases the thermo-mechanical expansion by reducing the resistant force from the side of pile. Figures 4.26(c) and 4.26(d) indicate that change of temperature induced axial stress in energy pile and axial strain with an increase of K_h, and the increase of K_h leads to null point moves downward. When K_h is large, the null point is very close to the head of the energy pile.

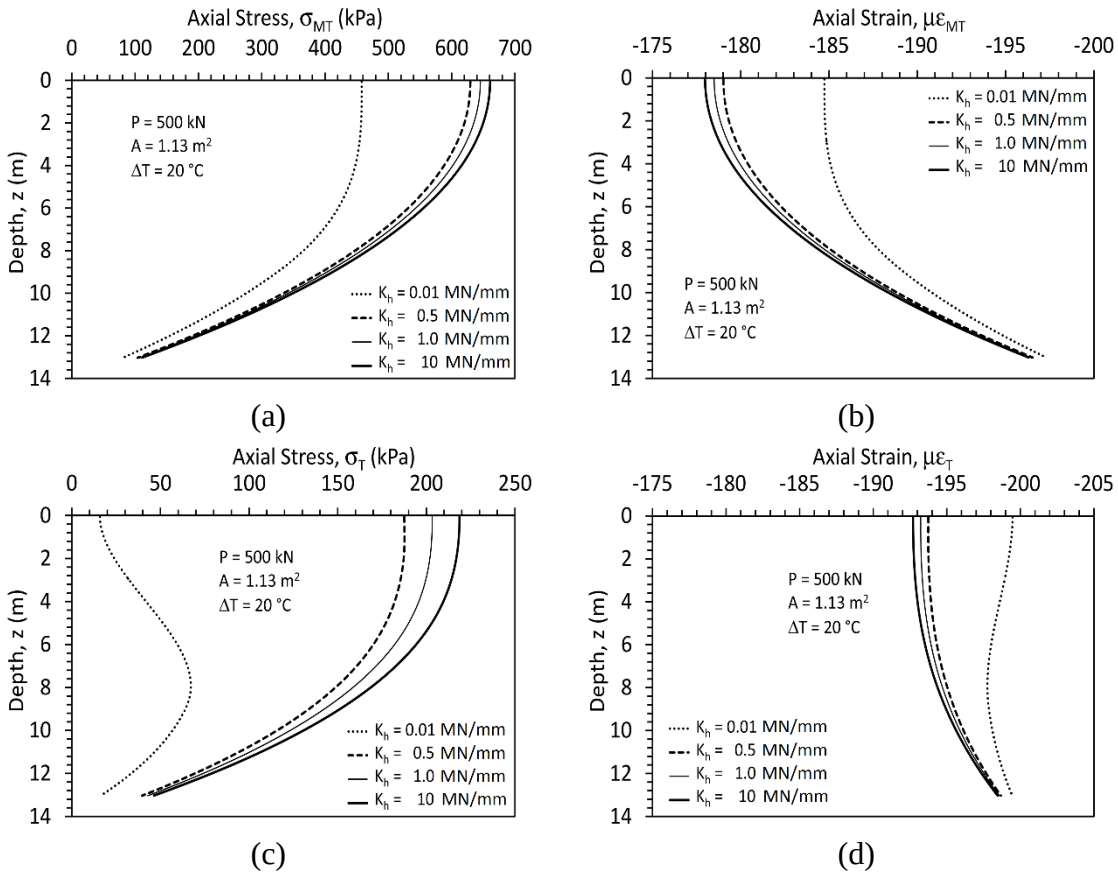

Figure 4.26: Soil-structure interaction behavior of a semi-floating energy pile in drained soils: (a) Thermo-mechanical axial stresses; (b) Thermo-mechanical axial strains; (c) Thermal axial stresses; (d) Thermal axial strains

The mechanical axial stresses and strain, thermo-mechanical mobilized side shear stresses and displacements strain under different head stiffness condition for energy pile in drained soils are shown in Figures 4.27(a) through 4.27(d). It can be observed from Figures 4.27(a) and 4.27(b) that a change of K_h has no influence on mechanical stresses and mechanical strains, because head stiffness is defined to constrain the top uplift induced by thermal loading. Figure 4.27(c) shows the mobilized side shear stress with head stiffness. It is clear that mobilized side shear stress increases with increase of K_h, and this increase becomes less as K_h become larger. The result from Figure 4.27(c) also indicates that the increase of K_h leads to the null point moving upward. Figure 4.27(d) shows the downward

displacement increases with an increase of head stiffness, because as the head becomes stiffer, the longer part of heated pile tends to move downward, which causes larger displacements to occur.

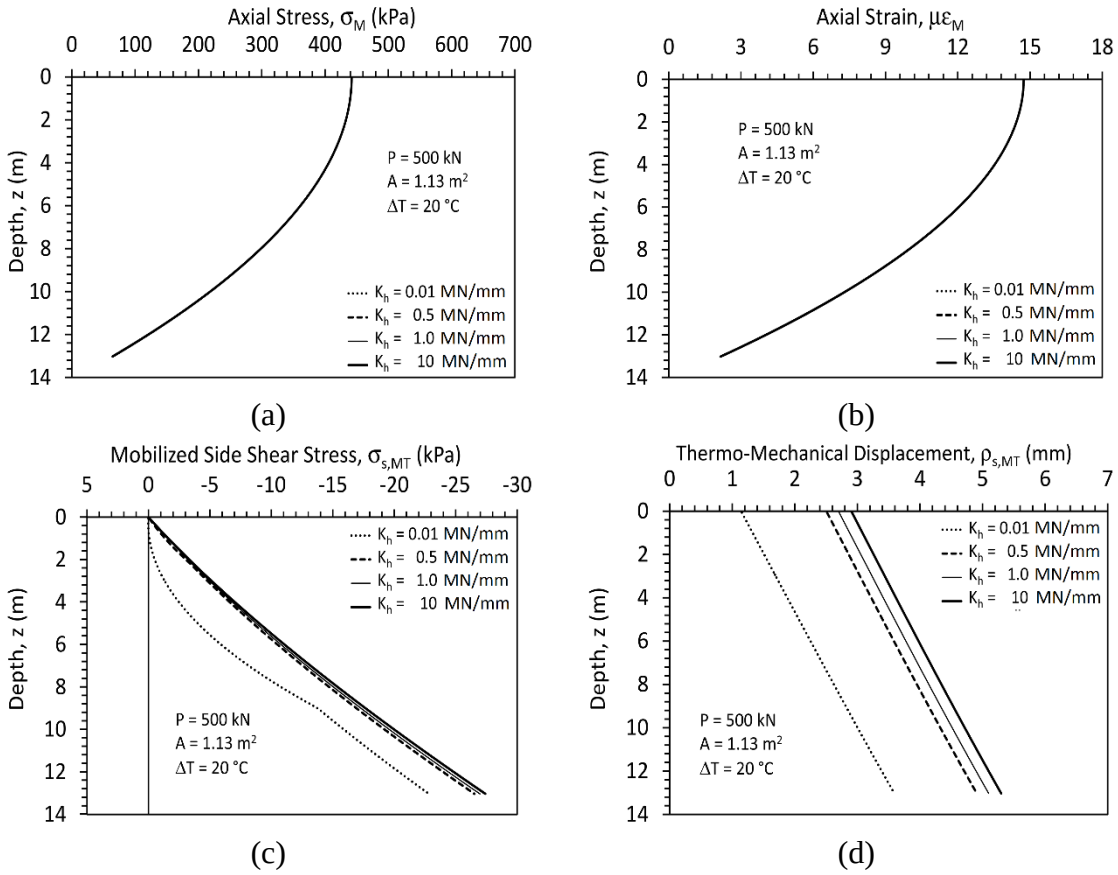

Figure 4.27: Soil-structure interaction behavior of a semi-floating energy pile in drained soils: (a) Mechanical axial stresses; (b) Mechanical axial strains (c) Mobilized side shear stresses; (d) Thermo-mechanical displacements

4.6.2 Undrained Soils

The thermo-mechanical, thermal induced axial stresses and strain under different head stiffness condition for energy pile in undrained soils are shown in Figures 4.28(a) through 4.28(d). It can be observed from Figures 4.28(a) and 4.28(c) that the thermo-mechanical and thermal induced axial stresses increase with an increase of K_h. Figures 4.28(b) and 4.28(d) show that the thermo-mechanical and thermal induced axial expansion

decreases with an increase of K_h. Also, the influences of K_h on the thermo-mechanical and thermal induced axial stresses and strains are insignificant when K_h is large, as explained in the previous section.

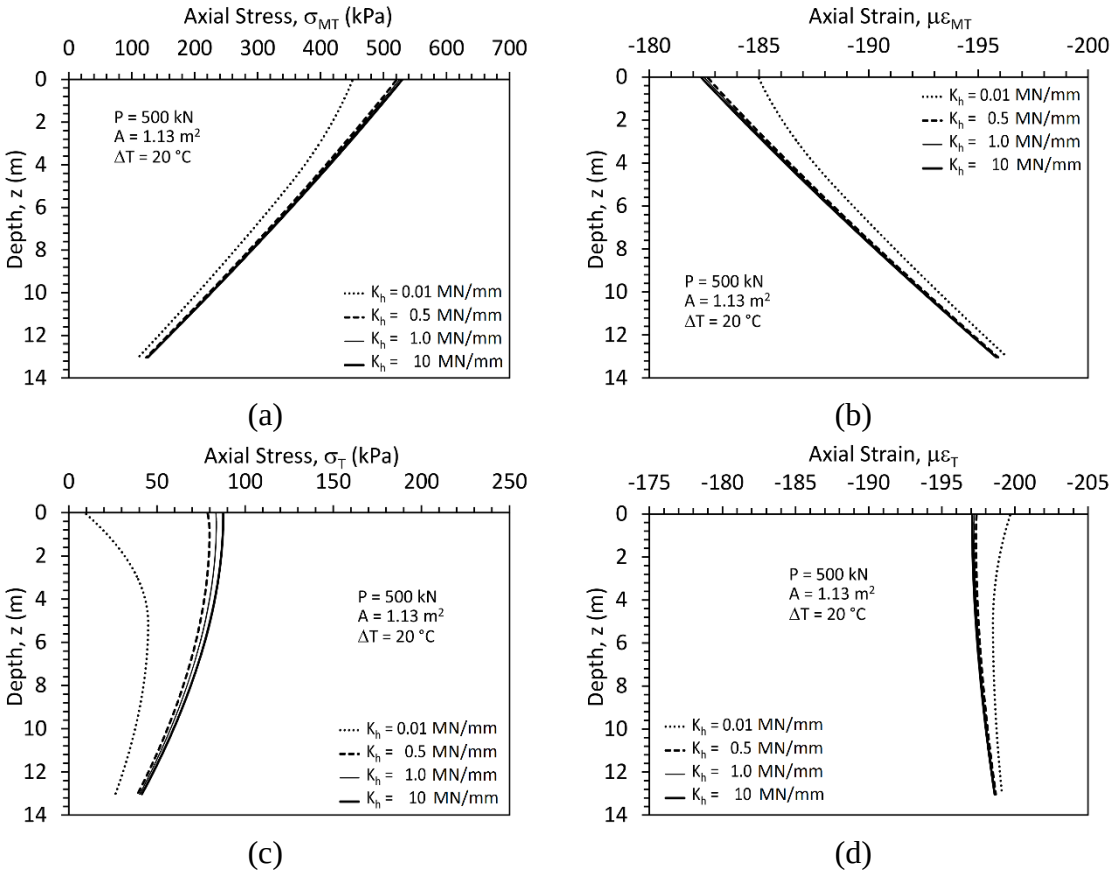

Figure 4.28: Soil-structure interaction behavior of a semi-floating energy pile in undrained soils: (a) Thermo-mechanical axial stresses; (b) Thermo-mechanical axial strains; (c) Thermal axial stresses; (d) Thermal axial strains

The mechanical axial stresses and strain, thermo-mechanical mobilized side shear stresses and displacements strain under different head stiffness condition for energy pile in undrained soils are shown in Figures 4.29(a) through 4.29(d). Figure 4.29(a) also shows that a change of K_h has no influence on mechanical stresses and mechanical strains, as explained in above section. Figure 4.29(c) shows the influence of head stiffness on thermo-mechanical mobilized side shear stresses. It can be observed from Figure 4.29(c) that an

increase of K_h leads to increases of thermo-mechanical mobilized side shear stresses, because more restraint is applied at the head of energy pile, leaving increases length of part of energy pile expands downward under thermal loading, which leads to an increase of mobilized side shear stresses. The clear discontinuities lying in this figure indicate that the null point moves upward with an increase of K_h. Figure 4.29(d) shows that the thermo-mechanical displacements increase with an increase of K_h, as explained above.

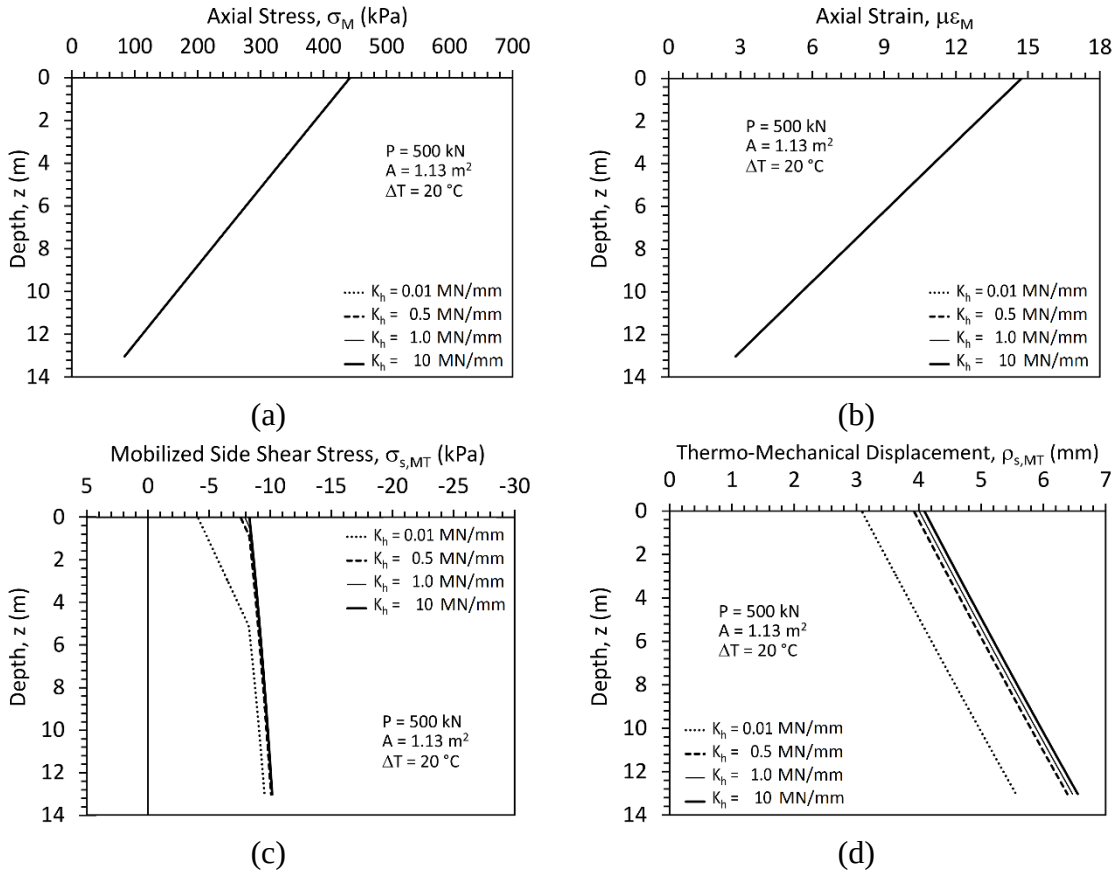

Figure 4.29: Soil-structure interaction behavior of a semi-floating energy pile in undrained soils: (a) Mechanical axial stresses; (b) Mechanical axial strains; (c) Mobilized side shear stresses; (d) Thermo-mechanical displacements

Comparing the behavior of energy piles in drained and undrained soils, it is clear from the Figures 4.26 and 4.28, a greater decrease of thermo-mechanical and thermal induced axial stress is observed in pile of deeper part because in the case of energy pile in

drained soil because the ultimate side shear stress is defined to be proportional to vertical earth pressure, yet the ultimate side shear stress in undrained soil is constant with depth when the displacement remains the same.

4.6.3 Synthesis of the Impact of Head Stiffness

Some maximum values of axial stress and displacement in terms of mechanical, thermal, and thermo-mechanical axial are shown in Figures 4.30(a) and 4.30(b), respectively. Figures 4.30(a) and 4.30(b) show the influence of head stiffness, K_h on maximum thermo-mechanical stresses and maximum displacement. It is observed from these figures that the maximum thermo-mechanical stresses and maximum displacements increase with an increase of head stiffness, and the influence of K_h on thermo-mechanical stresses and maximum displacements become less significant when K_h is comparably large. This is because with an increase of K_h, the head resistant stress increases and more side shear stress and toe resistant stress will be generated in order to achieve equilibrium, which leads to an increases in axial stresses. As the head resistance stress increases, the null point moves upward and larger part of energy pile experience an expansion downward, which leads to an increase of maximum displacements, though slightly larger axial stresses on the top lowers the maximum displacement by slightly lowering the thermal expansion considering the Young's modulus is very large. When K_h is very large, even if K_h increases, the upward movement of the null point is very low. In this case the maximum displacement accumulated from axial elongation of each element increases slightly even though a slight axial strain is induced by the slight increase of axial stress.

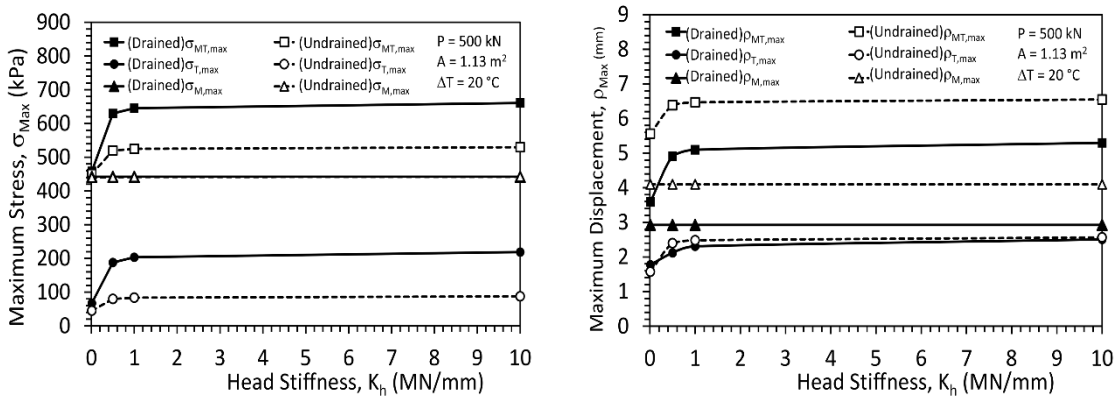

(a) (b)

Figure 4.30: Comparison of the impact of head stiffness on soil-structure interaction behavior: (a) Max. stresses vs. K_h; (b) Max. displacement vs. K_h

4.7 Effect of Side Shear Stress-Displacement Curve

A semi-floating energy pile with the same parameters is considered in this section. For each type of soil, a load of 500 kN was first applied to the pile head, then a change in temperature of 20 °C was applied uniformly to the length of the energy pile. Parameters a_s of 0.001, 0.0015, 0.002, 0.03, 0.004 or 0.005 and b_s of 0.9 are used to determine the toe stiffness. The response for this pile are shown in Figures 4.31 through 4.35.

4.7.1 Drained Soils

The thermo-mechanical, thermal induced axial stresses and strains under different side shear stress-displacement relation for energy pile in drained soils are shown in Figures 4.31(a) through 4.31(d). Figure 4.31(a) shows that above a certain point the thermo-mechanical stress increases with a decreases of parameter a_s, and below this point, the thermo-mechanical stress decreases with a decreases of parameter a_s. Figure 4.31(b) shows that above this certain point the thermo-mechanical expansive strain increases with a decreases of parameter a_s, and below this point, the thermo-mechanical expansive strain decreases with a decreases of parameter a_s, because an increase of a_s leading to a decreases

of the initial stiffness stress-displacement curve, lowers the side shear stress to restrain the thermal expansive strains. Figures 4.31(c) and 4.31(d) show that for larger values of the parameter a_s, the temperature changes induce lower axial compressive stress and larger axial expansive strain at the null point, and the axial compressive stress decreases and expansive strain increases as the pile element away from the null point. Parameter a_s has only a minor influence on the thermal axial stress at the toe.

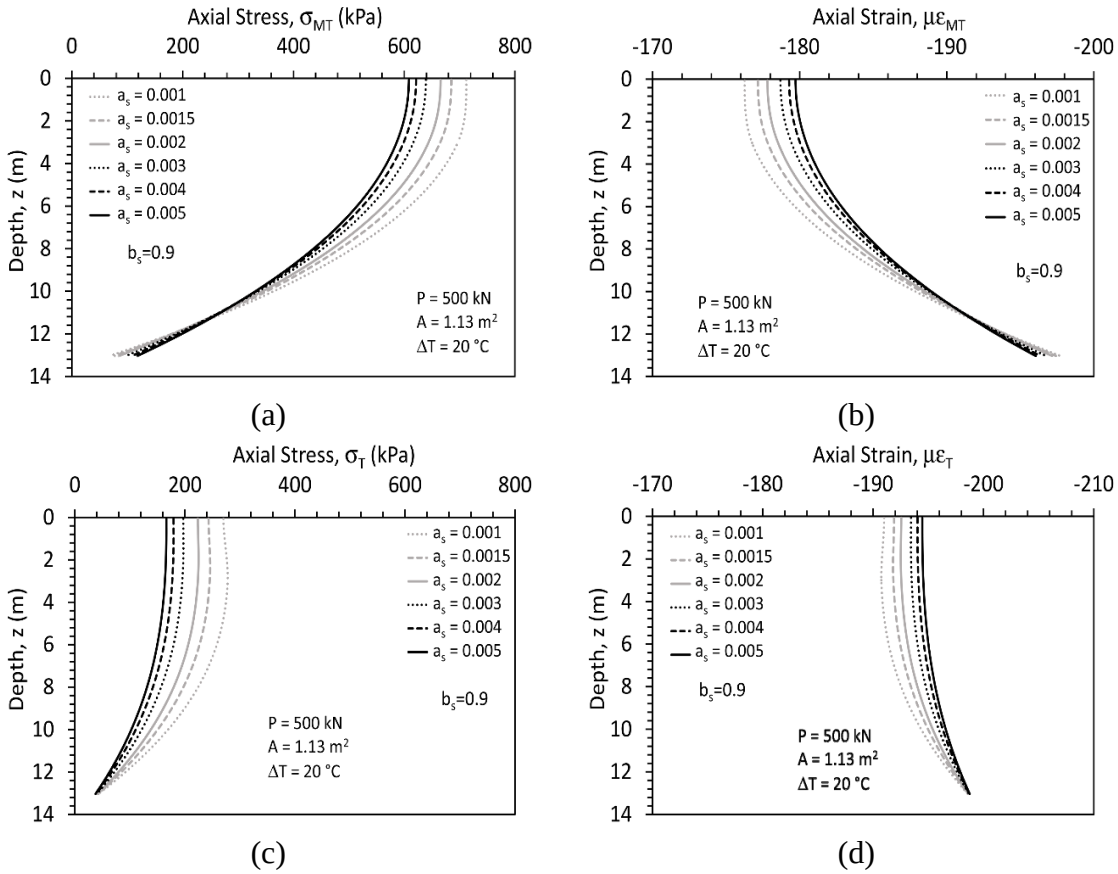

Figure 4.31: Soil-structure interaction behavior of a semi-floating energy pile in drained soils: (a) Thermo-mechanical axial stresses; (b) Thermo-mechanical axial strains; (c) Thermal axial stresses; (d) Thermal axial strains

The mechanical axial stresses and strain, thermo-mechanical mobilized side shear stresses and displacements strain under different side shear stress-displacement relation for energy pile in drained soils are shown in Figures 4.32(a) through 4.32(d). Figures 4.32(a)

and 4.32(b) show that an increase of the parameter a_s lead to greater increases in the mechanical axial stress and strain at deeper elements of pile than at shallower elements, and it has a slight influence on the mechanical axial stress and strain at the head of pile. Figure 4.32(c) indicates that parameter as increases with a decreases of mobilized side shear stress at toe of pile. Figure 4.32(d) shows that displacement becomes larger with an increase of parameter a_s.

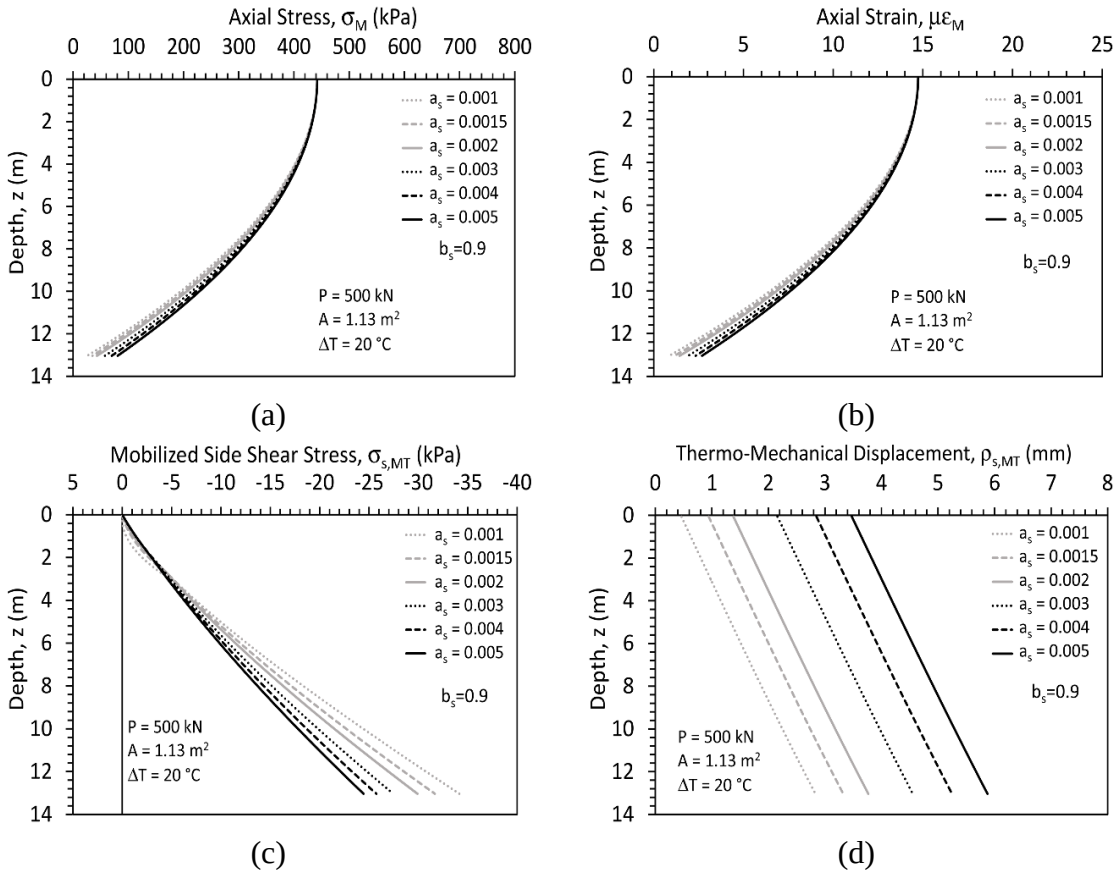

Figure 4.32: Soil-structure interaction behavior of a semi-floating energy pile in drained soils: (a) Mechanical axial stresses; (b) Mechanical axial strains; (c) Mobilized side shear stresses; (d) Thermo-mechanical displacements

4.7.2 Undrained Soils

The thermo-mechanical, thermal induced axial stresses and strains under different side shear stress-displacement relation for energy pile in undrained soils are shown in

Figures 4.33(a) through 4.33(d). Figure 4.33(a) also shows that the increase of a_s leads to decreases in the thermo-mechanical axial stresses above a certain point and increases below a certain point. Figure 4.33(b) indicates that the increase of a_s leads to the thermo-mechanical axial strains increase above certain point and decrease below the same point. Figures 4.33(c) and 4.33(d) show that the thermally-induced axial stresses decreases and thermal induced axial strains increase with an increase of a_s.

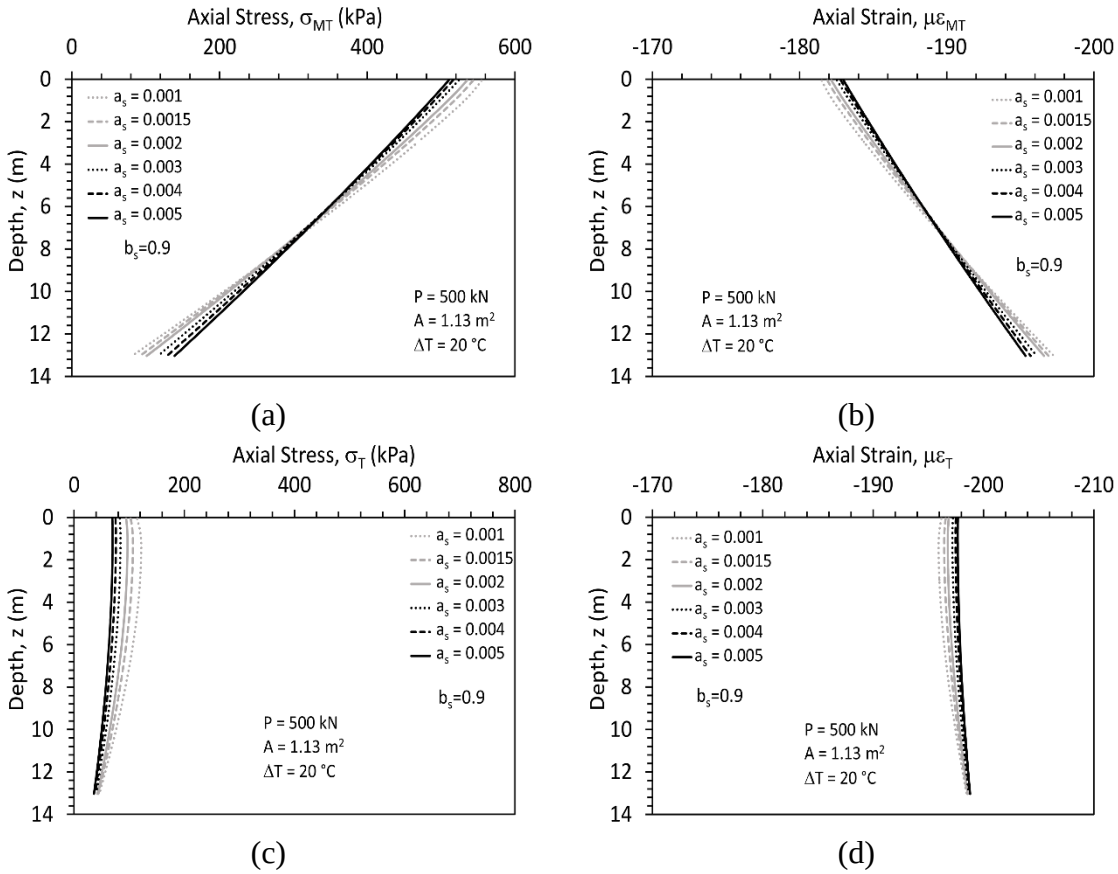

Figure 4.33: Soil-structure interaction behavior of a semi-floating energy pile in undrained soils: (a) Thermo-mechanical axial stresses; (b) Thermo-mechanical axial strains; (c) Thermal axial stresses; (d) Thermal axial strains

The mechanical axial stresses and strain, thermo-mechanical mobilized side shear stresses and displacements strain under different side shear stress-displacement relation for energy pile in undrained soils are shown in Figures 4.34(a) through 4.34(d). Figures 4.34(a)

and 4.34(b) indicate that the initial stiffness of the T-z curve has no influence on mechanical axial stresses and strain at the head of energy pile. The mechanical stresses and strains decrease with an increase of a_s, because the stiffness of T-z curve decreases as a_s increases, leaving lower side-skin friction to restrain the pile. Figure 4.34(c) shows that the a_s have insignificant influence on the null point location. The decrease of initial stiffness of T-z curve leads to thermo-mechanical mobilized side shear stresses decreases below certain point and increases above this point. Figure 4.34(d) indicates that the increase of a_s leads to a uniform increase of thermo-mechanical displacement along the energy pile.

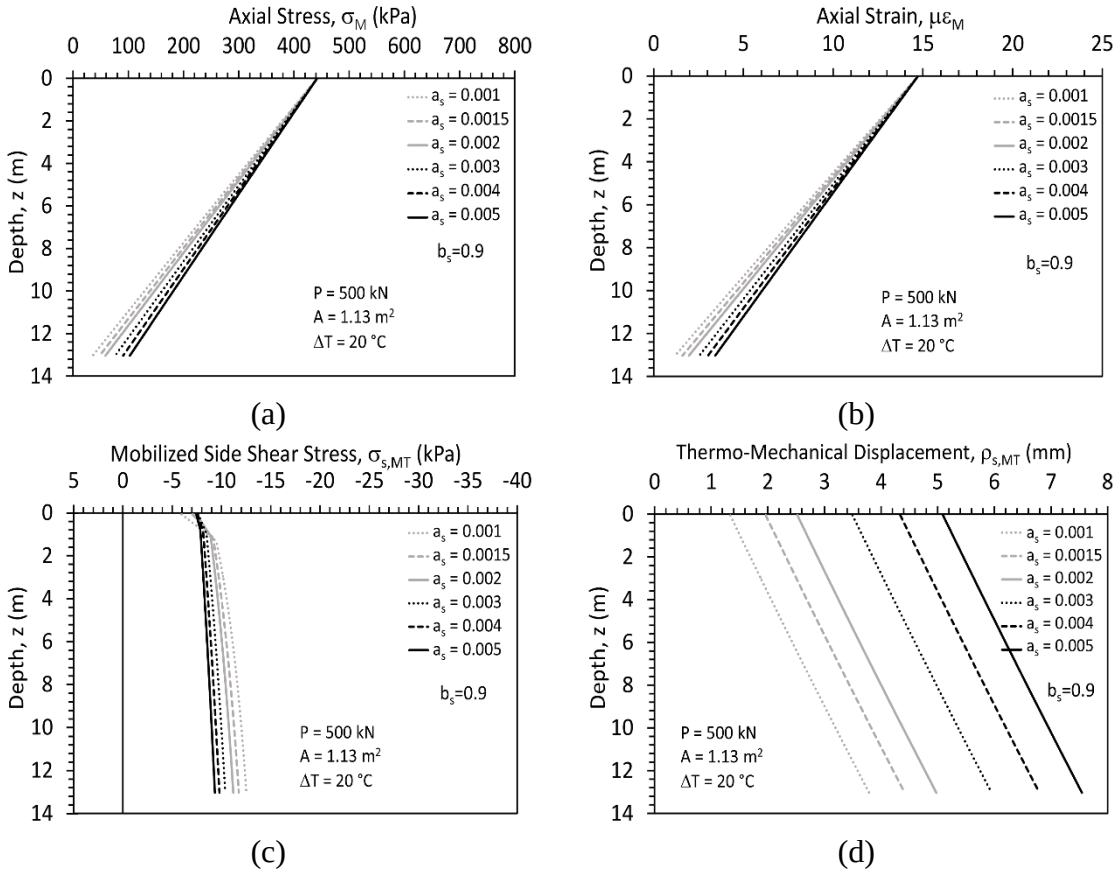

Figure 4.34: Soil-structure interaction behavior of a semi-floating energy pile in undrained soils: (a) Mechanical axial stresses; (b) Mechanical axial strains; (c) Mobilized side shear stresses; (d) Thermo-mechanical displacements

Comparing the behavior of energy piles in drained and undrained soils, it is clear from Figures 4.30 through 4.33 that the curve for the thermal axial stresses and strains are more linear with depth for energy piles in undrained soils than pile in drained soils. Larger axial stresses and lower axial strains are observed in the case of pile in friction soils rather than in undrained soils. The mobilized side shear stress at base varies larger with a change of parameter a_s for the case with drained soils rather than with undrained soils.

4.7.3 Synthesis of the Impact of Side Shear Stress-Displacement Curve

Some maximum value of axial stress and displacement in terms of mechanical, thermal, and thermo-mechanical axial are picked up and are shown in Figures 4.35(a) and 4.35(b), respectively. Figure 4.35(a) illustrates the maximum axial stresses vary with parameter a_s. It is clear from this figure that the maximum thermo-mechanical axial stress decreases with an increase of parameter a_s, and the ratio of the decrease is approximately linear with logarithm of parameter a_s. As parameter a_s increases, the difference of maximum stresses in the case of pile in two types of soil decreases. Maximum thermo-mechanical stresses are larger for energy pile in drained soils than in undrained soils. Figure 4.35(b) illustrates the maximum displacement varies with parameter a_s. From this figure, larger maximum displacement is observed to increase with parameter a_s, and the maximum displacement for energy pile in drained soils is approximate 1 mm larger and increases a little more than in undrained soils.

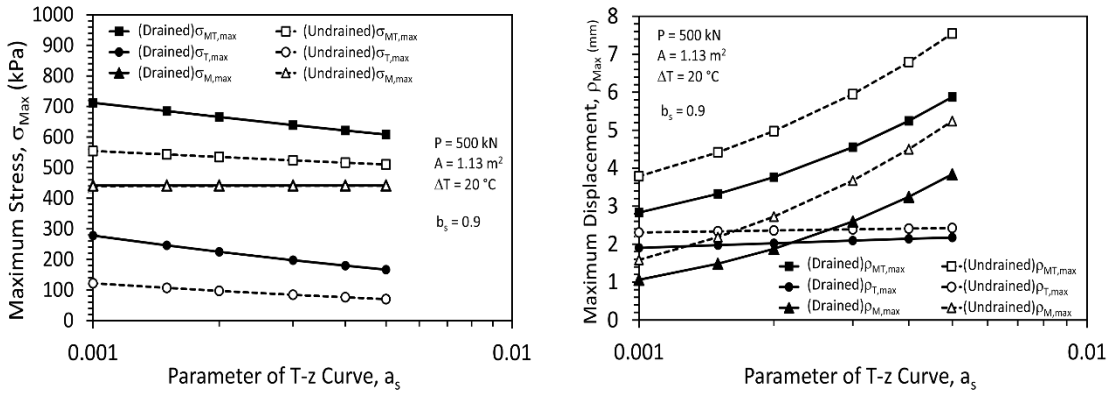

(a) (b)

Figure 4.35: Comparison of the impact of T-z Curve on soil-structure interaction: (a) Max. stresses vs. a_s; (b) Max. displacement vs. a_s

4.8 Effect of Radial Expansion

A semi-floating energy pile with the same parameters is considered in this section. For each type of soil, a load of 500 kN was first applied to the pile head, then a change in temperature of 20 °C was applied uniformly to the length of the energy pile. The radial expansion parameter of 0, 20, 40 or 60 is used to determine the toe stiffness. The responses of this pile are shown in Figures 4.36 through 4.40.

4.8.1 Drained Soils

The thermo-mechanical and thermal induced axial stresses and strains under different radial expansion parameter for energy pile in drained soils are shown in Figures 4.36(a) through 4.36(d). It can be observed from Figure 4.36(a) that the thermo-mechanical stress linearly increases with an increase of radial expansion, and thermo-mechanical stress decreases with depth. Radial expansion does have slight influence on the thermo-mechanical stress at toe. Figure 4.36(b) shows that the thermo-mechanical expansive strain linearly decreases with an increase of radial expansion. Maximum thermo-mechanical axial expansion is observed at head of pile and the strain decreases with depth from head to the

toe of pile. In Figures 4.36(c) and 4.36(d), larger thermal axial compressive stresses and lower expansive strains are observed with an increase of radial expansion. This is because ultimate side-skin resistance increases with an increase if radial expansion κ. As side shear resistance increases the thermo-mechanical and thermal induced axial stresses increase, larger friction restrains the energy pile to expand under thermal loading.

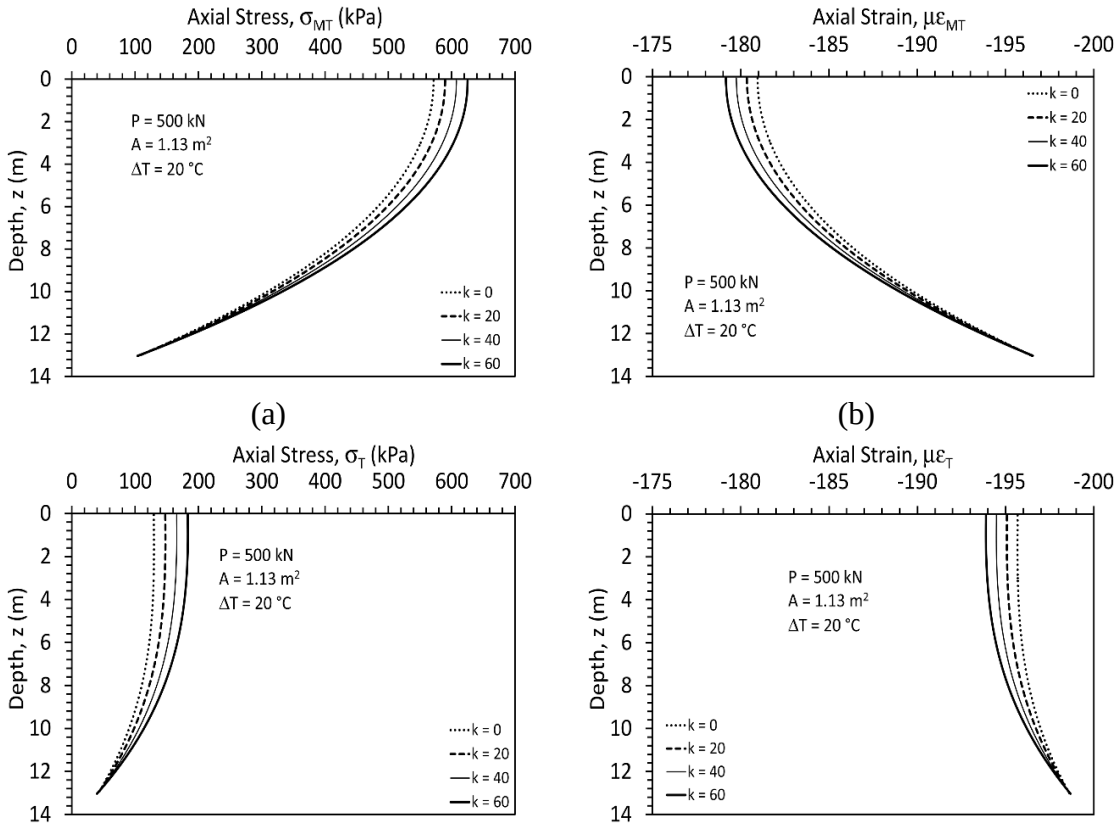

Figure 4.36: Soil-structure interaction behavior of a semi-floating energy pile in drained soils: (a) Thermo-mechanical axial stresses; (b) Thermo-mechanical axial strains; (c) Thermal axial stresses; (d) Thermal axial strains;

The mechanical axial stresses and strains, thermo-mechanical mobilized side shear stresses and displacements under different radial expansion parameter for energy pile in drained soils are shown in Figures 4.37(a) through 4.37(d). It is clear from Figures 4.37(a) and 4.37(b) that radial expansion has only a minor influence on the mechanical stresses

and strains in the pile. Figure 4.37(c) shows that mobilized side shear stress increases with an increases of radial expansion, because the increase of radial expansion parameter κ lead to an increase of reduction factor, which eventually increases the ultimate side shear stress. Figure 4.37(d) indicates that the thermo-mechanical displacement linearly decreases with a slight increase of radial expansion parameter.

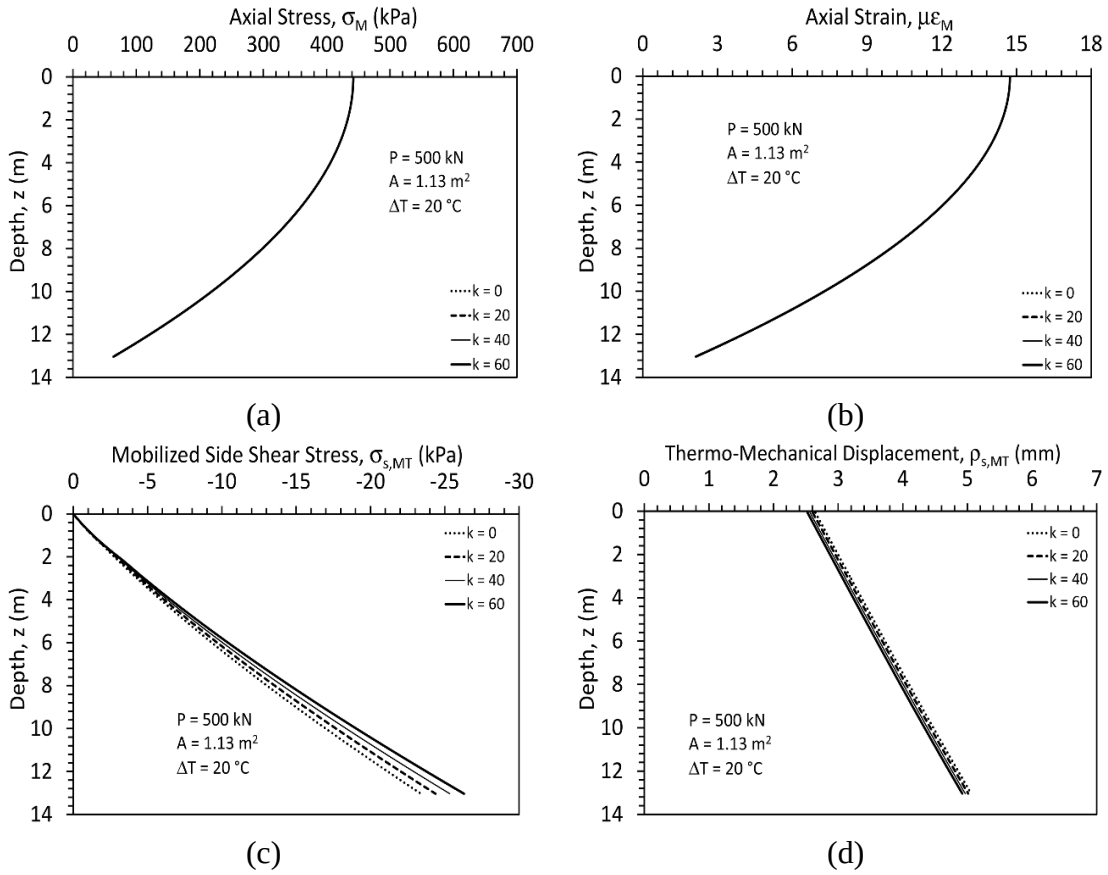

Figure 4.37: Soil-structure interaction behavior of a semi-floating energy pile in drained soils: (a) Mechanical axial stresses; (b) Mechanical axial strains; (c) Mobilized side shear stresses; (d) Thermo-mechanical displacements

4.8.2 Undrained Soils

The thermo-mechanical and thermal induced axial stresses and strains under different radial expansion parameter for energy pile in undrained soils are shown in Figures 4.38(a) through 4.38(d). It can be observed from Figures 4.38(a) and 4.38(d) that the radial

expansion has no influence on the thermo-mechanical and thermal induced axial stresses and strain.

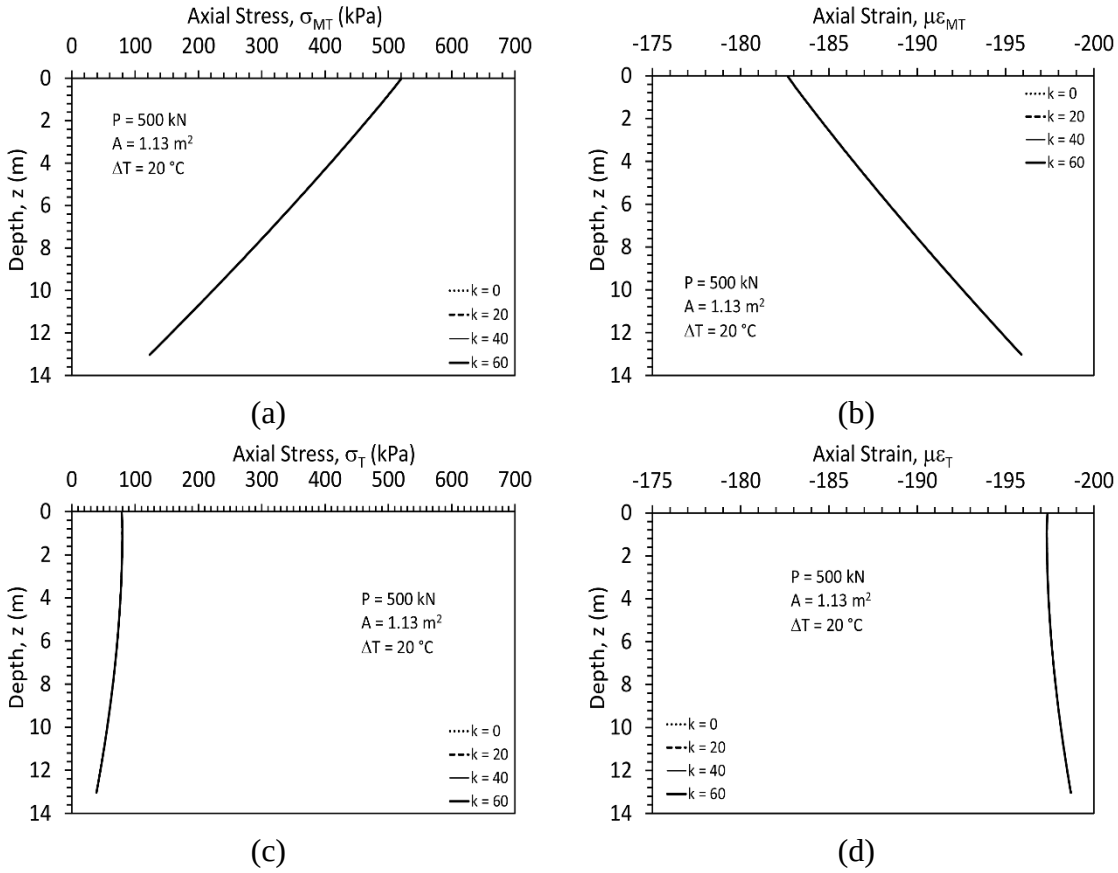

Figure 4.38: Soil-structure interaction behavior of a semi-floating energy pile in undrained soils: (a) Thermo-mechanical axial Stresses; (b) Thermo-mechanical axial strains; (c) Thermal axial stresses; (d) Thermal axial strains

The mechanical axial stresses and strains, thermo-mechanical mobilized side shear stresses and displacements under different radial expansion parameter for energy pile in undrained soils are shown in Figures 4.39(a) through 4.39(d). Figures 4.39(a) through 4.39(d) also indicate that radial expansion has no influence on mechanical stresses and strains, thermo-mechanical mobilized side shear stresses and displacements.

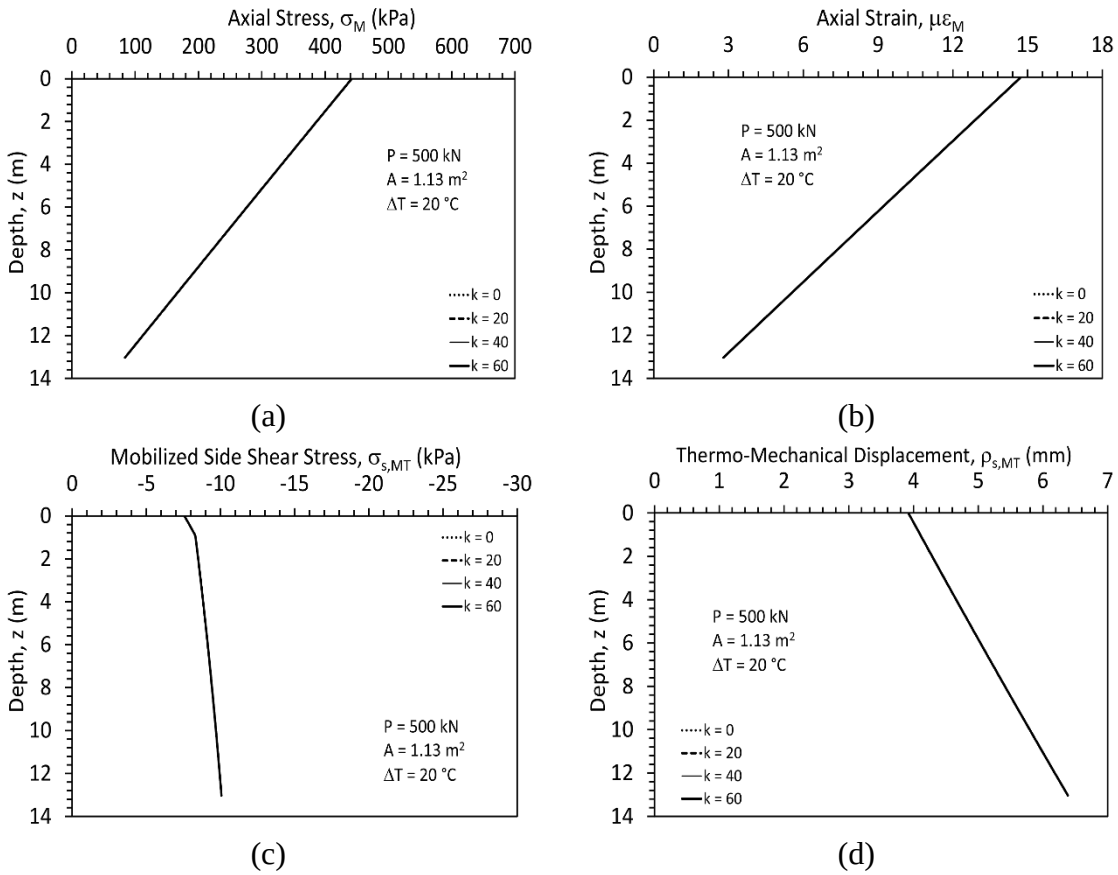

Figure 4.39: Soil-structure interaction behavior of a semi-floating energy pile in undrained soils: (a) Mechanical axial stresses; (b) Mechanical axial strains; (c) Mobilized side shear stresses; (d) Thermo-mechanical displacements

4.8.3 Synthesis of the Role of Radial Expansion

Some maximum value of axial stress and displacement in terms of mechanical, thermal, and thermo-mechanical axial are picked up and are shown in Figures 4.40(a) and 4.40(b), respectively. The results in these figures indicate that radial expansion does play a small role in the maximum stress in undrained soils, but the effect is not significant. The maximum axial stresses vary linearly with radial expansion parameter κ, as shown in Figure 4.40(a). It is clear from this figure that the maximum thermo-mechanical stresses increase with radial expansion parameter κ. The maximum displacement varies with radial

expansion parameter κ, as shown in Figure 4.40(b). It can be observed from Figure 4.40(b) that radial expansion has a negligible influence on maximum displacement.

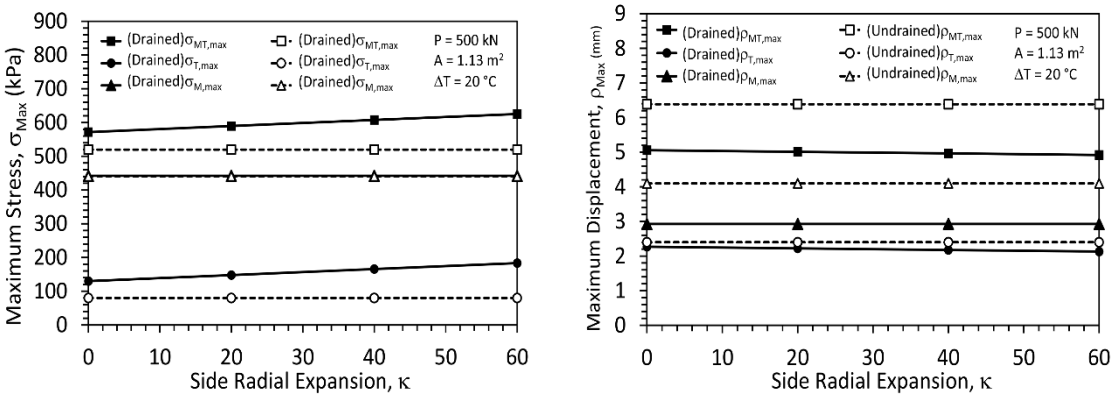

(a) (b)

Figure 4.40: Comparison of the impact of radial expansion on soil-structure interaction: (a) Max. stresses vs. κ; (b) Max. displacement vs. κ

CHAPTER 5: EVALUATION OF FIELD DATA

5.1 Overview

The updated load-transfer model was calibrated to evaluate the expected soil-structure interaction response of four case studies, including one field study (Murphy et al. 2015) and three centrifuge studies (Stewart and McCartney 2013; Goode and McCartney 2015; Ng et al. 2014). The calibration of the model to these studies permits evaluation of the typical ranges of values of the different model parameters that are difficult to measure in the field, including the parameters of the T-z and Q-z curves and the head stiffness K_h. All of these studies involve soils with a drained response, as clay soils may have other thermo-mechanical responses that are not considered using the load-transfer model developed in this study

5.2 Calibration to the Data of Murphy et al. (2015)

A one-story, shower-shave building was constructed at the US Air Force Academy (USAFA) beginning in March 2012. A site investigation was performed in September 2011, which consisted of two 102-mm-diameter borings located within the building footprint, extending 12 and 7 m below the ground surface. At selected intervals, disturbed samples were obtained by driving split-spoon with a 622.75 N hammer falling 762 mm. Penetration resistance measurements were made during driving. Exploration results from both boreholes were similar and showed three prominent strata, and relevant data are shown in Table 5.1.

Table 5.1: Summary of stratigraphy during subsurface exploration at USAFA

Layer	Depth to bottom of stratum (m)	Material encountered	Water content (%)	Dry unit weight (kN/m^3)	SPT N-Value
1	1	Sandy fill w/silt, gravel	5	18.4	70
2	2	Dense sands, silt, gravel	7	19.2	185
3	12+	Sandstone	N/A	N/A	50/25.4

Eight drilled shafts, each 15.2 m deep by 0.61 m diameter, provide the foundation support for the structure, as shown in Figure 5.1. Each shaft has one, two, or three heat exchanger loops configured in different ways (Figure 5.1). Foundations 1 through 4 have identical heat exchanger configurations, with two continuous heat exchanger loops attached to the inside of the steel reinforcement cage. Construction of the floor slab, walls, and roof occurred in Fall 2012. After the building was constructed, a series of thermal response tests were performed on individual and groups of energy piles. To evaluate the thermo-mechanical response of the energy piles, a nominal heat input of 11 kW for 498 hours was applied to heating Foundations 1-4 simultaneously to avoid heating any energy pile component too rapidly and to allow sufficient time to increase the temperature of the soil surrounding the energy piles. The resonant frequency values were recorded from Geokon Model 4200 vibrating wire strain gauge, and then converted to thermal axial strains with coefficient of thermal expansion of -12με/°C. Profiles of thermal axial stress were calculated with Young's modulus of 30 GPa. Profiles of thermal axial displacement were calculated by integrating the thermal axial strain profiles from toe of piles.

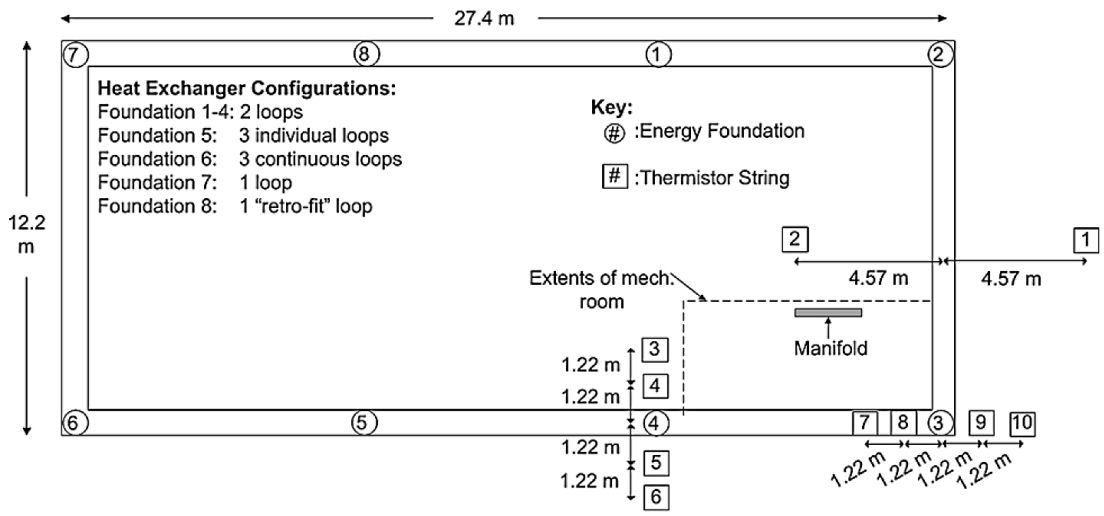

Figure 5.1 Plan view of the building with the locations of the different energy piles

The model parameters used to match the data from Murphy et al. (2015) are summarized as follows:

- Length L = 15.2 m
- Diameter D = 0.61 m
- Unit weight of pile γ_p = 24 kN/m^3
- Young's modulus of reinforced pile E = 30 GPa
- Coefficient of unrestrained thermal expansion $\alpha_T = 12\times10^{-6}$ m/m°C
- Empirical coefficient for radial expansion κ = 65
- Axial mechanical load P = 833 kN
- Changes of temperature ΔT = 6°C, 12°C, 19°C
- The values of head stiffness K_h that provided the best fit to the data are 800 MN/m for Foundations 1 and 4, and 300 MN/m for Foundation 3, as will be discussed later.

The subsurface stiff gravel and sandstone layers are assumed to be one equivalent layer with internal friction angle of 45° and dry unit weight of 19.2 kN/m^3. The undrained

shear strength at the toe $c_{u,b}$ is assumed to be 2000 kPa as toe of piles is embedded in sandstone. The fitting parameters that provided the best fit to the data were a_b = 0.002 and b_b = 0.9 for Q-z curve and a_s = 0.0003, b_s = 0.9, β = 0.9 for the T-z curve. The processed field data and simulation results are shown in Figures 5.2 and 5.3.

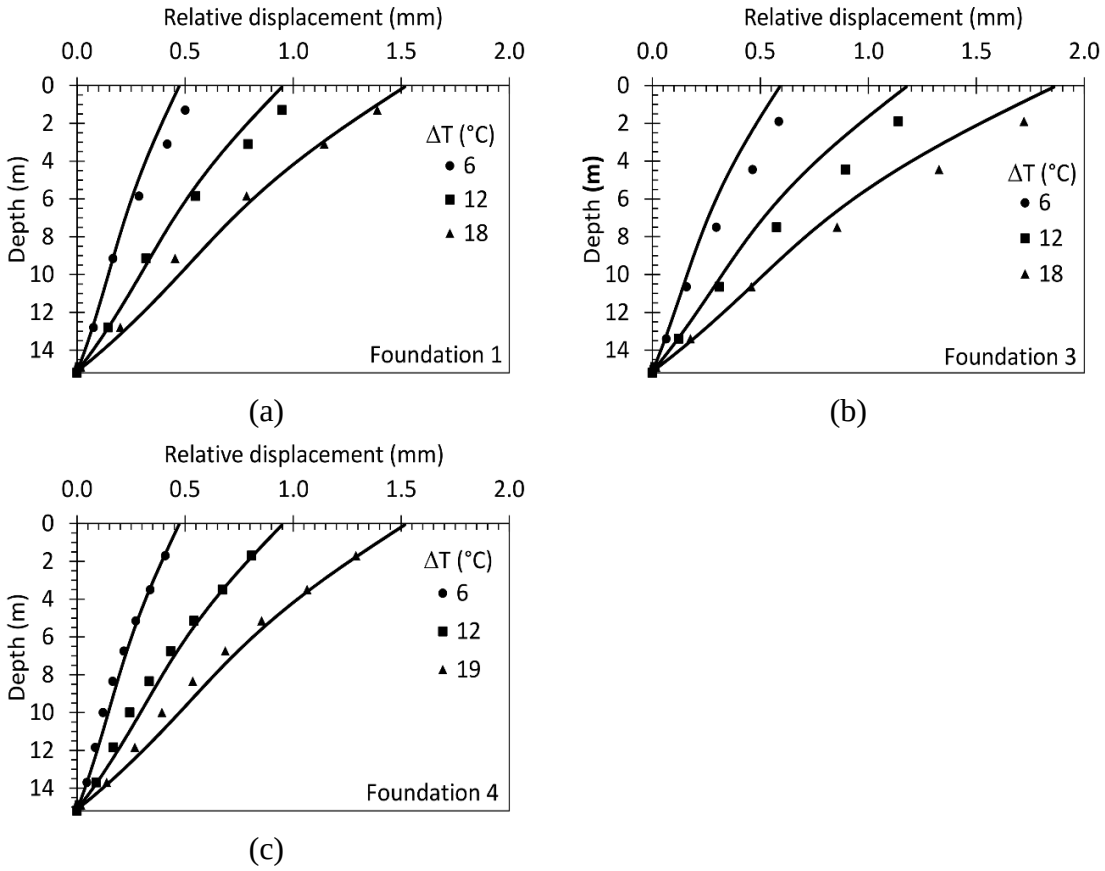

Figure 5.2: Predicted profiles of thermal axial displacement for three of the energy piles evaluated by Murphy et al. (2015)

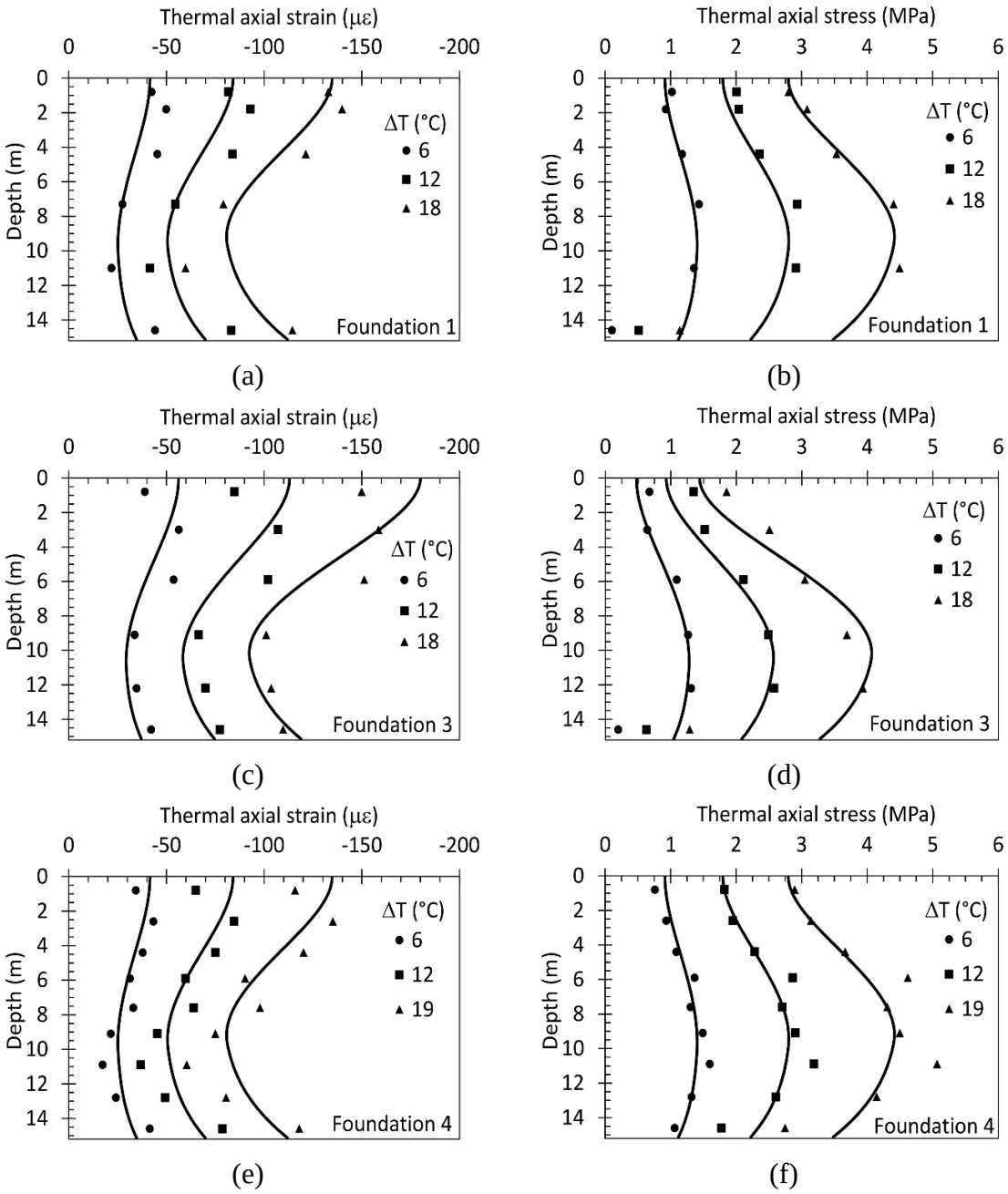

Figure 5.3: Predicted profiles of thermal axial strains and thermal axial stresses for three energy piles evaluated by Murphy et al. (2015)

The fitting results in these figures indicate a good estimate of behavior of energy pile in terms of axial compressive stresses and strains and displacements induced by the thermal loading in this research. The overall trend from the model is consistent with the

field data. However, the noticeable inconsistencies lie in the part in depth between 0 to 3 m as the model assuming a homogeneous layer of soil rather than 3 layers in project for simulation. Besides, the thermal axial stresses at the toe for three energy piles and the thermal axial stress at ΔT equal to 19°C are not well captured by numerical simulation.

5.3 Calibration using the Data of Goode and McCartney (2015)

A scale-model energy pile having a diameter of 63.5 mm and a length of 342.9 mm (short foundation) was heated in Bonny silt and Nevada sand, respectively, at a centrifuge g-level of 24 under an applied axial stress of 360 kPa. Under this centrifuge acceleration, the corresponding prototype-scale energy pile has a diameter of 1.5 m and a length of 8.2 m. Before centrifuge testing, a comprehensive set of characterization tests were performed on the precast energy pile outside of the soil in a load frame at 1-gravity to determine their mechanical and thermal properties. First, the energy pile was loading mechanically in stages in a load frame to evaluate the Young's modulus of the reinforced concrete, then heated under free-expansion conditions to evaluate the coefficient of linear thermal expansion.

The model parameters from Goode and McCartney (2015) are summarized as follows:

- Length L = 8.2 m
- Diameter D = 1.5 m
- Unit weight of pile γ_p = 24 kN/m^3
- Young's modulus of reinforced pile E = 33 GPa
- Coefficient of thermal expansion α_T = 16×10^{-6} m/m°C
- Head-structure stiffness K_h = 0

- Empirical coefficient for radial expansion $\kappa = 65$

The Nevada sand used in this study consists of uniform angular particles, and based on the characteristic grain size has a unified soil classification system (USCS) classification of SP (poorly graded sand). It has a relative density of 60%, and at this relative density and a mean stress of 100 kPa, it has a friction angle of 35°, a shear modulus of 30 MPa, and a Poisson's ratio of 0.3. The Bonny silt used in this study has a USCS classification of ML (inorganic silt). The soil layers were prepared by compacting silt having a gravimetric water content of 14.2% in 76.2-mmthick lifts around the foundation to reach a target dry density of 1,565 kg/m^3. Drained soil properties were assumed for the ultimate side shear resistance along the pile, while an undrained shear strength was assumed for the soil at the toe of the pile. The soil parameters are given as follows:

- Drained friction angle $\phi = 32.4°$ for Bonny silt and 35° for Nevada sand
- Dry unit weight of soil is 14.2 kN/m^3 for Bonny silt and 15 kN/m^3 for Nevada sand

The fitting parameters for the Q-z curve of $a_b = 0.002$ and $b_b = 0.9$ were used for Bonny silt in this analysis to represent the stiff end restraint at the tip of the energy pile, and $a_b = 0.001$ and $b_b = 0.9$ were used for Nevada sand. The parameters of the T-z that provided the best fit to the data were $a_s = 0.0001$, $b_s = 0.9$, $\beta = 2.0$ and $c_{u,b} = 54$ kPa for the energy pile in Bonny silt and $a_s = 0.0001$, $b_s = 0.9$, $\beta = 1.2$ and $c_{u,b} = 100$ kPa for the energy pile in Nevada sand. For the case of unsaturated Bonny silt, the suction-induced undrained shear strength c_u is assumed to be 20 kPa for the best fit.

The predicted thermal axial strain, thermal axial stress and thermal axial displacement profiles using load-transfer model analysis along with the centrifuge data for each temperature change condition are shown in Figures 5.4(a), 5.4(c) and 5.4(e) and in

Figures 5.4(b), 5.4(d) and 5.4(f) for the energy piles in Bonny silt and in Nevada sand, respectively.

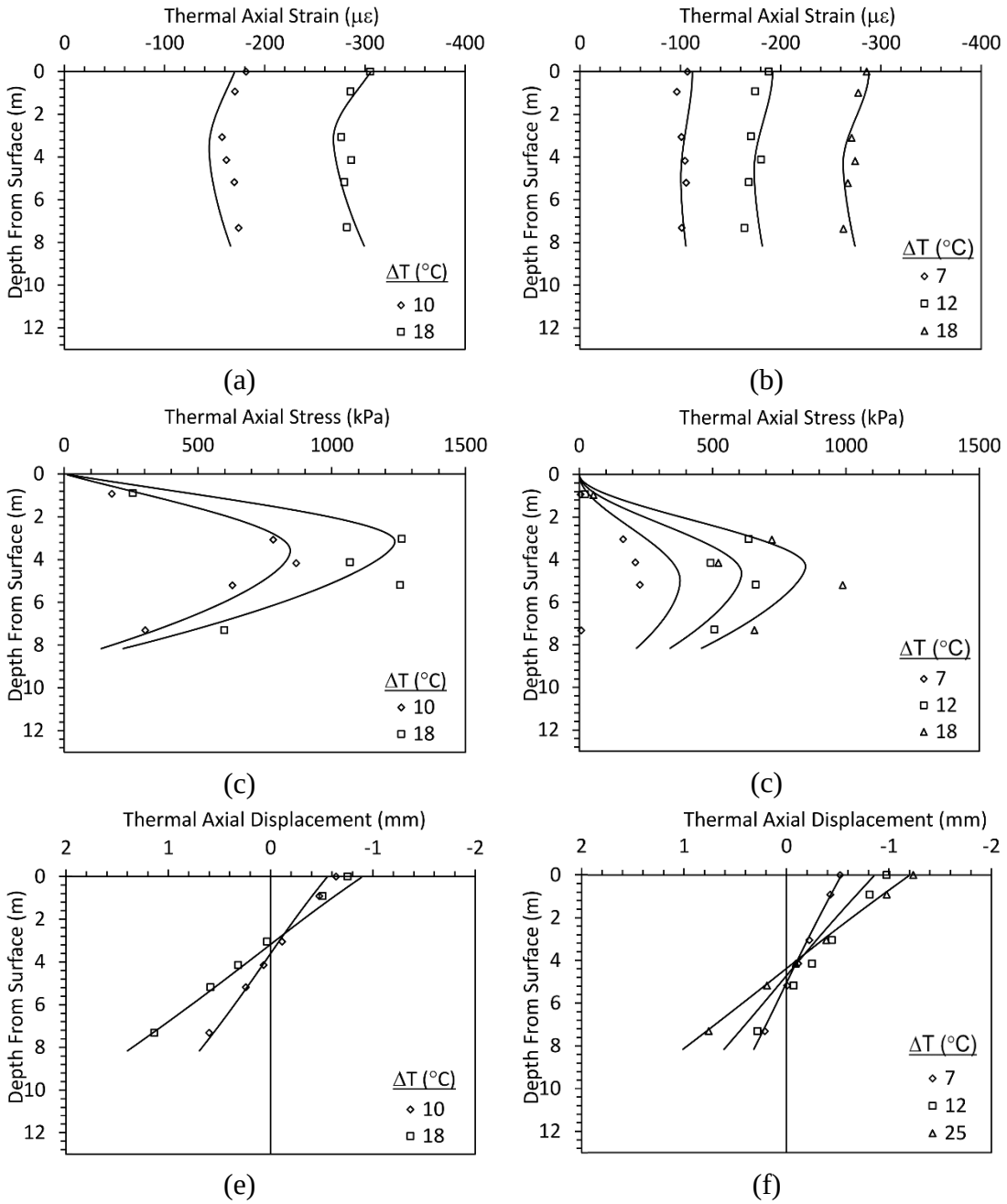

Figure 5.4: Predicted profiles of semi-floating energy pile with centrifuge model test by Goode and McCartney (2015): (a) Thermal axial strains (silt); (b) Thermal axial strains (sand); (c) Thermal axial displacements (silt); (d) Thermal axial displacements (sand); (e) Thermal axial stress (silt); (f) Thermal axial stress (sand)

Goode and McCartney (2015) plotted the thermal axial displacement values against the location at the midpoint between two strain gages. However, this should be plotted against the location of the upper gage. Accordingly, the experimental data from Goode and McCartney (2015) were re-analyzed so that the calculated thermal axial displacement values correspond to the location of the upper gage.

The results shown in these figures indicate a fairly good capture of the overall trend of axial stresses and strains induced by thermal loading in this case study. However, the difference between the applied average temperature applied in model and the actual temperature profile in real situation leads to an error in the thermal strain and stress.

5.4 Calibration using the Data of Stewart and McCartney (2014)

A small-scale, end-bearing model energy pile with dimensions of 50.8 mm in diameter and 533.4 mm in length was heated in the centrifuge at a g-level of 24.6 under an applied axial stress of 443 kPa. Under this centrifuge acceleration, the stresses and strains induced in the energy pile are representative of a prototype energy pile which has a diameter of 1.25 m and a length of 13.12 m. Before centrifuge testing, a comprehensive set of characterization tests were performed on the pre-cast energy pile outside of the soil in a load frame at 1-gravity to determine its mechanical and thermal properties. The coefficient of thermal expansion (α) was estimated 7.5×10^{-6} m/m°C and the secant elastic modulus of energy pile (E) was estimated to be 7.17 GPa. The value of E is smaller than that of the reinforced concrete in full-scale energy piles because the amount of coarse aggregate was lower in the reinforced concrete of the model energy pile.

The model parameters from Stewart and McCartney (2014) are summarized as follows:

- Length L = 12.8 m
- Diameter D = 1.22 m
- Unit weight of pile γ_p = 24 kN/m^3
- Young's modulus of reinforced pile E = 7.17 GPa
- Coefficient of thermal expansion $\alpha_T = 7.5\times10^{-6}$ m/m°C
- Head-structure stiffness $K_h = 0$
- Empirical coefficient for radial expansion $\kappa = 65$

Soil obtained from the Bonny Dam near the Colorado-Kansas border was used in the energy-foundation test in this study. The soil layer was prepared by compacting silt having a gravimetric water content of 14% in 76.2-mm-thick lifts around the foundation to reach a target dry density of 1,451 kg/m^3. Drained soil properties were assumed for the ultimate side shear resistance along the pile, while an undrained shear strength was assumed for the soil at the toe of the pile. The soil parameters are given as follows:

- Drained friction angle $\phi' = 32.4°$
- Dry weight of soil γ_d= 16.9 kN/m^3

The fitting parameters for the Q-z curve of $a_b = 0.002$ and $b_b = 0.9$ were kept used in this analysis to represent the stiff end restraint at the tip of the foundation, and undrained shear strength at the toe $c_{u,b}$ is assumed to be 2000 kPa to simulate end-bearing condition. The parameters of the T-z curve that provided the best fit to the data are a_s = 0.0006, $b_s = 0.9$ and $\beta = 1.1$. Since Bonny silt in this case is unsaturated, the suction induced undrained shear strength c_u is found to be 30 kPa for the best fit.

The predicted axial compressive stress profiles using load-transfer model analysis along with the centrifuge data for each temperature change condition are shown in Figures 5.5(a) through 5.5(c).

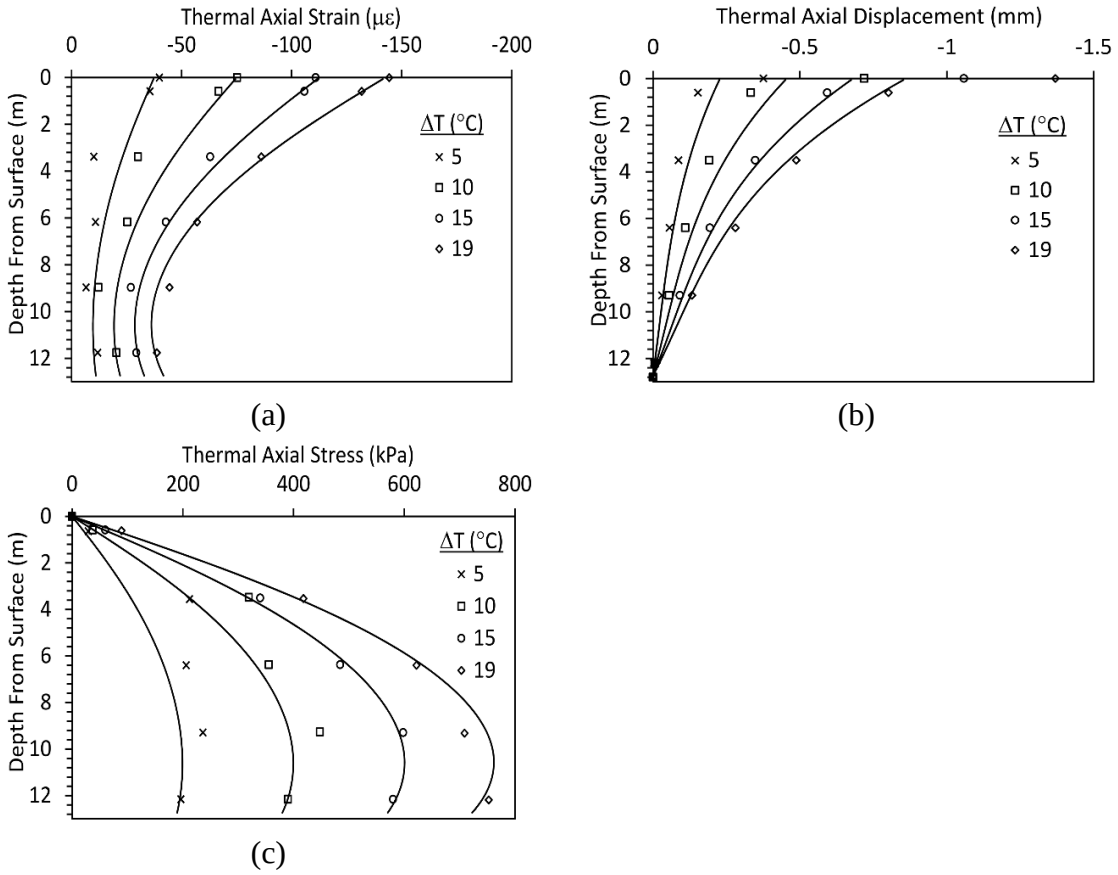

Figure 5.5: Predicted profiles of end-bearing pile with data with centrifuge model test by Stewart and McCartney (2014): (a) Thermal axial strains; (b) Thermal axial displacements; (c) Thermal axial stress

Stewart and McCartney (2014) plotted the thermal axial displacement values against the location at the midpoint between two strain gages. However, this should be plotted against the location of the upper gage. Accordingly, the experimental data from Stewart and McCartney were re-analyzed so that the calculated thermal axial displacement values correspond to the location of the upper gage. These good fits between numerical simulation result and the centrifuge data shown in Figure 5.5 confirm that the model is

capable of capturing the behavior of energy piles with different end restraint boundary conditions.

5.5 Calibration using the Data of Ng et al. (2015)

Three instrumented model piles having an external diameter (D) of 22 mm (0.88m in prototype) and length (L) of 600 mm (24 m) were placed in contained saturated soil at a centrifuge g-level of 40. Each model pile was prefabricated from an aluminum alloy tube with Young's modulus of 70 GPa and thermal expansion coefficient of 22.2×10^{-6} m/(m·K). Two adjacent piles were spaced equally at 305 mm (12.2 m) center to center (c/c), which was more than 13D to avoid pile interaction. The pile load test was carried out on the reference pile (RP), under the ambient temperature of 22°C. The first energy pile (EP1) and second energy pile (EP2) were heated up from temperatures of 22°C to 37°C and 52°C, respectively, before pile load tests were conducted.

All the tests were carried out in the saturated Toyoura sand, which is a subangular, uniform, quartz sand that does not contain fines. It has a mean diameter of d_{50} = 0.17 mm, a specific gravity of 2.65, a uniformity coefficient of U_c = 1.7, a maximum void ratio of 0.977 and a minimum void ratio of 0.597 (corresponding to a relative density between 67% and 89%, respectively), and an internal friction angle of 31° at the critical state. The fitting parameters for the Q-z curve of a_b = 0.003 and b_b = 0.9 were used in this analysis to represent the stiff end restraint at the tip of the energy pile. The undrained shear strength at the toe ($c_{u,b}$) is assumed to be 30 kPa. The parameters of the T-z curve that provided the best fit to the data were a_s = 0.0009, b_s= 0.9 and β = 0.2.

The predicted thermal induced axial force profiles using load-transfer model analysis along with the centrifuge data for each temperature change condition is shown in

Figures 5.6. It can be observed from Figure 5.6 that the load-transfer analysis gives results that are generally consistent with the centrifuge data in this case study. Yet, the discrepancies between simulation result and experimental data lie around the null point. The experimental data from this study was more nonlinear with a lower null point than those obtained from the model. This could be due to the characteristics of the pile, experimental issues with the strain gages, or uncertainties in the nonlinearity of the pile-sand interface shear resistance. This is also potentially because in the centrifuge test, the energy pile experienced mechanical loading after thermal loading had been applied, while in the model analysis, the mechanical load was applied before heating. Thermal loading before mechanical loading will cause the part of energy pile above the zero displacement point moving upward then moving downward, which is not included in current model.

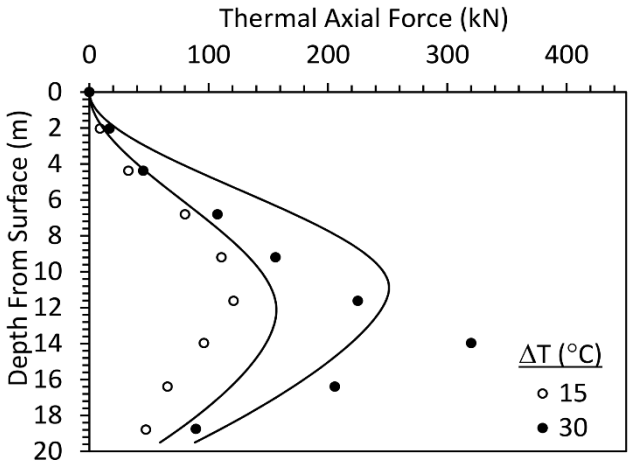

Figure 5.6: Predicted profiles thermal axial forces of semi-floating pile by Ng et al. (2015)

5.6 Summary of Parameters from Different Studies

A summary of the model parameters from the four different studies is presented in Table 5.2. The sands and sandstone were both represented using drained shear strength analyses, while the silt was represented using an undrained analysis. The end bearing

resistance was modeling using an undrained shear strength analysis in all cases, with a wide range of undrained shear strength values. The difference in the model parameters for the Bonny silt layers tested by Stewart and McCartney (2014) and Goode and McCartney (2015) can be attributed to the different compaction conditions for the soil layers tested. The values of β used in the centrifuge analyses are different from the ranges for drilled shafts in the field. This is expected, as the value of β represents installation effects on the side shear capacity. The energy piles in the centrifuge were installed by placing the soil around the piles, which may have led to different interface shear strengths from those expected of a full-scale pile in the field.

Table 5.2: Summary of model parameters

	Murphy et al. (2015)	Goode and McCartney (2015)		Stewart and McCartney (2014)	Ng et al. (2015)
Soil Type	Sandstone	Bonny silt	Nevada sand	Nevada sand	Toyoura sand
Foundation Type	Concrete	Concrete		Concrete	Aluminum
L (m)	15.2	8.2		12.8	19.6
D (m)	0.61	1.5		1.22	0.88
α ($\mu\varepsilon$/°C)	-12	-17	-16	-7.5	-22
E (GPa)	30	33		7.17	70
K_h (MN/m)	800 (Foundation 1,4) 300 (Foundation 3)	0		0	0
P (kN)	833	360		443	0
γ (kN/m)	19.2	14.2	15	14.2	9.5
ϕ' (°)	45	32.4	35	32.4	31
c_u (kPa)	-	20	-	30	-
a_s	0.0003	0.0001	0.0001	0.0006	0.0009
b_s	0.9				
a_b	0.002	0.002	0.001	0.002	0.003
b_b	0.9				
$c_{u,b}$ (kPa)	2000	54	100	2000	30
β	0.9	2.0	1.2	1.1	0.2

CHAPTER 6: DESIGN GUIDANCE

The goal of this chapter is to provide guidance on selection of parameters for application of thermo-mechanical T-z model to obtain predictions of the thermo-mechanical response of energy piles during preliminary design.

6.1 Soil-Structure Interaction Curves

The Q-z curves and T-z curves used in this simulation with parameters listed in Table 5.2 are plotted and presented in Figures 6.1(a) and 6.1(b), respectively. It can be observed from Figure 6.1(a) that as for most of the cases of tip resistance not reaching more than 65% of the ultimate tip capacity and ΔT is no more than 20°C, the tip displacement and the ultimate tip resistance approximately linearly increase with the ΔT. Observation of Q-z curves and T-z curves from Figures 6.1(a) and 6.1(b), the initial linear segments of T-z curves end up when the ultimate tip resistances reach 10% to 30% of ultimate tip resistances, and the flatten segments of T-z curves start when the ultimate tip resistances reach 25% to 55% of ultimate tip resistances. The curves used to represent the behavior of the aluminum pile in sand tested by Ng et al. (2015) are softer than the other curves, potentially due to the loose sand and the smoother interface of the aluminum.

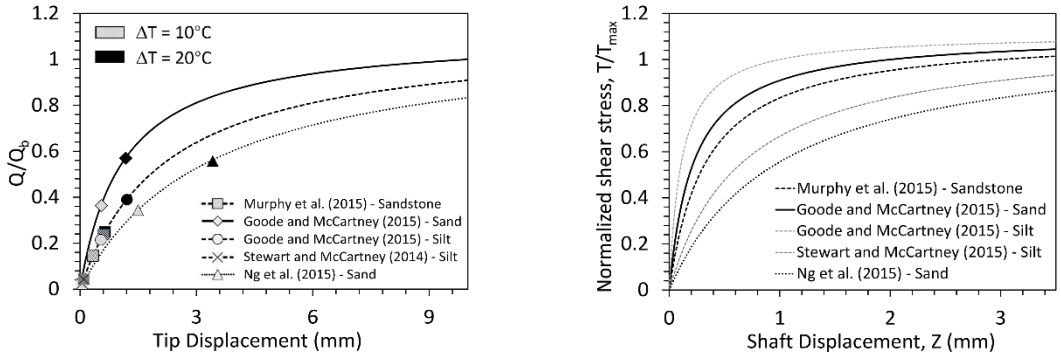

Figure 6.1: Hyperbolic nonlinear spring inputs for the load transfer analysis used in case studies: (a) Q-z curve; (b) T-z curve

6.2 Ratios of the Mobilized Resistance to the Ultimate Resistance

Plots of the variations in the ratio of the total mobilized resistance to the ultimate resistance induced by temperature variations for both the pile base resistance $Q_{b,T}$ /$Q_{b,max}$ and for the side shear resistance $Q_{s,T}$ /$Q_{s,max}$ are shown in Figures 6.2(a) and 6.2(b), respectively. These values are important to evaluate as they are related to the wise choice of the factor of safety for designing the energy pile during changes in temperature (Burlon et al. 2013). For each of the case histories $Q_{b,T}$ is obtained by performing thermo-mechanical load transfer analysis using parameters presented in Table 5.2, except the head stiffness K_h and change of temperature ΔT which are varying from 0 to 1000 MN/m and 0 to 20°C, respectively. The value of $Q_{s,T}$ was obtained by summing the side shear resistances of each pile element from the simulation results, while the value of $Q_{b,max}$ was calculated using Equation 3.10. The value of $Q_{s,max}$ is calculated by summing the ultimate side shear force for each elements using Equation 3.6. Upward and downward resistance are taken as positive and negative, respectively.

During heating, the base resistance systematically increases. As observed in Figure 6.2, the value of $Q_{b,T}$ /$Q_{b,max}$ increases less (i.e. approximately 0.001 to 0.03/°C) than the value of $Q_{s,T}$ /$Q_{s,max}$ (i.e. approximately 0.0005 to 0.016/°C) as the head stiffness K_h is varied from 0 to 1000 MN/m. The value of $Q_{s,T}$ /$Q_{s,max}$ linearly increases with the value of $Q_{b,T}$ /$Q_{b,max}$ for each case with the slope in the range of 5 to 50 depending on the stiffness of soil. The head stiffness affects whether negative side shear resistance is induced or not when temperature changes. It is clear that the aluminum pile tested by Ng et al. (2015) showed the most nonlinearity and widest range of ratios of the different piles due to its higher coefficient of thermal expansion.

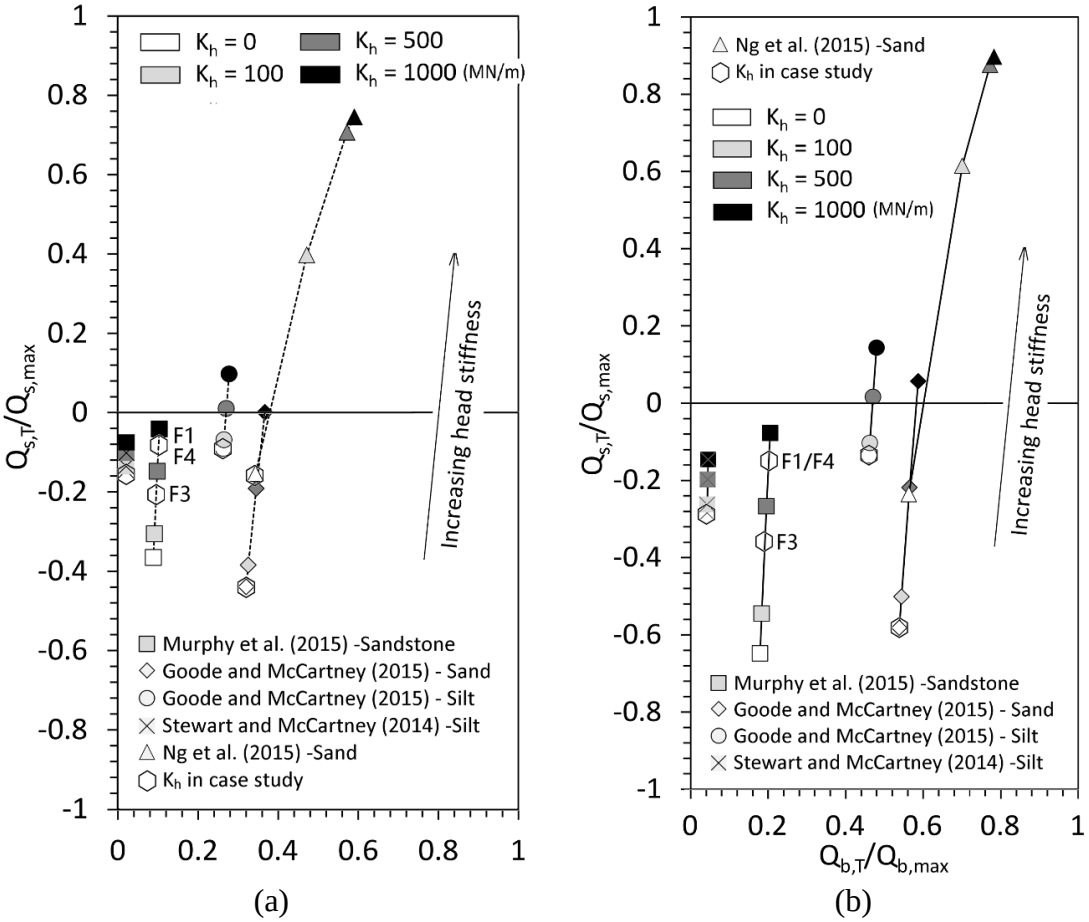

Figure 6.2: Ratios $Q_{b,T}/Q_{b,max}$ and $Q_{s,T}/Q_{s,max}$ for different head conditions and temperatures: (a) ΔT = 10°C; (b) ΔT = 20°C

Plots of the variations in the ratio of the total thermo-mechanical mobilized resistance to the ultimate resistance for both the pile base resistance $Q_{b,MT}/Q_{b,max}$ and for the side shear resistance $Q_{s,MT}/Q_{s,max}$ are shown in Figures 6.3(a) and 6.3(b), respectively. In Figures 6.3(a) and 6.3(b), values of $Q_{b,MT}/Q_{b,max}$ and $Q_{s,MT}/Q_{s,max}$ are obtained in the similar way $Q_{b,T}/Q_{b,max}$ and $Q_{s,T}/Q_{s,max}$ obtained as described above, and upward and downward resistance are also taken as positive and negative, respectively. Figures 6.3(a) and 6.3(b) show the impact of head stiffness K_h and the change of temperature ΔT on the percentage of thermo-mechanical side resistance and tip resistance of the ultimate capacity values. Similar conclusions can be drawn to the shapes of the curves in Figure 6.3, but the

major difference is that the thermo-mechanical stresses are closer to failure (i.e., 1.0). The closer the values of the ratio are to failure, the more nonlinear the behavior of the pile-soil interface. Further, it is increasingly possible that creep strains or cyclic effects may be encountered for piles loaded closer to failure (Pasten and Santamarina 2014). Nonetheless, for all of the scenarios considered in this analysis (i.e., a wide range of head stiffness values), the maximum value of the normalized thermo-mechanical side shear resistance was 0.9 and the maximum value of the normalized thermo-mechanical end bearing was 0.78. The aluminum pile tested by Ng et al. (2015) was the closest to failure likely due to the higher coefficient of thermal expansion of the aluminum.

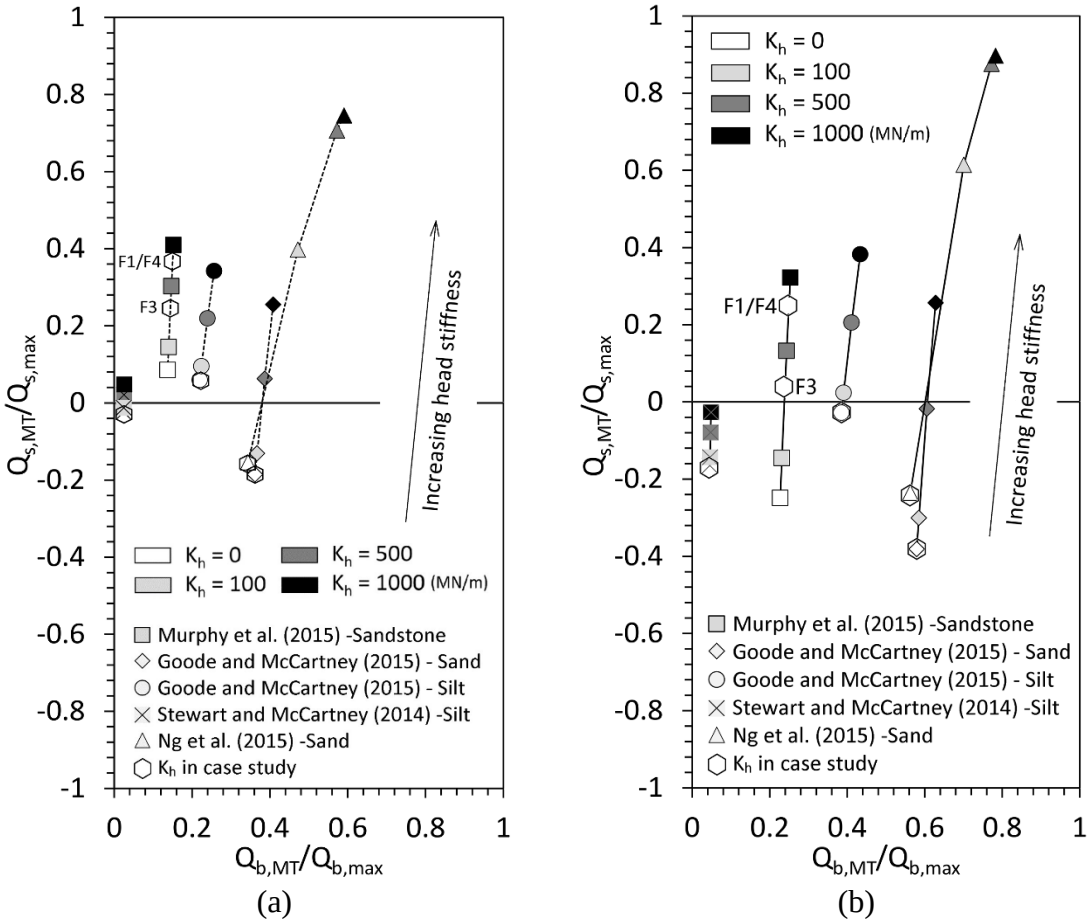

Figure 6.3: Ratios $Q_{b,MT}/Q_{b,max}$ and $Q_{s,MT}/Q_{s,max}$ for different head conditions and temperatures: (a) ΔT = 10°C; (b) ΔT = 20°C

6.3 Load and Settlement Relationships for the Head of the Energy Pile

It is important to understand the variation of head settlement for design because if the pile head displacement is more than the allowable limit for the structure, then the structure may fail by the Serviceability Limit State. The variations of head settlement ($\rho_{t,T}$) and head load ($Q_{t,T}$) induced by temperature variations and head stiffness are presented in Figure 6.4. Downward head load and head settlement are taken as positive. In Figure 6.4, $\rho_{t,T}$ and $Q_{t,T}$ are obtained from thermo-mechanical load transfer analysis using parameters presented in Table 5.2 with stiffness K_h varying from 0 to 1000 MN/m and change of temperature ΔT varying from 0 to 20°C. An interesting observation is that most of the curves for the piles made of concrete have a similar slope, which may be affected by both the Young's modulus and the coefficient of thermal expansion. This plot would be useful to assess the maximum thermal axial stress and displacement at the head of an energy pile made from a given material. It also emphasizes that very stiff elements with high thermal expansion (i.e., aluminum) may have different behavior than softer materials with lower thermal expansion (i.e., concrete).

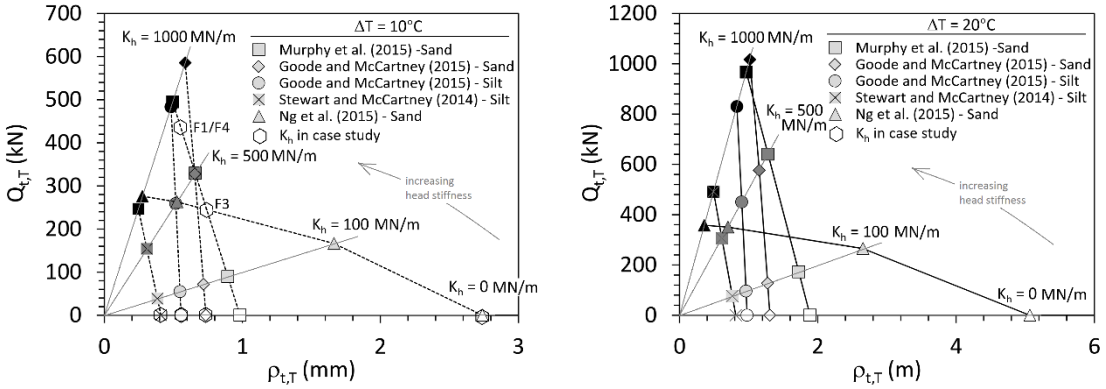

(a) (b)

Figure 6.4: Load vs. settlement plots for at equilibrium for the head of the pile under changes in temperature of: (a) ΔT = 10°C; (b) ΔT = 20°C

CHAPTER 7: CONCLUSION

This study involved the development of thermo-mechanical load-transfer analysis for capturing complex behavior of energy pile during mechanical and thermal loading. The key for successful simulation requires an accurate location of null point. Once the null point is defined, the status of strain and stress for energy pile will be computed by iteration for achieving equilibrium in two parts of pile separated by null point. Parametric evaluation is necessary to provide the effects of different parameters on the stress-strain response and settlement at both head and butt. The foundation type significantly affects settlement of energy pile. Comparing with the three common types of energy pile, the semi-floating pile is observed to have good control on settlement at both head and butt. Initial mechanical load increases the settlement as it takes the part of bearing capacity with comparably high stiffness, leaving the flatter part of T-z curve and Q-z curve at larger displacements for the pile to resist thermal loading. Soil shear strength affects the behavior of energy pile by affecting the ultimate capacity. The increase of temperature changes leads to pile expend so that larger resistance at head, butt and side skin will be generated, which significantly increase the strain and stress along the pile. Toe stiffness mainly affects the settlement at the butt and the head, though weaken the side shear resistance. The increase of head stiffness leads to more butt settlement as well as more stress along the pile. The impact of side shear stress-displacement curve mainly lies in the thermal induced stress along the pile. The radial expansion slightly increases the ultimate capacity at shaft skin. The thermo-mechanical load-transfer model was calibrated to four case studies to evaluate the typical ranges of values of the model parameters. These parameters from different cases are put into the model to provide preliminary design charts in terms of the ratio of the mobilized

resistance to the ultimate resistance and the head load and head settlement, but more case studies need to be evaluated using the load transfer analysis to fully delineate these trends.

A need for further study in the future is the role of thermal volume change, and associated changes in strength and stiffness, of the soil or rock surrounding the energy pile. As this study was focused on non-plastic soils, this issue is not relevant. However, energy piles may be installed in soft clays or expansive clays were appreciable volume changes or cyclic effects may be encountered. These soils may be considered using mobilized side shear resistance and end bearing resistance curves that vary with temperature and loading paths. Another issue that deserves further study is the role of heating and cooling about an average value. This requires slightly different shapes for the mobilized stress strain curves that can capture the hysteretic shape of the curves. The same concept for the hyperbolic curves can be used, but a transitional unloading function should be applied after unloading back to zero stress after plastic displacements are encountered.

REFERENCES

Akrouch, G., Sanchez, M., and Briaud, J.L. (2014). "Thermo-mechanical behavior of energy piles in high plasticity clays." Acta Geotechnica. 9(3), 399-412.

Amatya, B. L., Soga, K., Bourne-Webb, P. J., Amis, T., and Laloui, L. (2012). "Thermo-mechanical behaviour of energy piles." Geotechnique, 62(6), 503–519.

Burger, A., Recordon, E., Bovet, D., Cotton, L. & Saugy, B. 1985. Thermique des nappes souterraines. Laussane: Presses Polytechniques Romandes.

Bouazza, A., Singh, R.M., Wang, B., Barry-Macaulay, D., Haberfield, C., Chapman, G., Baycan, S., and Carden, Y. (2011). "Harnessing on site renewable energy through pile foundations." Aust. Geomech. J., 46(4), 79–90.

Bourne-Webb, P., Amatya, B., Soga, K., Amis, T., Davidson, C. and Payne, P. (2009). "Energy pile test at Lambeth College, London: Geotechnical and thermodynamic aspects of pile response to heat cycles." Géotechnique 59(3), 237–248.

Brandl, H. (2006). "Energy foundations and other energy ground structures." Géotechnique. 56(2), 81-122.

Burlon, S., Habert, J., Szymkievicz, F., Suryatriyastuti, M., and Mroueh, H. (2013). "Towards a design approach of bearing capacity of thermoactive piles." European Geothermal Congress 2013, Pisa, Italy. pp. 1-6.

Coyle, H. M., and Reese, L. C. (1966). "Load transfer for axially loaded piles in clay." J. Soil Mech. and Found. Div., 92(2), 1–26.

Goode, J.C., III and McCartney, J.S. (2015). "Centrifuge modeling of boundary restraint effects in energy foundations." Journal of Geotechnical and Geoenvironmental Engineering. 141(8), 04015034-1-04015034-13. DOI: 10.1061/(ASCE)GT.1943-5606.0001333.

Goode, J.C., III, Zhang, M. and McCartney, J.S. (2014). "Centrifuge modeling of energy foundations in sand." Physical Modeling in Geotechnics: Proceedings of the 8th International Conference on Physical Modelling in Geotechnics. Perth. Jan. 14-17. C. Gaudin and D. White, eds. Taylor and Francis. London. pp. 729-736.

Goode, J.C., III and McCartney, J.S. (2014). "Evaluation of head restraint effects on energy foundations." Proceedings of GeoCongress 2014 (GSP 234), M. Abu-Farsakh and L. Hoyos, eds. ASCE. pp. 2685-2694.

Knellwolf, C., Peron, H., and Laloui, L. (2011). "Geotechnical analysis of heat exchanger piles." Journal of Geotechnical and Geoenvironmental Engineering. ASCE. 137(12), 890-902.

Laloui, L. (2011). “In-situ testing of heat exchanger pile.” Proc., GeoFrontiers 2011, J. Han and D. E. Alzamora, eds., ASCE, Reston, VA, 410–419.

Laloui L, Moreni M, Vulliet L. (2003). “Comportement d'un pieu bi-fonction, fondation et échangeur de chaleur.” Canadian Geotechnical Journal 40(2): 388–402.

Laloui, N. and Nuth, M. (2006). “Numerical modeling of some features of heat exchanger pile.” ASCE GSP 153. ASCE. Reston, VA. pp. 189-195.

Laloui, L., Nuth, M., and Vulliet, L. (2006). “Experimental and numerical investigations of the behaviour of a heat exchanger pile.” International Journal of Numerical and Analytical Methods in Geomechanics. 30(8), 763–781.

McCartney, J.S. (2015). “Structural performance of thermo-active foundations.” In: Advances in Thermo-Active Foundations. M. Krarti, ed. ASME Press. New York. pp. 1-44. ISBN: 9780791861059.

McCartney, J. S. and Rosenberg, J. E. (2011). “Impact of heat exchange on side shear in thermo-active foundations.” ASCE Geo-Frontiers, 488-498.

McCartney, J.S., and Murphy, K.D. (2012). “Strain distributions in full scale energy foundations.” DFI Journal. 6(2), 28–36.

Mimouni T, Laloui L. (2014). “Towards a secure basis for the design of geothermal piles.” Acta Geotechnica 9(3): 355-366.

Murphy, K.D., McCartney, J.S., and Henry, K.S. (2015). “Evaluation of thermo-mechanical and thermal behavior of full-scale energy foundations.” Acta Geotechnica. 10(2), 179-195.

Murphy, K.D. and McCartney, J.S. (2014). “Thermal borehole shear device.” ASTM Geotechnical Journal. 37(6), 1040-1055.

Murphy, K.D. and McCartney, J.S. (2015). “Seasonal response of energy foundations during building operation.” Geotechnical and Geological Engineering. 33(2), 343-356.

Ng, C.W.W., Shi, C., Gunawan, A. & Laloui, L. (2014). “Centrifuge modelling of energy piles subjected to heating and cooling cycles in clay.” Géotechnique Letters 4, 310-316.

Ng, C.W.W., Shi, C., Gunawan, A., Laloui, L., et al. (2015). “Centrifuge modelling of heating effects on energy pile performance in saturated sand.” Canadian Geotechnical Journal 52, 1-13.

Olgun, C.G., Ozudogru, T.Y., Abdelaziz, S.L., and Senol, A. (2014a). "Long-term performance of heat exchanger pile groups.” Acta Geotechnica. 10(5), 553-569.

Olgun, C., Ozudogru, T., and Arson, C. (2014). “Thermo-mechanical radial expansion of heat exchanger piles and possible effects on contact pressures at pile–soil interface.” Géotechnique Letters, 10.1680/geolett.14.00018, 170-178.

Ouyang, Y., Soga, K., and Leung, Y. F. (2011). “Numerical back-analysis of energy pile test at Lambeth College, London.” Proc., Geo-Frontiers 2011 (GSP 211), J. Han and D. E. Alzamora, eds., ASCE, Reston, VA, 440–449.Plaseied, N. (2012). “Load transfer analysis of energy foundation. MS Thesis. University of Colorado Boulder.

Ozudogru, T.Y., Olgun, C.G. and Senol, A. (2014). “3D numerical modeling of vertical geothermal heat exchangers.” Geothermics. 51, 312–324.

Pasten, C. and Santamarina, J.C. (2014). “Thermally induced long-term displacement of thermoactive piles.” Journal of Geotechnical and Geoenvironmental Engineering 140 (5), 06014003.

Reese, L.C., O’Neill, M.W. (1987), “Drilled shafts: construction procedures and design methods.” Report FHWA-HI-88-042, US Department of Transportation, Federal Highway Administration, Office of Implementation, McLean, Virginia.

Reese, L.C., Isenhower, W.M. and Wang, S.-T. (2006). Analysis and Design of Shallow and Deep Foundations. Wiley Interscience. New York.

Rollins, K.M., Clayton, R.J., and Mikesell, R.C. (1997). “Ultimate side friction of drilled shafts in gravel.” Foundation Drilling, June/July, pp. 10-13.

Rotta Loria, A.F., Gunawan, A., Shi, C., Laloui, L. & Ng, C.W.W. (2015a). “Numerical modelling of energy piles in saturated sand subjected to thermo-mechanical loads.” Geomechanics for Energy and the Environment 1, Vol. 1, 1-15.

Rotta Loria, A., Donna, A., and Laloui, L. (2015). “Numerical study on the suitability of centrifuge testing for capturing the thermal-induced mechanical behavior of energy piles." J. Geotech. Geoenviron. Eng., 10.1061/(ASCE)GT.1943-5606.0001318, 04015042.

Stewart, M.A. and McCartney, J.S. (2014). “Centrifuge modeling of soil-structure interaction in energy foundations.” ASCE Journal of Geotechnical and Geoenvironmental Engineering. 140(4), 04013044-1-04013044-11.

Suryatriyastuti M. E., Mroueh H., Burlon S. and Habert J. (2013). Numerical analysis of the bearing capacitiy in thermo-active piles under cyclic axial loading. Energy geostructures: Innovation in Underground Engineering. L. Laloui and A. Di Donna. Hoboken, ISTE Ltd. and John Wiley and Sons: 139-154.

Sutman, M., Brettmann, T. and Olgun, C.G. (2014). “Thermo-mechanical behavior of energy piles: full-scale field test verification”. DFI 39th Annual Conference on Deep Foundations, Atlanta, GA. October 21-24, 2014. pp. 1-11.

Tomlinson, M. J. (1957). “The adhesion of piles in clay soils.” Proc., Fourth Intern. Conf. on Soil Mech. and Found. Engr. Vol. 2, pp. 66-71.

Wang, W., Regueiro, R., Stewart, M. A., and McCartney, J. S. (2012). “Coupled thermo-poro-mechanical finite element analysis of a heated single pile centrifuge experiment in saturated silt.” Proc., GeoCongress 2012 (GSP 225), R. D. Hryciw, A. Athanasopoulos-Zekkos, and N. Yesiller, eds., ASCE, Reston, VA, 4406–4415.

Wang, B., Bouazza, A., Singh, R., Haberfield, C., Barry-Macaulay, D., and Baycan, S. (2014). “Post-temperature effects on shaft capacity of a full-scale geothermal energy pile.” J. Geotech. Geoenviron. Eng., 10.1061/(ASCE)GT.1943-5606.0001266, 04014125.

Wang, W., Regueiro, R., and McCartney, J. S. (2015). “Coupled axisymmetric thermo-poro-elasto-plastic finite element analysis of energy foundation centrifuge experiments in partially saturated silt.” Geotech. Geolog. Eng., 33(2), 373–388.

APPENDIX A

```
%-----------------------------------------------------
%|This is procedure file named as calcM.m   |
%-----------------------------------------------------
pbo = 0;                        % Last assumed displacement at toe
R = 0;                          % Force at head obtained from equilibrium
pb = 1;                         % Assumed displacement at toe
while abs(P+R)>tol
   for i = N:-1:1               % Steps down from N to 1
      % Initialize the force and displacement for element i
      if i == N                 % For the bottom element first
         QtM(i) = 0;            % Set the force at the top equal to an initially small value
         pbM(i) = pb;           % For the bottom element, set this equal to the initial value of pb (zero to start)
         QbM(i)=-Qp*pbM(i)/(ab+pbM(i)*bb);       % Force at bottom from Q-z curve
      else
         pbM(i) = ptM(i+1);         % Set the displacement of the bottom of the next element
                                    % equal to the force on the previous element
         QbM(i) = -QtM(i+1);        % Set the force of the bottom of the next
                                    % element equal to the force on the previous element
         QtM(i) = 0;                % Set the force on the top of the next element to zero initially
      end;
      DQt = 999;                    % Set the change in force at top to an initially high value
      % This loop is used to find QtM(i) to make the element i converged.
      while DQt > tol
         QaveM(i) = (QtM(i)-QbM(i))/2;          % Average axial force at ith element
         deltaM(i) = QaveM(i)/Ki(i);            % Axial elongation of ith elemnet
         ptM(i) = pbM(i) + deltaM(i);           % Dispalcement at the head of ith element
         psM(i) = pbM(i) + deltaM(i)/2;         % Displacement at the middle of ith element
         FsM(i)=-FsmaxM(i)*psM(i)/(as+psM(i)*bs);       % Side shear force of ith element
         QtnewM(i) = - (FsM(i) + QbM(i));       % Force at the head of ith element obtained by equilibium
         DQt = QtnewM(i) - QtM(i);              % Change of the force at the head of ith element
         QtM(i) = QtnewM(i);                    % Update the force at the head of ith element
      end
      % Convergence of ith element means the behavior of the part of pile
      % below element i is obtained for assumed toe displacement.
   end
   % Find next toe displacement to be assumed
   FsMtot = sum(FsM);               % Total side shear force (kN/m3)
   R = FsMtot+QbM(N);
   K = R/pb;                        % Secant slope for find next pb to be assumed
   pbo = pb;
   pb = pb-(P+R)/K;                 % (P+R)is unbalanced force
end
sigmaM = QaveM/Ab;                  %Axial stress (kN/m2)
pb=pbo;


%-----------------------------------------------------
%|This is procedure file named as calcMT.m |
%-----------------------------------------------------
m = 30;                             % Parameter for controlling the update speed of deltaT
% |---------------------------------------|
% |-------Calculate the buttom part------|
```

```
% |--------------------------------------|
DDTb=Inf;                                % Change of sum(deltaT)
deltaT(N1+1:N,1)=Li(N1+1:N)*alphaT*DT;   % Initialize thermal elongation at free expansion
while sum(abs(DDTb))>tol
   % Calculate the displacement based on deltaT
   for j=N1+1:N
      if j==N1+1                 % Displacement at the top of ith element
         ptT(j) = 0;             % Case for element next to NP
      else
         ptT(j) = pbT(j-1);      % General case
      end;
      ptMT(j) = ptM(j) + ptT(j);       % M+T displacement at the top of jth element
      psT(j) = ptT(j) - deltaT(j)/2;   % T displacement at the side of jth element
      psMT(j) = psM(j)+psT(j);         % M+T displacement at the side of jth element
      pbT(j) = ptT(j) - deltaT(j);     % T displacement at the bottum of jth element
      pbMT(j) = pbM(j) + pbT(j);       % M+T displacement at the bottum of jth element
   end;
   % ---- Calculate the force based on displacement -----
   for j=N:-1:N1+1
      if j==N
         QbMT(j) = - Qp * pbMT(j) / (ab + bb * pbMT(j));   % Case for toe element
      else
         QbMT(j) = - QtMT(j+1);                            % General case
      end;
      FsMT(j) = -FsmaxMT(j)*psMT(j)/(as+psMT(j)*bs);       % MT side shear force
      QtMT(j) = - (QbMT(j) + FsMT(j));         % MT force at top of jth element obtained from equilibrium
   end;
   % ---- Update the deltaT ----
   QaveMT = (QtMT - QbMT) / 2;                 % Average axial forces for each element
   sigmaMT = QaveMT/Ab;                        % Average axial stresses for each element
   deltanewT = [zeros(N1,1);deltaTfree(N1+1:N)-deltaM(N1+1:N)]+sigmaMT.*Li/(E); % New elongation
                                                                                % according to current force
   deltaT = (deltanewT-deltaT)/m+deltaT;       % Update elongation to be 1/m close to the new DeltaT
   DDTb = deltaT-deltanewT;                    % Different between new and old deltaT
end;

% |----------------------------------|
% |-------Calculate the top part-----|
% |----------------------------------|
DDTb=Inf;                                % Change of sum(deltaT)
deltaT(1:N1) = Li(1:N1)*alphaT*DT;       % Initialize thermal elongation at free expansion
while sum(abs(DDTb))>tol
   % ---- Calculate the displacement based on deltaT -----
   for j=N1:-1:1
      if j==N1                           % Displacement at the bottum of ith element
         pbT(j) = 0;                     % Case for element next to NP
      else
         pbT(j) = ptT(j+1);              % General case
      end;
      pbMT(j) = pbM(j) + pbT(j);         % M+T displacement at the bottum of jth element
      psT(j) = pbT(j) + deltaT(j)/2;     % T displacement at the side of jth element
      psMT(j) = psM(j)+psT(j);           % M+T displacement at the side of jth element
      ptT(j) = pbT(j) + deltaT(j);       % T displacement at the top of jth element
      ptMT(j) = ptM(j) + ptT(j);         % M+T displacement at the top of jth element
```

```
    end;
    % ---- Calculate the force based on displacement -----
    for j=1:N1
        if j==1
            QtMT(j) = -Kh*(ptMT(j)-ptM(j)) + P;   % Case for head element
        else
            QtMT(j) = - QbMT(j-1);                % General case
        end;
        if beta==0
            FsMT(j)=0;                            % Non-friction case
        else
            FsMT(j) = - FsmaxMT(j)*(psMT(j)/as+(-FsM(j))/FsmaxM(j)-(1/((FsmaxM(j)/(-FsM(j)))-bs)));
                                                  % side friction for unloading
        end;
        QbMT(j) = -( QtMT(j) + FsMT(j) );         % MT force at bottom of element j from equilibrium
    end;
    % ---- Update the deltaT ----
    QaveMT = (QtMT(1:N1) - QbMT(1:N1))/2;   % Average axial forces for each element
    sigmaMT = QaveMT/Ab;                    % Average axial stresses for each element
    deltanewT = [deltaTfree(1:N1)+sigmaMT.*Li(1:N1)/(E)-deltaM(1:N1);deltaT(N1+1:N)];
                                            % New elongation according to current force
    deltaT = (deltanewT-deltaT)/m+deltaT;   % Update elongation to be 1/m close to the new DeltaT
    DDTb = deltaT-deltanewT;                % Different between new and old deltaT
end;


%---------------------------------------------------------
%|This is main program file named as main.m   |
%---------------------------------------------------------
clear;
clear all
format long e
warning off
%% ========= Define Variable ========  %%
%% SOIL DESCRIPTION %%
gamsoil=14.2;                   % Unit weight of soil
Phi=32.4;                       % Friction angle
K0=1-sin(Phi*pi/180);           % Coefficient of lateral earth pressure at rest
Kp = (1+sin(Phi*pi/180))/(1-sin(Phi*pi/180));   % Coefficient of passive earth pressure
drain = 1;                      % Define drained or undrained soil
cu=0;                           % Undrained shear strength
cub=2000;                       % Undrained shear strength at toe (kN/m2)
cusuc=30;                       % Suction-induced undrained shear strength (kN/m2)
%% FOUNDATION DESCRIPTION %%
L=12.8;                         % Length of pile (m)
D=1.22;                         % Diameter of pile (m)
Ab = pi*D^2/4;                  % Cross-sectional area (m2)
Cs = pi*D;                      % Circumference of pile (m)
gampile =  24;                  % INPUT Unit weight of concrete (kN/m3)
E=7170000;;                     % Young's modulus of pile
N = 100;                        % INPUT Number of pile elements
Wpile = gampile*Ab*L;           % Weight of pile (kN)
Wdisp = gamsoil*Ab*L;           % Weight of soil displaced (kN)
Wp = Wpile - Wdisp;             % Buoyant unit weight of pile (kN)
```

```
k = 65;                          % Radial expansion
alphaT=-7.5e-6;                  % Coefficient of thermal expansion
%% SOIL-STRUCTURE INTERACTION PARAMETER %%
Kh = 0.001;                      % Head stiffness
ab = 0.002;bb = 0.9;             % Parameter for toe stiffness
as = 0.0006;bs = 0.9;            % Parameter for side friction
alpha = 0.27;
beta =1.1;

%% MECHANICAL T-Z ANALYIS BASED ON APPLIED LOAD "P" %%
P = 443;                         % Mechanical load (kN)

% ESTIMATE ULTIMATE END BEARING %
sc = 1.2;                        % Shape factor
dc = 1.5;                        % Depth factor
Nc = 5;                          % Bearing capacity factor
Qp = cub*Ab*sc*dc*Nc;            % Total end bearing (kN)

% INITIALIZE VARIABLES %
QbM = zeros(N,1);                % Force at bottom of element (kN)
QtM = zeros(N,1);                % Force at top of element (kN)
FsM = zeros(N,1);                % Mobilized side shear force on each element (kN)
pbM = zeros(N,1);                % Displacement at bottom of each element (m)
ptM = zeros(N,1);                % Displacement at top of each element (m)
psM = zeros(N,1);                % Shear displacement at side of each element (m)
QaveM = zeros(N,1);              % Average force in each element (kN)
deltaM = zeros(N,1);             % Compression of each element (m)
sM = zeros(N,1);                 % Axial strain (microstrain)
sigmaM = zeros(N,1);             % Axial stress (kN/m2)
pb = 0;                          % Initial toe displacement (m)

% % ----------------------------------------------------------------------%
%% THERMO-MECHANICAL T-Z ANALYSIS %%
DT = 15;                         % Change of temperature

% ESTIMATE INCREASE IN ULTIMATE CAPACITY WITH HEATING %
KT = -k*alphaT*DT*(D/2)/(0.02*L);        % Mobilized radial expansion coefficient

% INITIALIZE THERMAL T-z VARIABLES %

QtT = zeros(N,1);                % Thermal axial force at the top of each element (kN)
QtMT = zeros(N,1);               % Thermo-Mechanical force at the top of each element (kN)
QbT = zeros(N,1);                % Thermal axial force at the bottom of each element (kN)
QbMT = zeros(N,1);               % Thermo-Mechanical force at the bottum of each element (kN)
QaveT = zeros(N,1);              % Change in average axial force due to heating (kN)
FsT = zeros(N,1);                % Mobilized side shear force due to thermal loading (kN)
FsMT = zeros(N,1);               % Mobilized side shear force due to thermo-mechanical loading (kN)
psT = zeros(N,1);                % Thermal shear displacement (m)
psMT = zeros(N,1);               % Thermo-mechanical shear displacement (m)
pbT = zeros(N,1);                % Thermal displacement at the bottom of each element (m)
pbMT = zeros(N,1);               % Thermo-Mechanical displacement at the bottum of each element (m)
ptT = zeros(N,1);                % Thermal displacement at the top of each element (m)
ptMT = zeros(N,1);               % Thermo-Mechanical displacement at the top of each element (m)
deltaT = zeros(N,1);             % Constrained thermal expansion of each element (m)
```

```
sigmaT = zeros(N,1);            % Thermal axial stresses in each element (kPa)
sigmaMT = zeros(N,1);           % Thermo-mechanical axial stresses in each element (kPa)
sT = zeros(N,1);              % Thermal axial strains in each element
sMT = zeros(N,1);             % Thermo-mechanical axial strains in each element

deltanewT=zeros(N,1);         % Vector of intermediate deltaT values used in the loop calculations
Difnull=zeros(N-1,1);         % Difference in force above and below the null point
tol=1e-10;                    % Tolerance for the thermal T-z analysis

% INITIALIZE THE VARIABLES FOR FINDING NULL POINT %
NP=1e-2;                      % Assumed null point (m)
NPo=-1;                       % Last assumed null point (m)
K=0;                          % Secant slope in Newton's method used to find next NP
dNP=L/N;                      % Increment to define the next NP to be tried (m)

% CALCULATE THE BEHAVIOR OF PILE ACCORDING TO THE ASSUMED NULL POINT %
while abs(NP-NPo)>=tol;
   % Define NP and mesh the elements according to the length of part of
   % pile. Make sure the element of part of pile is not less than 0.1*N
   if NP<L/2
      N1=max(round(NP/L*N),0.1*N);      % Number of element above the NP
      N2=N-N1;                          % Number of element below the NP
   else
      N2=max(round((L-NP)/L*N),0.1*N);
      N1=N-N2;
   end;
   Li=[zeros(N1,1)+NP/N1;zeros(N2,1)+(L-NP)/N2];      % Length of each element (m)
   z=[(0:1:N1-1)'*NP/N1+NP/N1/2';(0:1:N2-1)'*(L-NP)/N2+NP+(L-NP)/N2/2];
   As = Cs*Li;                       % Lateral areas of each element (m2)
   Ki = Ab*E./Li;                    % Axial stiffness of each element (kN/m)
   sigv = gamsoil*z;                 % Effective vertical stress of soil(kN/m2)

   % MECHANICAL T-Z ANALYSIS
   if drain==1
      fsM = beta*sigv*K0*tan(Phi*pi/180);    % Drained ultimate side shear stress (kN/m2)
   else
      fsM = alpha*cu;                % Undrained ultimate side shear stress (kN/m2)
   end;
   FsmaxM = fsM.*As;                 % Ultimate side shear force for each element (kN)
   calcM;                            % Call calcM.m to find the behavior of pile under mechanical load

   % THERMO-MECHANICAL T-Z ANALYSIS
   if drain==1
      fsmaxT = beta*(K0+(Kp-K0)*KT)*sigv*tan(Phi*pi/180);    % Drained ultimate side shear stress
                                                              % (kN/m2)
   else
      fsmaxT = alpha*cu;                  % Undrained ultimate side shear stress (kN/m2)
   end;
   FsmaxMT = fsmaxT.*As;                  % Ultimate side shear force after heating (kN)
   FstotMT = sum(FsmaxMT);                % Total Ultimate side shear force after heating (kN)
   deltaTfree(1:N,1) = Li*alphaT*DT;      % Define elongation under free expansion condition
   calcMT;                          % Call calcMT.m to find the behavior of pile under M-T load

   % Find out the next NP location to be assumed
```

```
   unb=QtMT(N1+1)+QbMT(N1);              % Unbalance force at NP
   if (unb>0)&&(NP+dNP<L)                % Case: NP to be deeper than assumed
      NPo=NP;
      NP=NP+dNP;
   else                                  % Case: NP between this and last assumed NP
      if NP+dNP<L
         dNP=dNP/2;
         NP=NPo+dNP;
         dNP=dNP/2;
      else
         dNP=dNP/2;
      end;
   end;
end;

% Additional data that haven't been calculated in T-z analysis procedure
sigmaMT = (QtMT - QbMT)/2/Ab;        % M-T axial stresses
sigmaT=sigmaMT-sigmaM;               % T axial stresses
epsMT = (deltaM+deltaT)./Li*1e6;     % M-T axial strains
epsT = deltaT./Li*1e6;               % T axial strains
epsM = deltaM./Li*1e6;               % M axial strains
QaveMT = (QtMT - QbMT)/2;            % M-T axial average force in elements
FsT=FsMT-FsM;                        % T force at base of elements
QbT=QbMT-QbM;                        % T force at top of elements
QtT=QtMT-QtM;

% =======  Output  ======
disp('Null point:');
disp(NP);
```